1979

Formation of calcium aluminates in the lime sinter process

Kan-Sen Chou
Iowa State University

CHOU, KAN-SEN

FORMATION OF CALCIUM ALUMINATES IN THE LIME SINTER PROCESS

Iowa State University PH.D. 1979

PLEASE NOTE:

In all cases this material has been filmed in the best possible way from the available copy. Problems encountered with this document have been identified here with a check mark ✓.

1. Glossy photographs _____
2. Colored illustrations _____
3. Photographs with dark background ✓
4. Illustrations are poor copy _____
5. Print shows through as there is text on both sides of page _____
6. Indistinct, broken or small print on several pages ✓ throughout _____
7. Tightly bound copy with print lost in spine _____
8. Computer printout pages with indistinct print _____
9. Page(s) _____ lacking when material received, and not available from school or author _____
10. Page(s) _____ seem to be missing in numbering only as text follows _____
11. Poor carbon copy _____
12. Not original copy, several pages with blurred type _____
13. Appendix pages are poor copy _____
14. Original copy with light type _____
15. Curling and wrinkled pages _____
16. Other _____

Formation of calcium aluminates in the lime sinter process

by

Kan-Sen Chou

A Dissertation Submitted to the

Graduate Faculty in Partial Fulfillment of the

Requirements for the Degree of

DOCTOR OF PHILOSOPHY

Major: Chemical Engineering

Approved:

Signature was redacted for privacy.

In Charge of Major Work

Signature was redacted for privacy.

For the Major Department

Signature was redacted for privacy.

For the Graduate College

Iowa State University
Ames, Iowa

1979

TABLE OF CONTENTS

	Page
INTRODUCTION	1
LITERATURE REVIEW	7
Diffusion in Solids	7
Chemical and structural defects in crystalline solids	8
Diffusion mechanisms	8
Reactivity of solids	11
Elementary Steps of Solid State Reactions	13
Kinetics of Solid State Reactions	14
Diffusion-controlled reactions	15
Phase-boundary controlled reactions	20
Nucleation and growth controlled reactions	21
Kinetic equations based on the concept of an order of reaction	22
Examination of Reactions in Real Systems	22
$CaO-SiO_2$ system	22
$CaO-Al_2O_3$ system	26
$Al_2O_3-SiO_2$ system	28
$CaO-Al_2O_3-SiO_2$ system	28
EXPERIMENTAL PROCEDURE	31
Materials and Preparation of Pellets	31
Furnacing the Pellets	35
Qualitative Analysis of the Sintered Products	39
X-ray diffraction analysis	39
Scanning Electron Microscopy (SEM)	41
Electron microprobe analysis (EMPA)	42
High temperature X-ray analysis	43
Differential thermal analysis (DTA)	45
Quantitative Analysis of the Sintered Products	47
Maleic acid treatment	47
Chemical analysis	48
Quantitative X-ray diffraction analysis	49

Leaching of the Sinters 53

Analysis of the Extracts and Residues 53

DISCUSSION OF RESULTS 55

Results of Qualitative Analysis of the Sinters 55

X-ray diffraction analysis 55
Scanning electron microscopy (SEM) 63
Electron microprobe analysis (EMPA) 73
High-temperature X-ray diffraction analysis 82
Differential thermal analysis (DTA) 88

Results of Quantitative Analysis of the Sinters 94

Chemical analysis 95
Quantitative X-ray diffraction analysis 98
Kinetic analysis of the formation of aluminates 104

The C_3A phase 109
The CA phase 125
The $C_{12}A_7$ phase 125

Thermodynamic study of reactions in the $CaO-Al_2O_3$ system 127

Results of Leaching Studies 133

CONCLUSIONS 139

RECOMMENDATIONS 141

REFERENCES 143

ACKNOWLEDGMENTS 152

LIST OF FIGURES

		Page
Fig. 1.	Lime sinter process for the recovery of alumina from fly ash	5
Fig. 2.	Mechanisms of lattice diffusion. A — Vacancy diffusion. B — Interstitialcy diffusion. C — Interstitial diffusion	10
Fig. 3.	Basic stages in the formation of monocalcium silicate when CaO and SiO_2 react	24
Fig. 4.	Phase diagram of the $CaO-Al_2O_3-SiO_2$ system	29
Fig. 5.	Particle size distribution of ground, pure Al_2O_3	34
Fig. 6.	The Lindberg hevi-duty tube furnace used in the sintering runs	36
Fig. 7.	The X-ray furnace used in the high-temperature X-ray work	36
Fig. 8.	Temperature distribution along the tube when the Lindberg furnace setpoint is 1300°C	38
Fig. 9.	The heating element for high-temperature X-ray work	44
Fig. 10.	Influence of $C_{12}A_7$ on the d = 2.97 peak of CA	52b
Fig. 11.	X-ray patterns of the sinter (1200°C, 1 hr) after being leached by maleic acid-methanol solution. CA, C_3A and C_5A_3 were formed	56
Fig. 12.	X-ray patterns of the sinter (1200°C, 4 hr) after being leached by maleic acid-methanol solution. The intensities of the peaks of C_3A and C_5A_3 increased, while that of CA remained at about the same level	57
Fig. 13.	X-ray patterns of the sinter (1300°C, 1 hr) after being leached by maleic acid-methanol solution. Three phases, CA, C_3A and $C_{12}A_7$ were found	58
Fig. 14.	X-ray patterns of the sinter (1300°C, 4 hr) after being leached by maleic acid-methanol solution. Both CA and C_3A decreased, but $C_{12}A_7$ increased	59
Fig. 15.	Phase diagram of the $CaO-Al_2O_3$ system in ordinary atmosphere	62

Fig. 16. Phase diagram of the $CaO-Al_2O_3$ system in a moisture-free atmosphere 62

Fig. 17. SEM micrograph of SiO_2 gel ground for 6 hours (500x) 64

Fig. 18. SEM micrograph of Al_2O_3 ground for 6 hours (500x) 64

Fig. 19. SEM micrograph of the ternary mixture ground for 6 hours (1000x) 66

Fig. 20. A closer look at the above micrograph (3000x) 66

Fig. 21. SEM micrograph of the ternary powder sintered at 1250°C for 7 hours (2000x) 68

Fig. 22. A closer look at the above micrograph (6000x) 68

Fig. 23. SEM micrograph of the ternary sinter (1250°C, 7 hr) after being leached by 3% Na_2CO_3 solution (3000x) 70

Fig. 24. SEM micrograph of the ternary sinter (1250°C, 7 hr) after the maleic acid treatment (2000x) 70

Fig. 25. Distribution of oxides across the $CaO-Al_2O_3-SiO_2$ pellet (sintered at 1350°C for 1 hr) as analyzed by EMPA 75

Fig. 26. Photomicrograph of a polished section of $CaO-Al_2O_3-SiO_2$ pellet sintered at 1350°C for 1 hr (940x) 76

Fig. 27. Energy dispersive X-ray analysis of calcium for Fig. 26. Except for the black area, the calcium is distributed evenly in the pellet (940x) 76

Fig. 28. Energy dispersive X-ray analysis of silicon for Fir. 26. Its distribution is not as uniform as that of calcium (940x) 78

Fig. 29. Energy dispersive X-ray analysis of aluminum for Fig. 26. There are three areas where only aluminum exists. This indicates unreacted alumina particles (940x) 78

Fig. 30. Point analysis (as dots) by EMPA of polished section of a $CaO-Al_2O_3-SiO_2$ pellet sintered at 1350°C for 2 hours 81

Fig. 31. High-temperature X-ray patterns of a mixture of $CaCO_3$ and Al_2O_3 (molar ratio 12:7) at 900°C and 1000°C 83

Fig. 32. High-temperature X-ray patterns of a mixture of $CaCO_3$ and Al_2O_3 (molar ratio 12:7) at 1100°C and 1250°C 84

Fig. 33. X-ray patterns of the ternary mixture of CaO-Al_2O_3-SiO_2 at 900°C and 1000°C 86

Fig. 34. X-ray patterns of the ternary mixture of CaO-Al_2O_3-SiO_2 at 1100°C and 1250°C 87

Fig. 35. DTA and TG curves for a binary mixture of $CaCO_3$ and SiO_2 gel. Heating rate = 10°C/min, sample amount = 25.4 mg, DTA range = 25 μV 90

Fig. 36. DTA and TG curves for a binary mixture of $CaCO_3$ and Al_2O_3. Heating rate = 10°C/min, sample amount = 26.2 mg, DTA range = 25 μV 91

Fig. 37. DTA and TG curves for the ternary mixture of $CaCO_3$, Al_2O_3 and SiO_2 gel. Heating rate = 10°C/min, sample weight = 34.5 mg, DTA range = 25 μV 92

Fig. 38. Formation of CA and C_3A at 1200°C. The C_5A_3 phase also formed at this temperature 101

Fig. 39. Formation of aluminates at 1250°C 102

Fig. 40. Formation of aluminates at 1300°C 103

Fig. 41. Relation between $K_{GB}t$ and conversion as calculated from the Ginstling-Brounshtein equation and the particle size distribution of Al_2O_3 108

Fig. 42. The Valensi-Carter equations for $C_{12}A_7$, CA and C_3A as functions of conversion 110

Fig. 43. Relation between $K_{VC}t$ and x as calculated from the Valensi-Carter equation for $C_{12}A_7$ and the particle size distribution of Al_2O_3 111

Fig. 44. Relation between $K_{VC}t$ and x as calculated from the Valensi-Carter equation for CA and the particle size distribution of Al_2O_3 112

Fig. 45. Relation between $K_{VC}t$ and x as calculated from the Valensi-Carter equation for C_3A and the particle size distribution of Al_2O_3 113

Fig. 46. Relation between Kt and sintering time for the C_3A phase at 1200°C 114

Fig. 47. Relation between Kt and sintering time for C_3A at 1250°C 115

Fig. 48. Relation between Kt and sintering time for C_3A at 1300°C. Values of (1 - x) were substituted for x in the calculation of Kt except for the beginning period 116

Fig. 49. Relation between ℓn K and $\frac{1}{T}$ for the formation of C_3A 117

Fig. 50. Relation between Kt and sintering time for CA at 1200°C 118

Fig. 51. Relation between Kt and sintering time for CA at 1250°C 119

Fig. 52. Relation between Kt and sintering time for CA at 1300°C. Values of (1 - x) were substituted for x in the calculation of Kt 120

Fig. 53. Relation between ℓn K and $\frac{1}{T}$ for the formation of CA 121

Fig. 54. Relation between Kt and sintering time for $C_{12}A_7$ at 1250°C 122

Fig. 55. Relation between Kt and sintering time for $C_{12}A_7$ at 1300°C 123

Fig. 56. Mechanisms of formation of aluminates: (a) $C_{12}A_7$ is the primary product; (b) CA is the first dominant phase; (c) C_3A is formed as more Ca ions diffuse into the CA phase; and (d) $C_{12}A_7$ is finally formed at the expense of CA and C_3A 127

Fig. 57. Calculated free energy changes as a function of temperature for the indicated reactions 132

Fig. 58. Extraction ratios (recoveries) of Al_2O_3 for different sintering runs. Extraction was done at 65°C for 15 min with a 3% Na_2CO_3 solution 134

Fig. 59. The SiO_2 contents in the filtrates as a function of sintering temperature and time 136

LIST OF TABLES

		Page
Table 1.	Classification of imperfections in crystal	8
Table 2.	Weight loss of Al_2O_3 and SiO_2 after 1 hr at 1300°C	32
Table 3.	Chemical analysis of the pure $CaCO_3$-Al_2O_3-SiO_2 gel mixture	32
Table 4.	Particle size distribution of ground, pure Al_2O_3, SiO_2 gel and $CaCO_3$	33
Table 5.	Free CaO content of the sinters in wt %	60
Table 6.	Residues of the sinters after the maleic acid treatment (in wt % of the original sample)	95
Table 7.	Chemical analysis of the residues from the maleic acid treatment (wt %)	96
Table 8.	Molar ratio of CaO/SiO_2 in the C_2S phase which dissolves in the maleic acid-methanol solution	97
Table 9.	Intensity ratios of the strongest peaks for three aluminates to the d = 2.392 peak of KBr	98
Table 10.	Calibration of d = 2.97 peak of CA under the influence of $C_{12}A_7$	99
Table 11.	Conversions of aluminates in the sinters for different runs	100
Table 12.	Thermodynamic properties of several compounds of interest in this investigation	129
Table 13.	Standard free energy changes (ΔG_T^o) in calories for Reactions 41-44	131

INTRODUCTION

Ever since the 1973 embargo on oil, not only have energy resources become a serious problem for most countries of the world, but also there is a clear warning of potential problems involving many other natural resources.

In the case of energy, the oil importing countries will have to turn to alternative fuels, which in the immediate future can only be coal and nuclear power. In the United States, more emphasis has been put on coal because of its abundance. As a result, the consumption of coal has increased steadily in recent years, as has the production of coal ashes — fly ash, bottom ash and boiler slags. In the year of 1977, the production and collection of total ash climbed to a record of 61.9 million tons (3). The overall utilization of ashes, however, was only 20% for the same year. For fly ash alone, the utilization rate was even lower at 13.3%, while it counted for about 70% of the total ash. The cost of handling these aggregate in an environmentally acceptable manner is reaching staggering proportions, resulting in pressure to develop new mass tonnage applications (3).

The United States is not only dependent upon imports of oil and natural gas, but also upon imports of many other mineral raw materials, such as manganese, chromium, titanium, platinum, aluminum, etc. (51). To ease this dependence, the United States must turn to more recycling, conservation and new technology, as well as to processing low grade ores.

The usual ore from which aluminum is recovered is bauxite, an

alumina hydrate. As early as World War II, the United States began research to develop substitute materials for bauxite because of the increasing demand in war time and also because of very limited domestic reserves. Clay and other alumina bearing ores like alunite and anorthite were the main materials studied (20, 33). But these efforts were abandoned after the war due to economical considerations. Nevertheless, the search for new processes and new materials still went on (1, 72, 83). After the 1973 oil embargo, the United States, in anticipation of a possible critical supply situation in imported bauxite, once again increased the effort to find an economical process to produce aluminum from domestic nonbauxite resources (7). As part of the effort, various methods of extracting alumina from fly ash have been investigated at the Ames Laboratory over the past few years.

Fly ash is comprised of compounds of silicon, aluminum, iron and calcium, and smaller amounts of compounds containing magnesium, titanium, sodium and potassium, plus traces of other elements (13). Silica and alumina are the main constituents in the majority of U.S. fly ashes. Only a small fraction of them is in the form of mullite, $3Al_2O_3 \cdot 2SiO_2$, while the rest exists in glassy form. In the original mineral fraction of coal, clay is the principal source of both silica and alumina. Iron is found in fly ash in both crystalline and glassy forms. Hematite and magnetite are present in a crystalline form. They are formed as a result of the oxidation of pyrite (65, 94). The decomposition of calcite and dolomite at high temperatures accounts for the formation of calcium oxide and magnesium oxide. In addition to the above compounds, the ash particles often contain residual carbon.

This is usually present as black vesicular particles distributed intimately throughout the mass (65, 94).

In order to understand the basic ideas about the extraction of alumina from ores, a review of conventional alumina recovery processes is necessary. Aluminum is usually produced from bauxite by the Bayer-Hall-Heroult process. Raw bauxite is first ground and digested with hot caustic soda to produce a sodium aluminate solution. Impurities, predominantly iron oxide, titania and silica, are left behind as an insoluble residue. The solution is discharged from the digester and the insoluble residue (red mud) is separated by filtration, sedimentation, or both. The wash water is added to the sodium aluminate solution and the clear solution is cooled and stirred with a seed charge of previously prepared hydrated aluminum oxide to precipitate the soluble sodium aluminate as a hydrated alumina. The resulting precipitate is then washed and calcined at 1000°C to produce anhydrous alumina (22, 35). High purity aluminum is produced by electrolysis of alumina from a bath of fused cryolite (1 AlF_3 + 3 NaF) in the Hall-Heroult process (22).

The most troublesome impurity in bauxite is silica. During the digestion, an insoluble sodium aluminum silicate apparently is formed, which carries both soda and alumina into the red mud (84). It is quite essential, then, in selecting ore for the Bayer process, to keep the silica content as low as possible, usually less than five percent. Because of the depletion of domestic reserve of high-grade bauxite, the aluminum industry must consider the use of high-silica bauxites and nonbauxite raw materials, such as fly ash. Many processes to permit the use of these materials are thus studied. These processes

may be broadly divided into three groups: (a) dry processes in which the essential step is a furnacing operating, e.g., sintering with lime or soda to produce soluble sodium or calcium aluminates; (b) wet processes in which the alumina is directly extracted by means of aqueous agent, e.g., the alkaline or acidic extractions; (c) chlorination processes in which aluminum chloride instead of alumina is first obtained. It is then followed by a decomposition or refining stage to produce aluminum metal. This method will eliminate the use of Hall-Heroult process, which has low energy efficiency and serious pollution problems (71).

Since the lime sinter process was studied quite thoroughly by the author, it will be discussed in more detail. A flow sheet of this process is shown in Fig. 1. Limestone is first mixed and ground with the nonmagnetic fraction of fly ash. The mixture is then sintered at 1300°-1400°C to form dicalcium silicate and calcium aluminates. The leaching step is done with 3% Na_2CO_3 solution to convert calcium aluminates into soluble sodium aluminate while leaving most of the silicate behind. Desilication, carbonation and calcination then follow to produce pure alumina (1, 4, 33, 68). Of all these steps involved, only sintering and leaching are different for different raw materials. Thus only these two steps were investigated.

The parameters studied include the sintering temperature and time, the amount of limestone added, the leaching temperature and time, and the concentration and volume of sodium carbonate solution. The results, however, were not quite satisfactory. The recovery ratio of alumina in the ash stayed between 50% and 60% at most. A subsequent

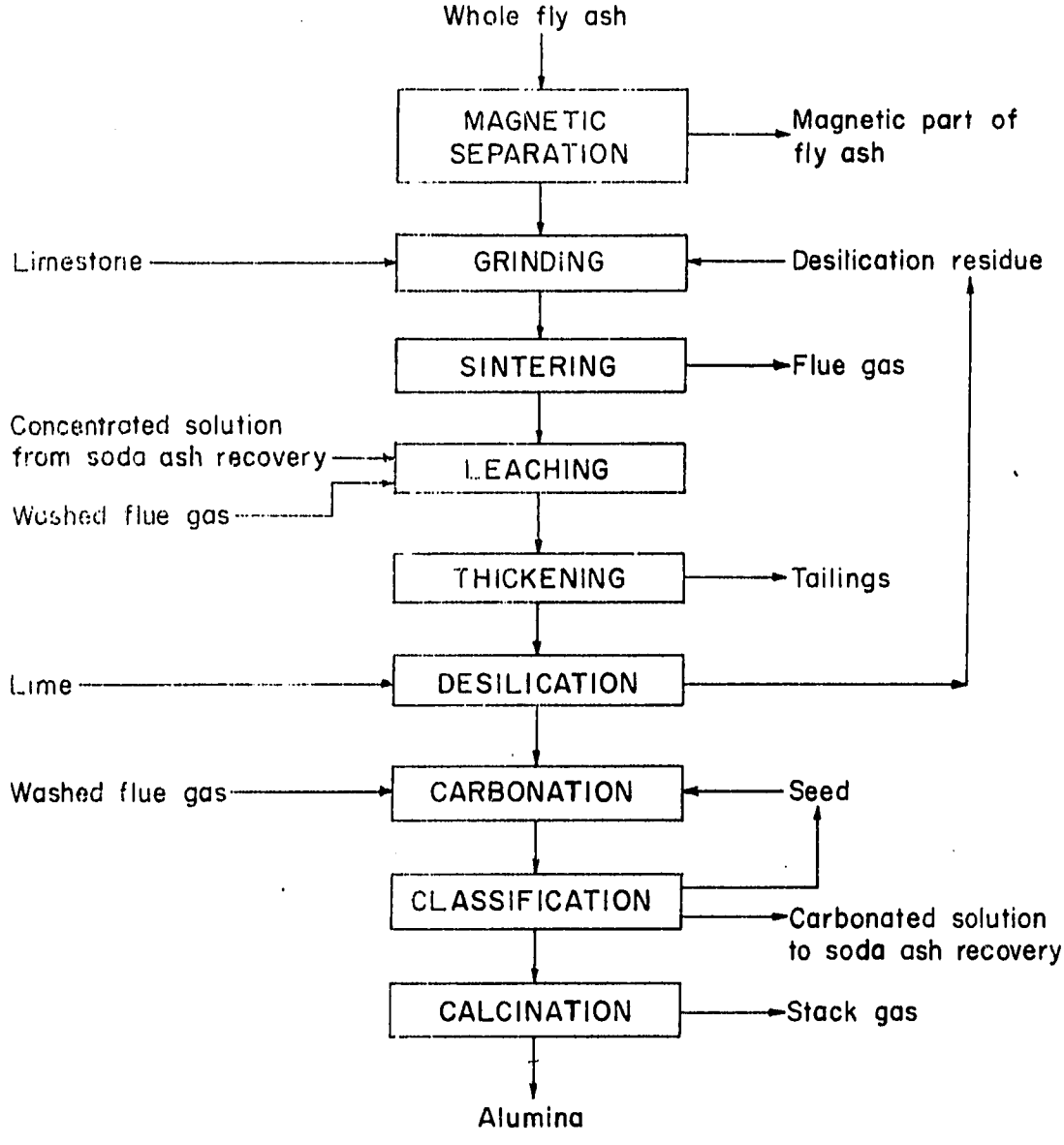

Fig. 1. Lime sinter process for the recovery of alumina from fly ash

economic study showed that an extraction ratio of at least 80% would be necessary for this process to become economically feasible for fly ash.

In order to improve the extraction and to increase our knowledge about the lime sinter process, it was determined that more fundamental work had to be done. It is, therefore, the purpose of this research to study the sintering and leaching steps, especially the former one, in more detail. The atomistic reaction mechanism and kinetics, as a function of the controllable variables, through which the calcium oxide reacts with alumina and silica in the stage and their subsequent reactions with sodium carbonate solution in the leaching stage, have to be determined and understood.

LITERATURE REVIEW

The solid state reactions in general may be classified to comprise (34, 77): (a) the decomposition or transformation of a solid; (b) the reaction of two or more solids with each other; (c) the reaction of a solid with gaseous or liquid phase. In the lime sinter process, the sintering step is an example of solid-solid reactions, while the leaching step belongs to the class of solid-liquid reactions. Since the sintering reactions are the main subject in this research, the discussion will be focused on reactions between solids only. Nevertheless, the basic features of different classes of solid state reactions are very similar to each other. The review made here can be applied to other cases without much difficulty.

Diffusion in Solids

The atoms of a solid, unlike those of a liquid or gas, are constrained within narrow limits and cannot move freely in reactions. In order to understand the atomistic mechanism and kinetics of solid-solid reactions, it is first of all necessary to explain the transport of matter in the reaction product under the action of chemical or electrochemical potential gradients. Since this transport in solids is basically due to the mobility of defects, it is furthermore necessary to understand the behavior of defects in solids (82).

Chemical and structural defects in crystalline solids

The concept of the crystalline solid defines a solid in which the atoms are arranged in a three-dimensional periodic array of perfect order. A basic group of atoms or molecules is repeated in space according to a regular pattern to give the crystal structure. It is, thus, quite impossible to conceive any mechanism for reaction in perfect solids. Defects must be either created or destroyed, move, interact or aggregate in any solid state reaction (27, 78).

Table 1 gives a classification of crystal defects. Associated with these defects, there are electrical defects, which are localized regions of electrical imbalance, to preserve the electrical balance of solids. Free electrons, positive holes and excitons (electron-electron hole pairs) are examples. In addition, there are also thermal defects, called phonons (43).

Table 1. Classification of imperfections in crystal (27)

Point defects:	Vacancies, interstitials, impurity atoms;
Line defects:	Dislocations;
Planar defects:	Surfaces, grain boundaries, planar stacking faults;
Volumetric defects:	Cluster of atoms of different chemical composition, cluster of point defects, impurity-atom vacancy or interstitial complexes, small regions of disorder.

Diffusion mechanisms

In order for microstructure changes or chemical reaction to take place in the solid phase, it is essential for diffusion to occur. Diffusion is local transport of matter under the action of chemical potential gradient or — in the case of diffusion of ions — under the

action of electrochemical potential gradient.

The direct change of atoms without the intervention of a lattice defect is energetically very unfavorable. Diffusion therefore occurs by means of lattice defects. The diffusion may either be surface or dislocation diffusion or bulk diffusion. In all cases imperfections play an essential role (48).

There are two main approaches to diffusion theory: (1) the atomistic approach, where the atomic nature of the diffusing substance is explicitly considered; and (2) the continuous approach, where the diffusing substance is treated as a continuous medium and the atomic nature of diffusion is ignored (61). The second approach in one sense simplifies the problem since it directly relates the initial and final states, but also it is limited in results. A more complete picture of diffusion phenomena is obtained if the first approach is used. Equations can be found relating macroscopic quantities to atomic quantities, such as atom jump frequencies. It is thus more difficult to obtain an equation in this method. As a result, many useful equations are derived from a continuous approach as will be discussed later on.

Whichever theory of atom diffusion is used, we have to start with a consideration of diffusion mechanisms. A number of possible diffusion mechanisms can be identified according to the type of elementary jump which takes the atom from one site to another. These mechanisms may be classified as follows (34, 43, 61, 78, 88): (1) ring exchange; (2) interstitial mechanism; (3) interstitialcy mechanism; (4) vacancy mechanism; (5) dislocation diffusion mechanism; (6) grain boundary

diffusion; and (7) surface diffusion.

Overall, these mechanisms can be divided into three groups. The first mechanism is of the least importance of all, since it needs too much energy to occur. The next three mechanisms are responsible for volume diffusion in solids (Fig. 2). Of the two point defects, vacancies and interstitials, the vacancies usually have a lower energy of formation and are thus more prevalent, especially in close-packed structures (92).

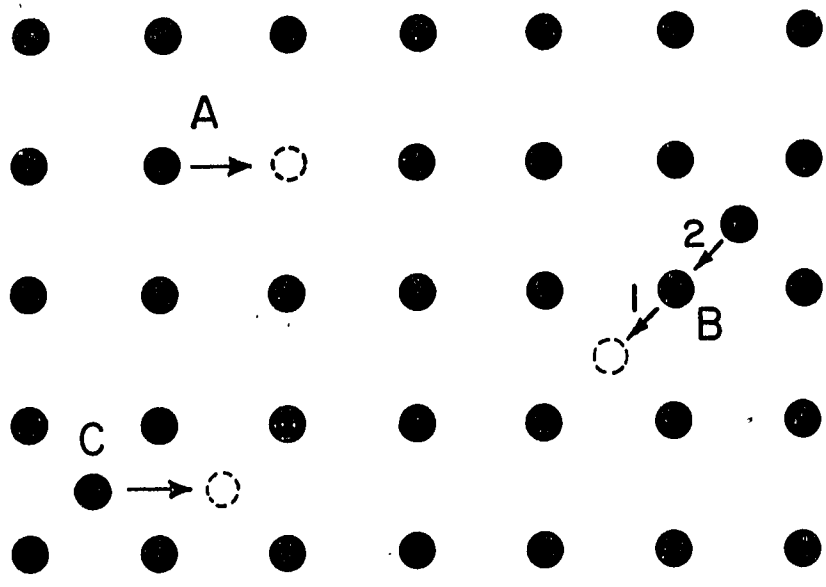

Fig. 2. Mechanisms of lattice diffusion. A — Vacancy diffusion. B — Interstitialcy diffusion. C — Interstitial diffusion

The last three mechanisms in the above list are concerned with diffusion in regions where the regular lattice structure breaks down. It is thus not difficult to imagine that diffusion occurs more easily in these regions of the crystal. However, in chemical process at high temperatures the role played by point defects moving in the crystal lattice tends to predominate over that played by line or surface

defects. In simple terms we may say that for material transport by line or surface imperfections, A and Q in the Arrhenius equation $k = Aexp(- Q/RT)$ are both small, while for transport by point defects A and Q are, by comparison, large (43, 61, 88). As a result, the dislocation or surface diffusion is important at low temperatures, while volume diffusion is important at high temperatures.

Since the individual atoms inside a crystal cannot be viewed directly as they diffuse, our knowledge of their diffusion mechanisms is necessarily indirect. Diffusion will occur predominantly by that mechanisms which requires the lowest activation energy in that particular structure or it can occur by the motion of a particular point defect which is present at equilibrium in appreciable concentration. There are also other criteria which have been used in the past (8).

Reactivity of solids

The chemical reactivity of a gas or liquid is proportional to its concentration. In contrast, the notion of concentration of a solid is usually of little significance, since the atoms are very restricted in their motions (31). Thus the main point on which chemical reactions with solids distinguish themselves from those occurring in a liquid or gaseous phase is the effect of lattice structure, i.e. the existence, the nature and the number of the defects they contain (21, 31).

Point defects in the bulk of a crystal may arise as a result of any of the following ways: (1) thermal equilibrium; (2) irradiation; (3) doping; and (4) mechanical deformation (31, 48). In our case, however, only the effect of temperature is important. It has been shown

(21, 43) that the numbers of both Frenkel (vacancy-interstitial pair) and Schottky (vacancy) defects at a temperature T follow the Arrehenius equation.

A dislocation is the boundary line between that part of a crystal which has undergone slip and that which has not. The slip vector, Burger vector, uniquely describes the magnitude and direction of the slip that has occurred. The energy of a dislocation is generally proportional to the square of the length of this vector (21, 91). This energy is considerable, i.e. dislocations are not in thermal equilibrium with the crystal. They are more or less unavoidable consequences of growth. Dislocations can move or interact with other defects through the mechanisms mentioned earlier. The reactivity of dislocations is generally enhanced by three factors: the extra energy of dislocations, the abnormal stereochemistry at dislocation cores, and catalytic impurities which accumulate preferentially at dislocations (91).

Surface is sometimes called the largest and most significant imperfection of all in solids (79). This is especially true when we are dealing with powders. The gross properties of surface depend upon the possible variations in the behavior of the atoms or electrons in or near the surface region. A large quantity of impurities is usually concentrated at the surface of a solid, as a result of either adsorption or mechanical erosion of the apparatus in which the milling, firing and other processes are applied to solids (11). These impurities can sometimes have an effect on the strength of the lattice of the solid, on its surface energy and other properties. Above all, the surface diffusion always occurs first among all kinds of diffusion mechanisms and is

very important at low temperatures.

So far we have implicitly considered crystalline solids, and we may ask what remains when we are dealing with amorphous substances. According to DeKeyser (21), of the defects which have been considered, only line defects cannot be transported to an amorphous material. Nothing specific has to be added.

Elementary Steps of Solid State Reactions

The individual steps of a solid state reaction depend to some extent on the choice of reaction class, but some important steps are common to all.

All solid state reactions involve at some stage or other the following elementary steps (78):

1. The creation of defects, of which local equilibrium is usually assumed (82).
2. The transport of matter through the solid by some type of defect diffusion mechanism. The diffusion in the reaction product is an especially important step. The rate of diffusion is in some cases the rate-determining step in solid state reactions.
3. The association of defects into small cluster or aggregates without separation of a new phase. The cluster of defects or photophase in the host crystal may be referred to as a prenucleus. This is the first step toward the formation of reaction products.

4. The transformation of the prenucleus into a small crystal of the product phase with the creation of the necessary conditions for growth. This small volume of the new phase is called a nucleus.
5. Growth of the nucleus by an interface diffusion process or by direct addition at the interface of atoms from another phase.

Kinetics of Solid State Reactions

At equilibrium a system is at its lowest energy state for the composition, temperature, pressure and other conditions imposed on it. The equilibrium situation is usually represented graphically by phase equilibrium diagrams. The primary use of thermodynamics and phase diagrams in our studies is to allow the prediction of whether a given system is at equilibrium or whether a given reaction will occur. This is a very powerful tool, but it is only a first step, since it leaves unanswered the questions of how the reaction proceeds and how fast it proceeds. Besides, the importance of the activation energy, the small contact surface area of the reagents and the high diffusion resistance to the process may make thermodynamically probable reactions practically impossible. This refers especially to reactions in crystalline mixtures. Therefore, correct conclusions on the nature of such reactions will follow only from comprehensive thermodynamic and kinetic investigation.

As mentioned above, a solid state chemical reaction is composed of many elementary steps. The reaction rate will then be determined

by the slowest of these processes. Generally, the kinetic equations derived for solid state reactions are based on: (1) diffusion control; (2) phase-boundary reaction control; (3) nucleation and growth control; and (4) the concept of an order of reaction (85).

Diffusion-controlled reactions

The simplest case is one-dimensional diffusion process. The interface always remain in contact and the volume change is sufficiently small that a dense product is formed. The reactivity of the reactants remain constant on both sides of the reaction interface so that the rate of diffusion is given by

$$dy/dt = Dk/y \tag{1}$$

where k is a constant, D is the diffusion coefficient and y is the diffusion layer thickness. On integration, we obtain

$$y^2 = kDt \tag{2}$$

The square of the thickness of the new phase is proportional to the diffusion coefficient and time. That is, the rate of new phase formation follows a parabolic rate law (43).

Jander applied the above principle to spherical particles and derived his own kinetic equation. He considered a sphere of radius r of component A, the complete surface of which was reacting with component B and forming a reaction product of thickness y. Then the volume of unreacted material at time t was given as:

$$V = (4/3)\pi(R - y)^3 = (4/3)\pi R^3(1 - x) \tag{3}$$

where x is the fraction of the original sphere which has reacted. Equating Eqs. (2) and (3) yields the well-known Jander relationship:

$$K_J t = (1 - (1 - x)^{1/3})^2 \qquad (4)$$

A plot of $(1 - (1 - x)^{1/3})^2$ versus t should be a straight line (14, 43).

The assumptions used in Jander's model were (38):

(a) The reaction is diffusion-controlled.

(b) The product is not miscible with any of the reactants.

(c) The reacting particles are all sphere of uniform radii.

(d) The ratio of the volume of the product to the reactant is unity.

(e) The increase in thickness of the product layer follows the parabolic law; i.e. the reaction interface is a plane.

(f) The diffusion coefficient of the species is not a function of time.

There are many weaknesses in Jander's model because of the many assumptions made in his analysis. Jander's equation was verified preferentially for small degrees of conversion of the reagents. The deviation between experimental data and theoretical value becomes larger at large x (11, 14).

Kröger and Ziegler improved Jander's equation by assuming that the diffusion coefficient of the transported species was inversely proportional to time (37, 38). Their equation is:

$$K_{KZ} \ln t = (1 - (1 - x)^{1/3})^2 \qquad (5)$$

Zhuravlev, et al. (11, 38) modified the Jander relation by

assuming that the activity of the reacting substances was proportional to the fraction of the unreacted material (1 - x). Their equation is:

$$K_{ZLT}t = ((1/1 - x)^{1/3} - 1)^2 \quad (6)$$

Ginstling and Brounshtein (30) arrived at a model using Jander's assumptions except the parabolic rate law. They noticed that the parabolic law is applicable only when the surface area remained constant; however, when they considered spherical particles, this surface actually decreased in area as the reaction proceeded. They derived instead of Eq. (2) the following equation based on steady state diffusion:

$$y^2(1 - 2y/3R) = K't \quad (7)$$

Their final equation is:

$$K_{GB}t = 1 - 2x/3 - (1 - x)^{2/3} \quad (8)$$

Carter (14) improved the Ginstling-Brounshtein model by accounting for differences in the volume of the product layer with respect to that of the reactants. He used Z to represent the volume of the reaction product formed per unit volume of the reactant consumed. His equation which was also developed earlier by Valensi (38) from a different starting point is generally referred to as the Valensi-Carter equation:

$$K_{VC}t = Z/(Z-1) - (1 + (Z - 1)x)^{2/3}/(Z - 1) - (1 - x)^{2/3} \quad (9)$$

Dunwald and Wagner (38) derived an equation for solid state reaction based on a solution to Fick's second law for diffusion:

$$1 - x = 6/\pi^2 \sum_{n=1}^{\infty} 1/n^2 \exp(- n^2\pi^2 Dt/R^2) \qquad (10)$$

where $\pi^2 D/R^2 = K_{DW}$ and n = an integer series. If we only take the first term of the series, we will obtain the following equation:

$$K_{DW}t = \ln(6/\pi^2(1 - x)) \qquad (11)$$

Attempts (36) have also been made to introduce the Kröger-Ziegler idea into Ginstling-Brounshtein's and Valensi-Carter's equations. The modified equations will have terms of lnt instead of t.

There is one inherent assumption in all the models; i.e. one of the two reactants is in excess amount so that the conversion is described by referring to the fraction of the reactant of less amount reacted. Another fact about these models is that they are based on the reaction of spherical particles of the same radius. There have been attempts to introduce particle size distribution into a workable model. Sasaki (80) developed such a model based on Carter's equation. He considered the reactant of less amount to have a particle size distribution and was divided into n groups by size. The radii of each group were set up according to the following relation:

$$r_{10},\ r_{20}(= ar_{10}),\ \cdots\cdots\cdots,\ r_{n0}(= a^{n-1}r_{10}) \qquad (12)$$

The overall conversion is then calculated by summing up the contribution from each group. Gallagher (28) made a similar analysis based on the log normal distribution and Dunwald-Wagner equation.

In cases where the reaction starts only at the contact zones between particles, Jander's assumption that the surface of one component is

continuously and completely covered with particles of the other component is obviously not always valid (38, 46). To compensate for this deficiency, Komatsu (46) introduced into the Jander equation the mixing ratio of the two components, the ratio of the radii of the two components, and a parameter which describes the packing state of the powders. In the case of a constant number of contact points, his equation is:

$$K_J t \cdot (au/au + 1)^m = (1 - (1 - x)^{1/3})^2 \qquad (13)$$

where $a = r_B^3 p_B / r_A^3 p_A$, $u = W_A/W_B$, and m is the parameter to describe the state of packing in the real system; r_A, r_B, p_A, p_B, W_A and W_B are radii, densities and total weights of components A and B, respectively.

Another common assumption used in the above equations is that only one component of the reactants can diffuse through the product layer. Komatsu and Uemura (47) developed recently several kinetic equations for the counterdiffusion system of powder components. They considered the conditions when the radii of the two components are either markedly different from or nearly equal to each other.

Gordeev and Sychev (32) recently introduced a new concept into the kinetics of solid state reactions. They assumed that the resistance to the diffusion of the thickening product layer grows and consequently at a certain value of conversion x_p, under the selected conditions, the rate of conversion is equal to zero. The introduction of such a limitation into Eq. (1) gives:

$$dy/dt = K'(1/y - 1/y_p) \qquad (14)$$

Then from Eq. (3), they derived their kinetic equations:

$$\frac{K_{GS}t}{3(1-(1-x_p)^{1/3})^2} = \frac{(1-x)^{1/3}-1}{1-(1-x_p)^{1/3}} - \ln\left(1+\frac{(1-x)^{1/3}-1}{1-(1-x_p)^{1/3}}\right) \quad (15)$$

In general, all the above equations are capable of describing the kinetics of certain solid state reactions, but not every solid state reaction. This is simply because most solid systems, especially those consisting of powder materials, have a high number of variables which can influence reaction rates.

Phase-boundary controlled reactions

The general assumptions made in this aspect are:

(a) Diffusion through product layer is very rapid;

(b) The reaction rate is proportional to the surface of the fraction of unreacted material;

(c) The nucleation step occurs virtually instantaneously so that the surface of each particle is covered with a layer of product;

(d) The reaction rate is phase-boundary controlled.

Reaction models in this category are largely lacking because of the unknown structure of the solid/solid phase boundary on an atomic scale and also the unknown kinetic behavior of the atoms or ions (36, 38, 81). For a sphere reacting from the surface inward the relationship between conversion and time is:

$$K_{PB}t = 1 - (1-x)^{1/3} \quad (16)$$

Nucleation and growth controlled reactions

This approach considers the nucleation of the product at active sites and the rate at which the nucleated particles grow. It includes mainly reactions involving decomposition and transformation of solids. There are three successive stages in this mechanism: (1) a prenucleus process leading to the formation of a large number of nuclei; (2) an accelerating period; and (3) the final period when the nuclei are coalescing (34). Several equations have been developed in the past for this mechanism.

The simplest case is the power law: $x = C_1 \cdot t^n$; where C_1 is a constant. The values of n are determined empirically. Nucleation according to a cubic law followed by three-dimensional growth to give an overall sixth-power law has been observed (34). This provides the clearest case of a power law arising from the combined effects of nucleation rate and growth rate.

Another similar empirical equation is the exponential laws: $x = C_2 \exp(kt)$. This equation applies to processes in which the rate of nucleation is affected by the amount of reaction x which has already occurred, so that nucleation is self-catalyzed (34).

The most general form of the kinetic equations in this category is:

$$\ln(1 - x) = - kt^m \qquad (17)$$

which is sometimes referred to as the Avrami-Erofeev equation (11, 34, 38). This model corrects for the errors due to the coalescence of nuclei and the "ingestion" of some potential nucleus-forming sites by the advancing reaction zones.

Kinetic equations based on the concept of an order of reaction

Equations of the following kind have been applied to solid state reactions mainly for analytical convenience. The general differential equation takes the following form:

$$dx/dt = k(1 - x)^n \tag{18}$$

The corresponding integrated form is:

$$kt = (1/(1 - x)^{n-1} - 1)/(n - 1) \tag{19}$$

where n is the so-called order of the reaction. For certain values of n, Eqs. (18) and (19) lead to some of the equations based on physical models. When n = 2/3, Eq. (19) becomes identical to Eq. (16). However, n usually has a value without any obvious physical significance. Because of this fact, this method has only very limited applicability to solids.

Examination of Reactions in Real Systems

We have thus far discussed only the theoretical features of general solid state reactions. In this section, however, specific reactions of systems of CaO, SiO_2 and Al_2O_3 will be discussed with the aid of the principles reviewed earlier.

CaO-SiO_2 system

Four compounds have been isolated in this system: $CaO \cdot SiO_2$, $3CaO \cdot 2SiO_2$, $2CaO \cdot SiO_2$ and $3CaO \cdot SiO_2$. The reactions of their formation in crystalline mixtures, constituting the physiochemical basis of Portland cement clinker technology, have been studied in great detail.

It is generally agreed that the primary product at the interface between CaO and SiO_2 is $2CaO \cdot SiO_2$, regardless of the initial ratio between CaO and SiO_2 (11, 25, 66). The start of formation of the reaction products of the CaO-SiO_2 system is noted at about 700°C-850°C, depending upon the activities of the reactants and the presence of traces of impurities (11, 66). When bulk diffusion begins, $3CaO \cdot 2SiO_2$ will be formed on the SiO_2 side and $3CaO \cdot SiO_2$ (when temperature reaches 1300°C) on the CaO side. Finally, after further diffusion on the SiO_2 side, $CaO \cdot SiO_2$ will be formed. The reactions between CaO and SiO_2 are always carried out by monodiffusion of Ca ions, rather by counterdiffusion of both Ca and Si ions. Figure 3 is a schematic diagram of the sequence of CaO-SiO_2 reactions.

Of the four possible compounds in this system, only $2CaO \cdot SiO_2$ and $3CaO \cdot SiO_2$ are likely to be encountered in the sintering processes for the production of alumina. Tricalcium silicate is formed by the reaction between calcium oxide and dicalcium silicate at temperatures between 1250°C and 1900°C (11, 23, 49, 54). Its formation is enhanced somewhat in the presence of magnesia, manganese oxide and chromium oxide (11). Lopez, et al. (54) studied the beginning stage in the $3CaO \cdot SiO_2$ formation reaction and found that the mechanism which controls the overall rate of the reaction product is that of the nucleation of $3CaO \cdot SiO_2$, according to Avrami-Erofeev's model.

The formation kinetics of dicalcium silicate has been studied quite extensively (25, 26, 55, 66, 75). Montierth, et al. (66) studied the initial stages of the reaction between calcium oxide and quartz in the temperature range of 700-850°C. They concluded that the reaction

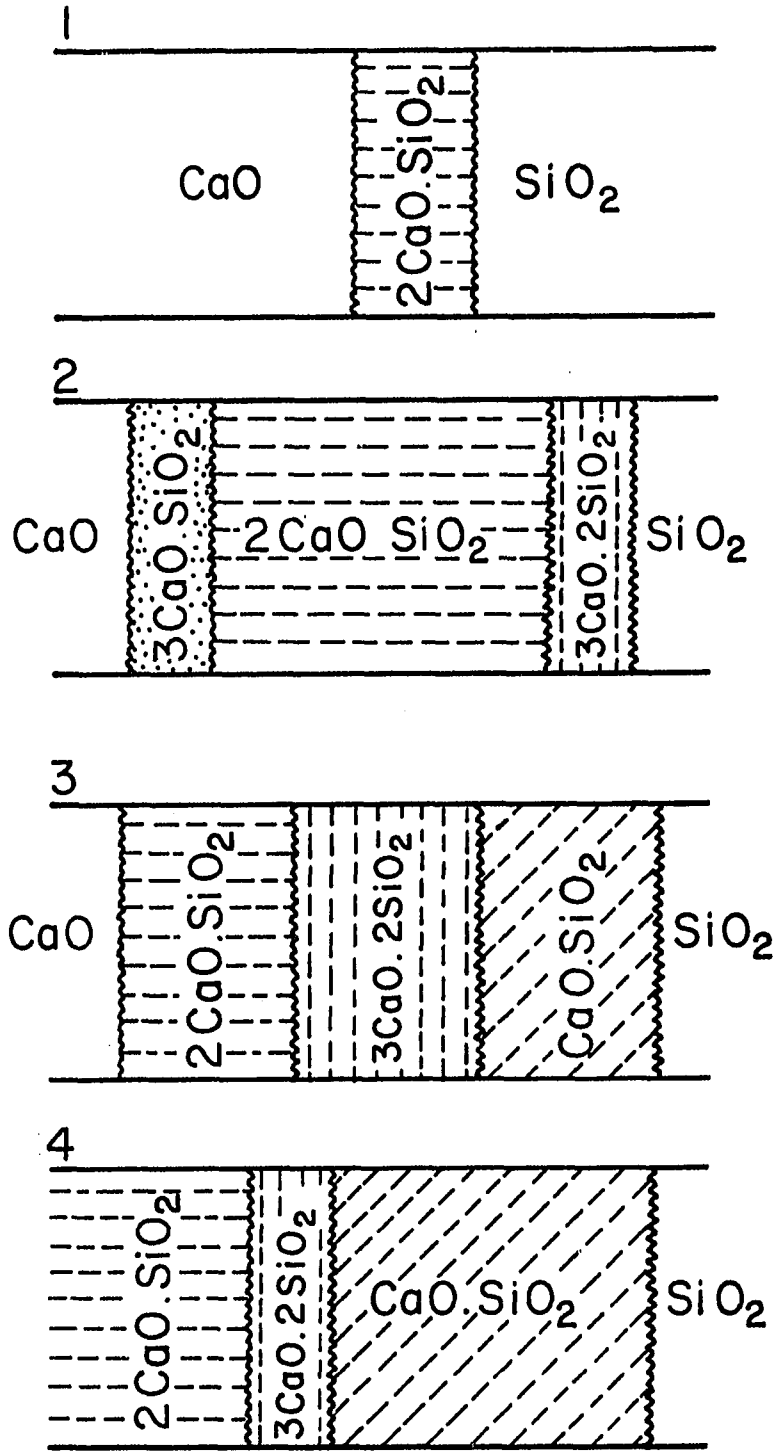

Fig. 3. Basic stages in the formation of monocalcium silicate when CaO and SiO_2 react

occurs in two distinct steps at the initial stages. The first step is believed to be solid solution reaction of calcium into the quartz. The second step, obeying parabolic reaction kinetics, is thought to be a diffusion-controlled process in the product layer.

Luginina (55) stated in his paper that with or without the presence of mineralizers the formation of dicalcium silicate follows the Ginstling-Brounshtein's equation up to practically complete conversion. While recently, P'yachev, et al. (75) found in their experiments that the generalized Avrami-Erofeev's equation fits best the formation kinetics of $2CaO \cdot SiO_2$ from polydispersed mixtures. Their results also indicate a change in the formation kinetics as time passes. In the first period the reaction takes place on the surface and lasts for only a few minutes (0.3-3 min). The second period, limited by diffusion through the product layer, begins at different degrees of completion of the reaction, depending on the particle size of the initial components. The studies made by Fierens and Picquet (26) were above 1400°C. Their findings, however, showed that the reaction is controlled by the motion of interfaces, i.e. the chemical reaction at the phase boundary.

There are four well-established forms of dicalcium silicate. Of practical importance is the polymorphic transformation from beta- to gamma-Ca_2SiO_4, which is accompanied a 10% increase in volume and which is responsible for the disintegration into fine powder of cement clinkers and other lime-rich silicate slags. This "dusting" phenomena is very desirable in the lime sinter process, because it not only saves energy otherwise required for grinding, but also provides large surface area for the leaching step that follows (16). There are, however, many

factors which can prohibit this transformation. One such factor is the firing temperature. At each temperature below the inversion point there is a critical size for the nuclei of the new phase. If a nucleus exceeds the critical size it will grow and form a crystal; if it is less than the critical size it will then revert to the old phase. When none of the nuclei exist at the firing temperature, an incubation period, which may be indefinite, is necessary for the conversion to occur (69).

The most important factor which can influence the beta-gamma transformation is the presence of impurities. Zerfoss and Davis (99) discussed their effects under the headings of physical and crystal-chemical stabilization. Physical inhibition of the transformation is characterized by the isolation and constraint placed on Ca_2SiO_4 grains by the vitreous or crystalline material. For crystal-chemical stabilization, a solid solution is usually formed, which consequently lowers the inversion temperature. Preservation of the high temperature form is favored in such a case, partly because the degree of supersaturation on cooling is less and partly because the impurity has to be precipitated before the lower temperature modification can occur (69). Of ordinary oxides, small amounts of CaO, SiO_2, Al_2O_3, Fe_2O_3, MgO and TiO_2 do not prevent this transformation, while B_2O_3, Cr_2O_3, Na_2O and K_2O do (9, 24, 69).

CaO-Al_2O_3 system

Four stable compounds occur in this system: $3CaO \cdot Al_2O_3$, $CaO \cdot Al_2O_3$, $CaO \cdot 2Al_2O_3$, and $CaO \cdot 6Al_2O_3$. Another compound $12CaO \cdot 7Al_2O_3$,

can only be stable in the presence of moisture (39, 70, 93). As a matter of fact, it has been given a formula of $11CaO \cdot 7Al_2O_3 \cdot Ca(OH)_2$. A sixth compound, $5CaO \cdot 3Al_2O_3$, is definitely a metastable one (15). Of these compounds, $CaO \cdot 6Al_2O_3$ and $CaO \cdot 2Al_2O_3$ will be less important in the lime sinter process than others.

For the reactions between CaO and Al_2O_3, some researchers (11, 58) think that $CaO \cdot Al_2O_3$ is the primary product, while others (6, 40) indicate that $12CaO \cdot 7Al_2O_3$ will be formed at first. Williamson and Glasser (97), however, concluded from their results that no one calcium aluminate is preferentially formed as a first, nonequilibrium reaction product. Nevertheless, they all agree that the reactions are carried out by the diffusion of Ca ions into alumina. The diffusion of Al ion will not be noticeable until at least 1200°C (58).

The sequence of products of the reaction between CaO and Al_2O_3 has been shown as follows (45): $CaO/C_3A/C_{12}A_7/CA/CA_2/CA_6/Al_2O_3$, where C stands for CaO and A for Al_2O_3. The thickness of the layer obeys the parabolic law, indicating that the reaction is diffusion-controlled (40). Kohatsu and Brindley (45) observed the amounts of various product phases from the reaction sintered pellets of CaO and Al_2O_3 at 1330°C and found that comparison of the development of reaction products with physical properties (melting points and oxygen ion densities) points to low melting points and low packing densities, favoring high diffusion and large product development. Of the five aluminates shown above, the $C_{12}A_7$ phase has the lowest melting point and the lowest oxygen ion density, followed by C_3A, CA and CA_2. The CA_6 phase is, however, at the other end in terms of these properties.

Al_2O_3-SiO_2 system

The only stable compound in this system is mullite, $3Al_2O_3 \cdot 2SiO_2$. Three forms of anhydrous aluminum silicate of composition, $Al_2O_3 \cdot SiO_2$, along with other hydrated aluminum silicates, however, do occur in nature.

Studies made in this system are relatively fewer than those in the preceding two systems. This is probably because compounds of alumina and silica alone do not occur in Portland or high-alumina cement. Marinov, et al. (62) recently studied the formation of mullite and found that at the initial stage of process, the nucleation and chemical reaction are process-controlled mechanisms. Nevertheless, as a whole, the process is diffusion-controlled. The relatively low diffusion rates of both aluminum and silicon ions compared to calcium ion make this binary system less important than others.

CaO-Al_2O_3-SiO_2 system

An equilibrium phase diagram of this ternary system is shown in Fig. 4 (53). There are two ternary compounds: gehlenite ($Ca_2Al_2SiO_7$ or C_2AS) and anorthite ($CaAl_2Si_2O_8$ or CAS_2). The formation of gehlenite from oxides, according to the book by Budnikov and Ginstling (11), occurs in the following manner. At first the compounds of $C_{12}A_7$ and C_2S are formed at 900-1000°C. Later the aluminate reacts with silica, and the orthosilicate with alumina, giving the basic mass of gehlenite. We also obtain at this stage CA and CS, which react slowly with each other to complete the formation of gehlenite. The synthesis of anorthite from mixtures of oxides follows the same pattern as gehlenite. The

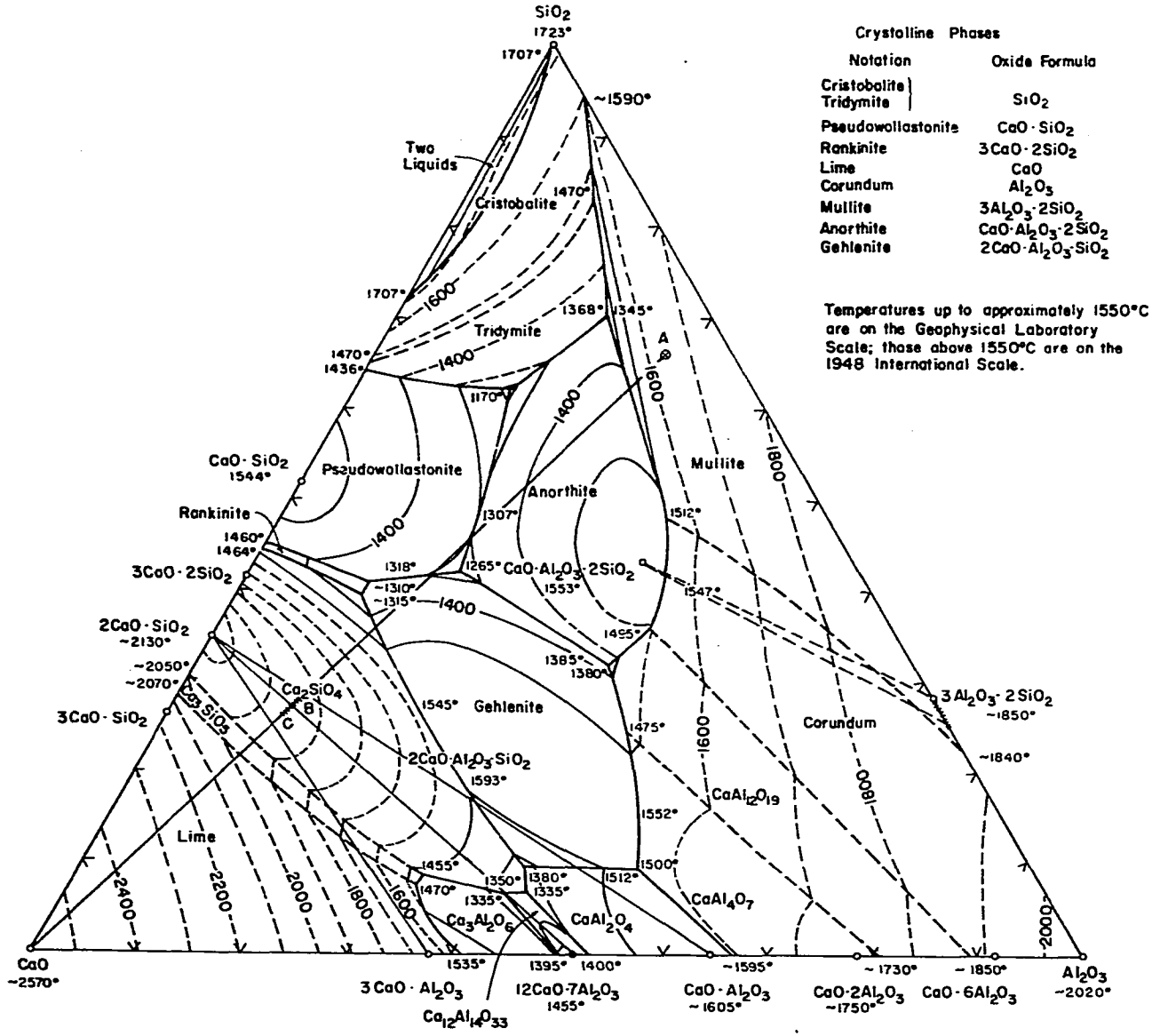

Fig. 4. Phase diagram of the $CaO-Al_2O_3-SiO_2$ system

formation of binary compounds of $C_{12}A_7$, CS, C_2S and CA are first observed. The gehlenite forms as an intermediate compound. Only after prolonged heating or very high temperature, will the synthesis of anorthite be completed (11).

However, these two ternary compounds are not likely to be encountered in the study of the lime sinter process. The composition of mixtures in this process is designed to stay within the subsystem of C_2S-$C_{12}A_7$-CA. Naturally, the equilibrium compounds in such a subsystem will be C_2S, $C_{12}A_7$ and CA themselves.

Our purpose in this research is to first develop the kinetics of the formation of calcium aluminates and silicates based on studies from pure components, and then to apply the information gained to the lime sinter process with nonmagnetic fly ash as the raw material. The effects of the addition of Na_2CO_3 and other mineralizers on the above results will then be studied to fully understand the sintering reactions in industrial processes.

EXPERIMENTAL PROCEDURE

It is well-known that fly ashes from different sources may have different chemical composition and physical properties. In fact, it is also difficult to characterize a typical fly ash from a power plant. In view of the widely varying nature of fly ash, a particular sample was sought that represented as closely as possible the average chemical composition of nine available midwestern power plant fly ashes. A fly ash from a power plant in Milwaukee, Wisconsin was selected as the sample to be used in a series of investigations (16). Since the present work is a continuation of the earlier investigations, it was decided to use a sample which contained alumina and silica in the same relative amounts as used before. In order to eliminate the influences of other elements existing in fly ash, it was decided to use pure components of calcium carbonate, aluminum oxide and silica gel as the starting materials.

Materials and Preparation of Pellets

Pure, reagent-grade $CaCO_3$, Al_2O_3 and SiO_2 gel was used. The loss on ignition at 1300°C was determined at first in order to obtain the true assay of alumina and silica. Both alumina and silica gel have large surface areas and absorb a certain amount of foreign materials on their surfaces. The data obtained are shown in Table 2. A modified, single-point B.E.T. method using nitrogen as the absorbate gave the specific surface areas of Al_2O_3 and SiO_2 gel as 229 and

Table 2. Weight loss of Al_2O_3 and SiO_2 after 1 hr at 1300°C

Component	Weight loss (%)[a]	Average (%)
Al_2O_3	11.30; 11.59; 11.60	11.50
SiO_2 gel	6.80; 6.40; 6.89; 7.13	6.80

[a]Includes L.O.D.

341 m^2/gm.

Weighted samples of these three components were then mixed and ground for 6 hours in a ball mill to insure the homogeneity of the mixture. Chemical analysis was conducted on this mixture to check its composition. Results are shown in Table 3.

Table 3. Chemical analysis of the pure $CaCO_3$-Al_2O_3-SiO_2 gel mixture

Component	Weight percentage (%)	Average (%)
CaO	62.60; 61.09; 62.83; 61.41	61.98
Al_2O_3	11.20; 11.68; 11.78; 11.43	11.53
SiO_2	26.90; 27.23; 25.39; 27.16	26.67

Since it is important in the calculation of kinetic equations, the particle size distribution of Al_2O_3 along with that of SiO_2 gel and $CaCO_3$ was determined on a Coulter counter. Samples of these compounds were ground individually in a ball mill also for 6 hours before they were subjected to the size analysis. Data from these analyses are given in Table 4. The distribution of Al_2O_3 was also plotted as shown in Fig. 5.

Table 4. Particle size distribution of ground, pure Al_2O_3, SiO_2 gel and $CaCO_3$

Group No.	Diameter μ	Weight fraction (%)		
		Al_2O_3	SiO_2	$CaCO_3$
1	0.63[a]	1.8	—	0
2	0.794	2.9	—	0.2
3	1.0	5.3	1.2	0.5
4	1.26	7.9	1.5	1.0
5	1.59	12.4	2.0	2.5
6	2.0	13.4	2.9	5.1
7	2.52	12.0	3.6	9.6
8	3.17	8.5	4.5	14.5
9	4.0	6.0	5.2	19.7
10	5.04	3.9	6.6	20.3
11	6.35	3.4	8.7	13.3
12	8.0	3.2	9.7	8.6
13	10.08	4.5	12.1	3.7
14	12.7	5.7	14.4	0.7
15	16.0	6.6	15.4	0.3
16	20.2	2.4	9.2	0
17	25.4[a]	—	3.1	—

[a]Fraction includes particles smaller or larger than the diameter shown.

Before the sintering step, pellets were made out of this mixture by using a hydraulic pressing machine (Model B manufactured by Fred S. Carver, Inc.). A load of 2000 lb was used throughout the experiments. Since the particles hold together quite well, no water was added. The pellets had a diameter and a height of about 1/2 inch. Nine pellets stacked in three piles in a platinum boat were used for each run.

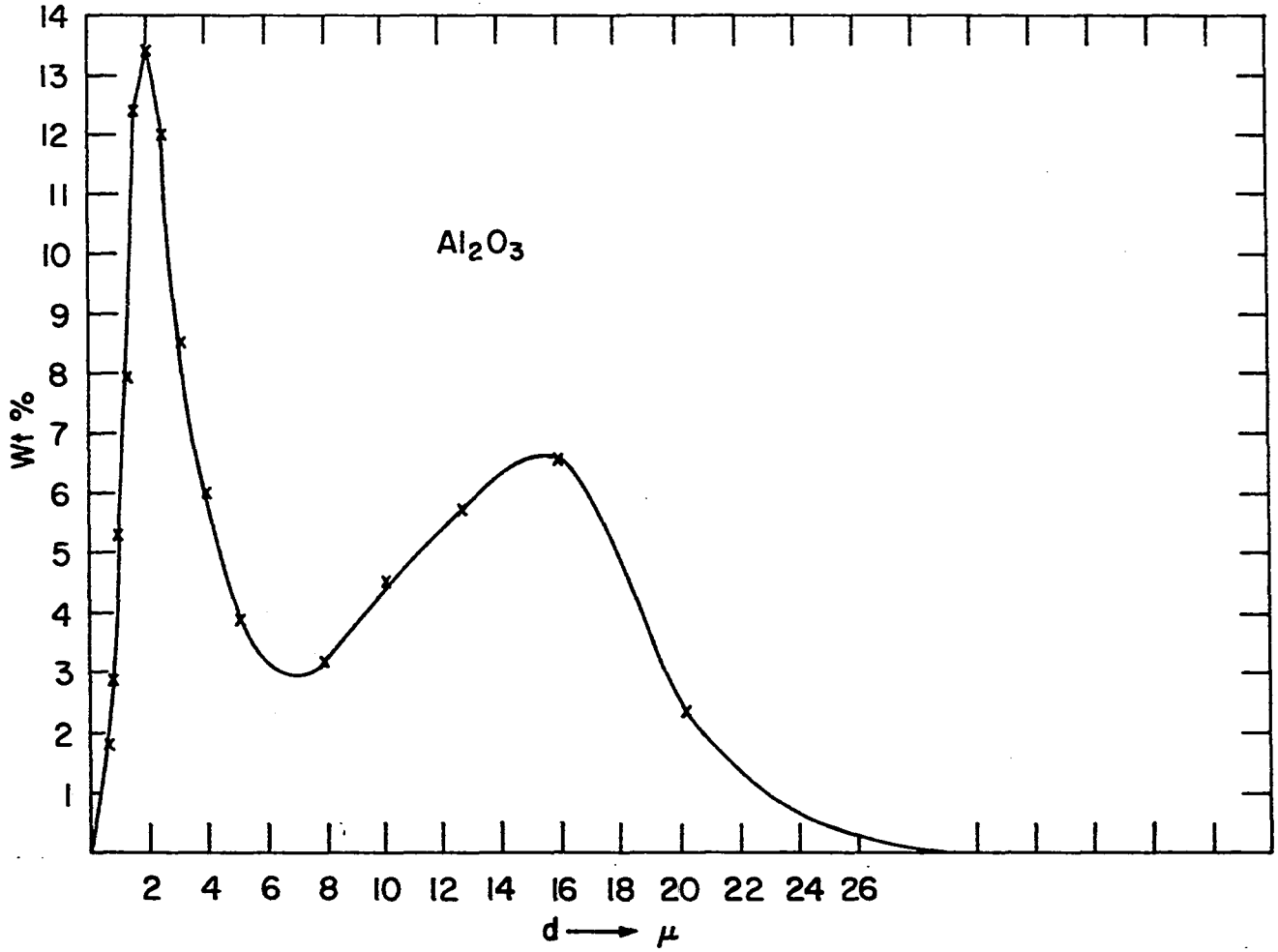

Fig. 5. Particle size distribution of ground, pure Al_2O_3

Furnacing the Pellets

The furnace used in this sintering work is a product from Lindberg Hevi-Duty Division of Sola Basic Industries (Fig. 6). The furnace is equipped with a programmer which consists of a ramp programmer, a set-point unit and a digital timer. It is capable of controlling the temperatures to better than $\pm$ 1°C. The furnace uses silicon carbide as the heating element and is designed such that the temperature of a wide region in the center is maintained at the established setpoint. The temperature distribution along the tube in the furnace was measured once with a Pt/Pt-13% Rh thermocouple and the results shown in Fig. 8 were obtained.

In view of the fact that the decomposition of $CaCO_3$ takes a certain amount of time to complete, it was decided to preheat the pellets to first completely decompose the $CaCO_3$ without causing any reaction between CaO and Al_2O_3 or SiO_2. Through trial and error, it was found that the best pretreatment was obtained at 850°C and 2 hours. Another reason for this pretreatment was based on kinetic analysis considerations which will be discussed later.

Since it takes time for the furnace to heat up from 850°C to the desired temperatures such as 1200°C and 1300°C, the platinum boat which holds the pellets was placed in the open end of the tube while the furnace was heating up. The boat was then pulled into the center region as quickly as possible using a platinum wire attached to the front end of the boat after the furnace had been at the desired temperature for several minutes. After a fixed period of isothermal heating,

Fig. 6. The Lindberg hevi-duty tube furnace used in the sintering runs

Fig. 7. The X-ray furnace used in the high-temperature X-ray work

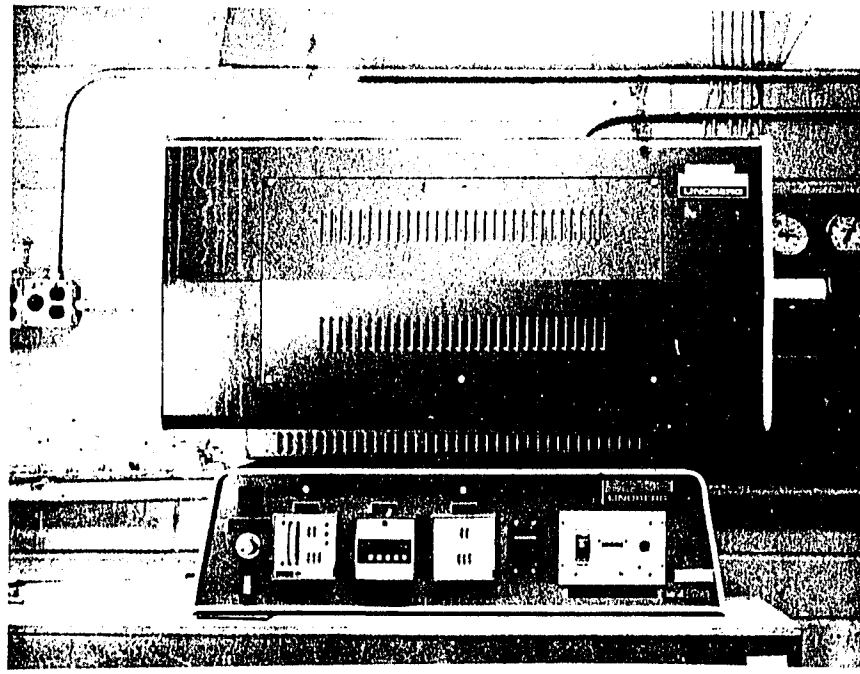

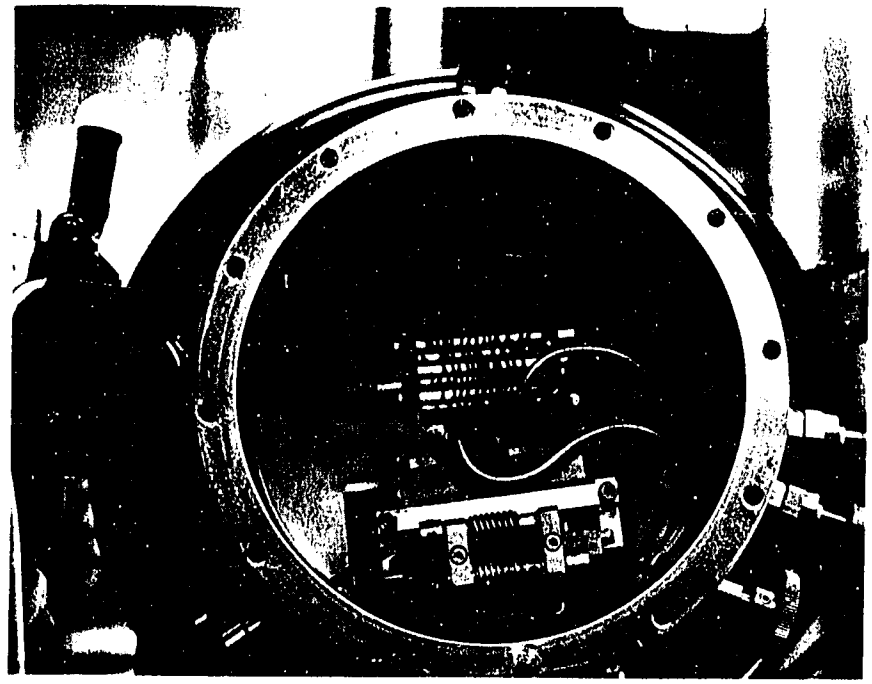

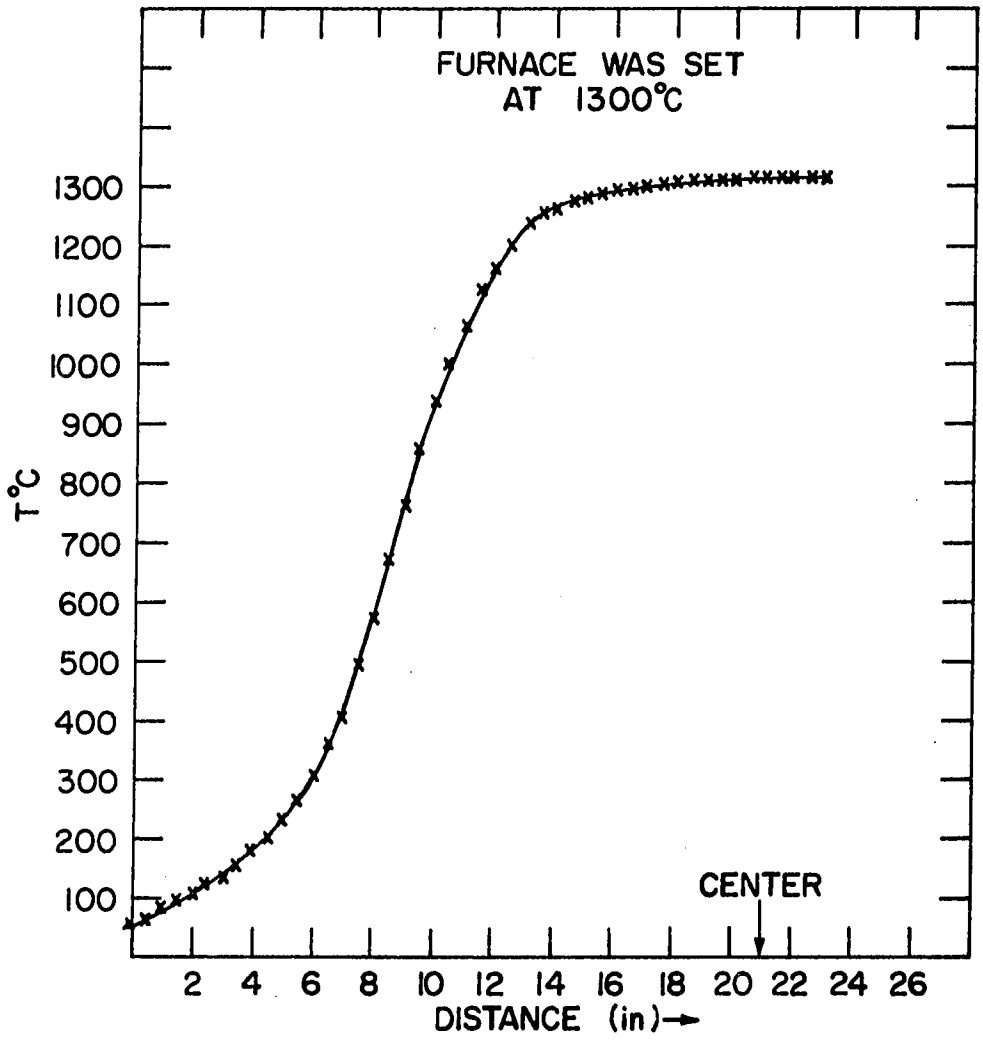

Fig. 8. Temperature distribution along the tube when the Lindberg furnace setpoint is 1300°C

the pellets were pulled out quickly and quenched in the air. They were then stored in a desiccator for further experiments. The sintering runs were made at 1200°C, 1250°C, 1300°C and 1350°C and for different periods of time from 0.2 hour up to 10 hours.

Qualitative Analysis of the Sintered Products

In an attempt to understand the chemical reactions taking place during the sintering step, a qualitative analysis was carried out. The following experiments were performed to identify the reactions that occurred and compounds formed during the high temperature treatment.

X-ray diffraction analysis

X-rays are generated when electrons from a heated filament are accelerated and strike the metal target. The X-ray spectrum thus produced consists of a broad, white continuum with superimposed sharp peaks which are characteristic of the target metal (44). The spectrum has then to be filtered to give relatively narrow bandwidths of X-rays for practical work.

The X-ray equipment used here was supplied by Philips Electronic Instruments. Iron was the target metal and manganese was used as a filter. Thus the $K\alpha_1$ line at $\lambda = 1.936$ of iron was used for diffraction work throughout the experiments. The common detectors used in association with X-ray machines are Geiger, proportional or scintillation detectors. A scintillation detector was employed here. The detected signal was then amplified and displayed digitally on a counter and also graphically on a recording chart.

X-rays are electromagnetic waves and can be diffracted by crystals in the same way as light is by a diffraction grating. Diffraction is governed by Bragg's Law: $N\lambda = 2d \sin \theta$, where N = an integer, λ = the wavelength of the X-ray, d = the interplanar spacing of the crystal, and θ = the angle between the crystal surface and the X-ray beam (19,

44). A given substance will always produce the same characteristic diffraction pattern, whether it is present in the pure state or as one constituent in a mixture. This fact is the basis for the diffraction method of chemical analysis.

Qualitative analysis for a particular substance is accomplished by identification of the pattern of that substance. Since more than one substance can have the same or nearly the same d values for its strongest lines, it is necessary to use the three strongest lines to sufficiently characterize the pattern of an unknown. The American Society for Testing Materials (ASTM) began to collect and classify diffraction data in 1940, and published these data in the form of a set of 3" x 5" index cards. Numerous supplementary sets have appeared from time to time since then (19). Data from ASTM cards and from a paper by Ampian (2) were used to identify the unknowns in this work.

It is essential for the most satisfactory results that (a) the size of crystallites be sufficiently small, and that (b) preferred orientations of the crystallites be held to a minimum (44). The first condition was achieved by grinding the samples in a mortar for at least 15 min. This reduction in size has the added benefit of reducing preferred orientation, provided a uniform mounting technique is adhered to. The specimen holders used in this work were rectangular aluminum plates about 2 mm thick containing a rectangular window in which a powder sample is placed. The cell-filling procedure used here was adapted from the book by Klug and Alexander (44). It is as follows:

1. Cover the face side of the aluminum plate with a clean glass

slide bound firmly in place with tape.

2. Place the plate, face down, on a flat surface and sift an excess of powder into the cavity.
3. Tamp the surplus gently but thoroughly with the edge of a spatula. Slice off the surplus powder with a razor blade.
4. Sift on a loose layer of powder about 1/16 inch thick. Press gently but firmly with the flat blade of the spatula to compress the powder. Slice off the surplus again and cover it with another clean glass slide.
5. Turn the assembly over and remove the other glass slide. It is then ready for X-ray diffraction.

Scanning Electron Microscopy (SEM)

The scanning electron microscope is one of the powerful instruments which permit us to observe and correctly explain phenomena occurring on a micron or submicron scale. It is often used for the characterization of heterogeneous materials and surfaces on such a local scale (67, 95). When a focused electron beam impinges on a specimen surface, it produces several types of signals which include secondary electrons, back-scattered electrons, low-loss electrons, Auger electrons, light, characteristic X-rays and continuous X-ray spectrum. In SEM, the primary signal of interest is the variation in secondary electron emission. When the beam is swept in a raster across the surface of the specimen, secondary electrons are collected to form images correspondingly. Since the secondary electron yield is confined near the beam impact area and the focus depth of SEM is large, it can produce images

at relatively high resolution and also with a three-dimensional appearance.

In this research work, a SEM unit manufactured by Japan Electron Optics Laboratory (JEOL) was used. A thin layer of graphite suspension in isopropyl was first applied to the top of an aluminum holder. This suspension served both as a glue and a conducting material. Powdered samples were then spread onto the surface. After the sample was dried, it was coated in vacuum by about 200Å thickness of gold. The sample was then ready for examination.

Electron microprobe analysis (EMPA)

Electron microprobe analysis has very much in common with scanning electron microscopy. The main difference is in the signal collected after the electron beam strikes the specimen. In EMPA, characteristic X-ray lines are collected. These lines with a spatial resolution of the order of 1 μm, are very useful in the determination of elemental compositions in the sample. Moreover, quantitative data can often be obtained with very good accuracy. Another important feature of the EMPA is the capability for obtaining X-ray signal scanning pictures. The X-ray pictures show the elemental distribution in the area of interest. The attractiveness of this form of data gathering is that detailed micro-compositional information can be directly correlated with optional metallography.

The EMPA unit used in this work was manufactured by American Research Laboratory (ARL). It was equipped with a Tracor-Northern NS-880 multichannel analyzer having a Kevex Si(Li) solid state energy

dispersive detector. This detector made possible quick, simultaneous analysis of all elements with atomic number greater than 10. Powdered samples were dispersed on a clean pyrolytic carbon disc using ultrasonic vibration. The sample was then coated by carbon by a D.C. sputtering device. In case of pellet samples, which were usually very hard, a metal disc was used as the base. Polishing of the pellet was always done in this case to ensure a flat surface for examination.

The areas of interest were selected by optical examination followed by electron micrograph and X-ray micrographs for Si, Al and Ca. On the basis of these pictures, specific areas were then selected for X-ray quantitative analysis. Standards of known composition for Si, Al and Ca were chosen as SiO_2, Na_3AlF_6 and CaF_2. The relative X-ray intensity ratios between the element of interest in the specimen and the same element in the standard was obtained. This ratio, however, had to be corrected for several effects to give a correct result (98). The effects include: (1) the difference in electron scattering and retardation in the specimen and the standard, i.e. the so-called atomic number effect; (2) absorption of X-rays within the specimen; (3) fluorescence effects; and (4) continuum fluorescence. This method is often referred to as the ZAF method. It was used in the calculation of data reported in this work.

High temperature X-ray analysis

X-ray diffraction is one of the most powerful tools for the identification of crystalline materials in the study of solids. A diffractometer equipped with a high-temperature furnace allows extension

of this X-ray diffraction technique to any investigation in which a crystallographic characteristic of the sample varies with temperature. It has been employed in a wide variety of problems such as decomposition, oxidation-reduction, phase transformation, solid state reaction, etc. (12).

A X-86-N3 series high-temperature diffractometer attachments manufactured by Materials Research Corporation were used in this work. These units normally use a platinum-40% radium strip heater as the method of heating. However, a pure platinum strip heater was used in this work instead. The heating element was made into the shape shown in Fig. 9. Powdered sample was mounted on top of the strip which was then simply clamped onto two water-cooled electrode posts. An auxiliary heating assembly was provided to reduce thermal gradients across the face of the heating element and through the thickness of the specimen on the heating element. Although it has a limit of 1000°C, this element tends to reduce the thermal gradient when the specimen is at a temperature higher than 1000°C. A picture of the entire unit is shown in Fig. 7.

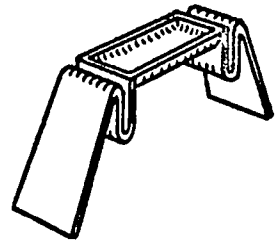

Fig. 9. The heating element for high-temperature X-ray work

A proportional temperature controller with a Pt/Pt-13% Rh thermocouple was used to control the temperature automatically. It usually

took only seconds to reach the desired temperature which was then maintained very stably. An optical pyrometer was also used to observe the temperature throughout the experiment. Based on this observation, the thermal gradient was estimated at about 15°C across the depth of the sample. The powdered sample was at first heated at 850°C for one hour. The temperature was then increased by 50°C increments until 1250°C was reached. At each increment, the temperature was also maintained for one hour. The X-ray diffraction pattern was always taken during the last 20 min of each heating period. Individual pure components were tested first, followed by binary and ternary mixtures.

Differential thermal analysis (DTA)

A substance subjected to thermal treatment may undergo physical or chemical changes. The method of differential thermal analysis (DTA) determines these changes as a function of temperature. DTA is generally performed by heating a sample and a thermally inert reference material in rather close continguity and measuring temperature differences between them. Evaluation of the DTA data will help to understand the physical or chemical changes in the sample during treatment. It is not only of use or assistance in qualitative analysis, but also in many cases in quantitative analysis (73, 76). Most DTA units are also equipped with thermal balances to enable the operator to carry out a thermogravimetric analysis at the same time.

There are many factors which can affect the resulting experimental curves (29, 96). These factors are generally divided into two categories: (a) instrumental factors and (b) sample characteristics. The

former category includes: (1) furnace atmosphere; (2) furnace size and shape; (3) sample holder material; (4) sample holder geometry; (5) wire and bead size of thermocouple junction; (6) heating rate; (7) speed and response of recording instrument; and (8) thermocouple location in sample. The second category includes: (1) particle size; (2) thermal conductivity; (3) heat capacity; (4) packing density; (5) swelling or shrinkage of the sample; (6) amount of sample; (7) effect of diluent; and (8) degree of crystallinity. The most important of these factors are sample size, heating rate and furnace atmosphere.

The DTA unit that was used in this research work was a desk-top type differential thermal and thermogravimetric analyzer manufactured by Rigaku Company. It consisted of six cmponents: TGA unit, temperature controller, DTA amplifier unit, sample holder, furnace and recorder. A high temperature furnace and sample holder were used to insure the required temperature of 1300°C. The furnace was made up of an equalizing beryllia cylinder which was wound using platinum-rhodium wire. Two shield cases made of alumina were used to prevent heat loss and also to improve temperature distribution within the furnace. The sample holder was a part of the moving system of a thermobalance. The holder conveyed to the external system not only the weight changes in the sample but also the thermal changes through a thermocouple. The Pt/Pt-13% Rh thermocouple was spot-welded to the bottoms of the two heat-pick-up-discs which are symmetrical about the supporting rod. On top of these discs rested the sample pan and the reference pan.

The reference material used here was α-Al_2O_3 powder, which was heated at 1300°C for several hours before using. The powdered samples

were packed uniformly into the pan, usually with the help of a sample crimper. The sample pan was very small with a diameter of about 0.4 cm and a height of about 0.2 cm. The pan can hold up to 40 mg of material depending on the density.

Base line shift was a problem for DTA curves. However, it was corrected by turning the slope adjustment knob. Through trial and error, it was found the best setting was 94 for DTA sensitivities of $\pm$ 25 μV and $\pm$ 50 μV/full scale, which were used throughout the work.

Quantitative Analysis of the Sintered Products

In order to express the formation of calcium aluminates in the sintering step explicitly in kinetic equations, the quantities of the compounds formed have to be measured. The following experiments were thus performed.

Maleic acid treatment

Since the formation of calcium aluminates is of primary concern and the quantities formed are relatively small for accurate X-ray quantitative work, it is of great advantage to preferentially remove the dicalcium silicate phase from the samples. One such method was found through extensive literature search. This method employs a 20% methanol solution of maleic acid (90). For each gram of sintered sample, 100 ml of solution is used. The solution (with sample) is stirred at room temperature for 20 min before being filtered. The residue is then dried and burnt at 900°C for about one hour. After cooling, it is then stored in desiccator.

The maleic acid, by virtue of its carboxyl group configuration, can react with a single silicate particle to produce a low molecular weight complex, soluble in methanol. Its effectiveness was found in this research to be somewhat dependent on its freshness. A freshly prepared solution would dissolve a little more silicate than one that had been prepared for awhile. It was also found, during experiments, that free CaO (unreacted CaO) dissolve in this solution. On the other hand, the aluminates did not react with maleic acid at all, even when a fresh solution was used.

Chemical analysis

This analysis was done on the residues from the maleic acid treatment only. It was intended mainly as a check for the quantitative X-ray work to be conducted later. The residues were analyzed for their oxide constituents according to the procedures set forth in the 1977 Annual Book of the American Society for Testing and Materials Standards (87).

The general procedures for these analyses are as follows (87): The sample to be analyzed is ashed under standard conditions and ignited to contact weight. Two solutions are prepared from the residue. Solution A is obtained by fusing the sample with sodium hydroxide followed by a final dissolution of the melt in dilute hydrochloric acid. Solution B is prepared by decomposition of the sample with sulfurnic, hydrochloric and nitric acids. Solution A is used for the analysis of SiO_2 and Al_2O_3 by spectrophotometric methods. Solution B is used for CaO by the chelatometric titration method.

In addition to the above analysis, free CaO content was also

determined for all sintered products before they were treated with maleic acid. The technique employed here is also from the ASTM Standards. It is based on the solution of free CaO in a hot glycerol and alcohol solution and the subsequent titration of the dissolved lime with an alcoholic solution of ammonium acetate (86).

Quantitative X-ray diffraction analysis

This is the most important analysis method used in this research, since it can measure directly the quantities of compounds existing in the samples.

The capability of X-ray diffraction as a method for quantitative analysis was pointed out as early as 1919 (19, 44, 100). The fundamental idea in the use of this method is that the intensity of the characteristic peaks for a substance is proportional to the concentration of that substance in the sample. However, the relation between intensity and concentration is not generally linear, since the diffracted intensity depends markedly on the absorption coefficient of the mixture and this itself varies with the concentration. The common method to eliminate this "matrix effect" is to use an internal standard and to construct calibration curves to relate the intensity and concentration of a substance from samples containing known concentrations of the substance and a constant concentration of the internal standard used (19, 44, 64). However, it is a rather tedious procedure. Lately, Chung (17) developed a new matrix-flushing method which eliminates most, if not all, of the calibration work in the use of internal standards. His theory will be described briefly here.

The basic equations relating the intensities of diffracted rays and the percentage composition are:

$$I_i = Ki \frac{X_i/\rho_i}{\mu_t} \tag{20}$$

and

$$\frac{I_i}{I_i^o} = X_i \frac{\mu_i}{\mu_t} \tag{21}$$

where

I_i, I_i^o = intensities of X-rays diffracted by a selected plane of component i and pure compound i, respectively

Ki = a constant which depends upon the geometry of the diffractometer and the nature of component i

X_i = weight fraction of i

ρ_i = density of component i

μ_i = mass absorption coefficient of pure component i

μ_t = mass absorption coefficient of the total specimen exposed to primary X-rays, including component i, internal standard and reference material added, if any.

The μ_i and μ_t are called the absorption effect, which complicates X-ray diffraction analysis. So the best way of approaching this problem is to flush all these μ factors out of the intensity-concentration equation. In order to achieve this, a flushing agent, potassium bromide in our case, is added to a sample of n components.

$$X_f + \sum_{i=1}^{n} X_i = 1 \tag{22}$$

Then from Eq. (21):

$$\frac{I_i}{I_i^o} = X_i \frac{\mu_i}{\mu_t}$$

$$\frac{I_f}{I_f^o} = X_f \frac{\mu_f}{\mu_t} \qquad (23)$$

We have:

$$\left(\frac{I_i}{I_f}\right)\left(\frac{I_f^o}{I_i^o}\right) = \left(\frac{X_i}{X_f}\right)\left(\frac{\mu_i}{\mu_f}\right) \qquad (24)$$

For a binary mixture of component i and the flushing agent with one-to-one weight ratio, similar to Eq. (24), we have

$$\left(\frac{I_i}{I_f}\right)\left(\frac{I_f^o}{I_i^o}\right) = \left(\frac{\mu_i}{\mu_f}\right) \qquad (25)$$

For the sake of simplicity, let $k_i = \frac{I_i}{I_f} = \left(\frac{\mu_i}{\mu_f}\right)\left(\frac{I_i^o}{I_f^o}\right)$. Then we arrive at the following working equation:

$$X_i = \left(\frac{X_f}{k_i}\right)\left(\frac{I_i}{I_f}\right) \qquad (26)$$

In this research work, pure compounds of $C_{12}A_7$, CA and C_3A were synthesized by mixing appropriate amounts of $CaCO_3$ and Al_2O_3 together. The mixtures were first pelletized and heated at 1300°C for 2 hours, then ground if necessary, and examined by X-ray diffraction. If the synthesis was not complete, they would be treated a second time until the X-ray diffraction patterns showed only the existence of the desired compounds. The respective patterns obtained were the same as those reported by Ampian (2).

Since the intensity of the major peak of the flushing agent KBr used here was relatively strong, a one-to-four weight ratio between the KBr

and the pure compounds or the samples was used throughout the experimentation. The mixing of potassium bromide and our samples was done by putting the materials into a small glass bottle along with several small glass beads to promote mixing. The bottle was then put into the ball mill, along with styrofoam to keep the bottle in position, and rotated for 6 hours. During this operation, the bottle was taken out at least once to check whether there was excessive sample adhering to the bottle wall. After the mixing, the mixture was ground in a mortar for another 15 min.

The respective peaks used for quantitative work for these compounds were: d = 4.89 for $C_{12}A_7$, d = 2.97 for CA, d = 2.70 for C_3A and d = 3.292 for KBr. The integrated intensity of each peak was measured on a nuclear counter in terms of number of counts obtained. The background counts were measured both in front of and behind the corresponding peak and were taken as the average value of those two measurements. Since the intensity of FeKα radiation is not very strong, large slits, 4^o for inlet slit and 0.05^o for receiving slit, and a slow scan speed (2θ $1/8^o$/min) were used. A total of ten measurements were done for each sample to minimize the statistical errors associated with this analysis.

For peaks of CA and C_3A, there would be influences from the peaks of d = 2.99 and d = 2.68 of $C_{12}A_7$. The influence of $C_{12}A_7$ on CA was determined by mixing different proportions of these two compounds and measured the intensity of CA in them. A calibration curve was thus constructed by calculating the differences in intensities measured compared to those expected. The curve obtained is shown in Fig. 10.

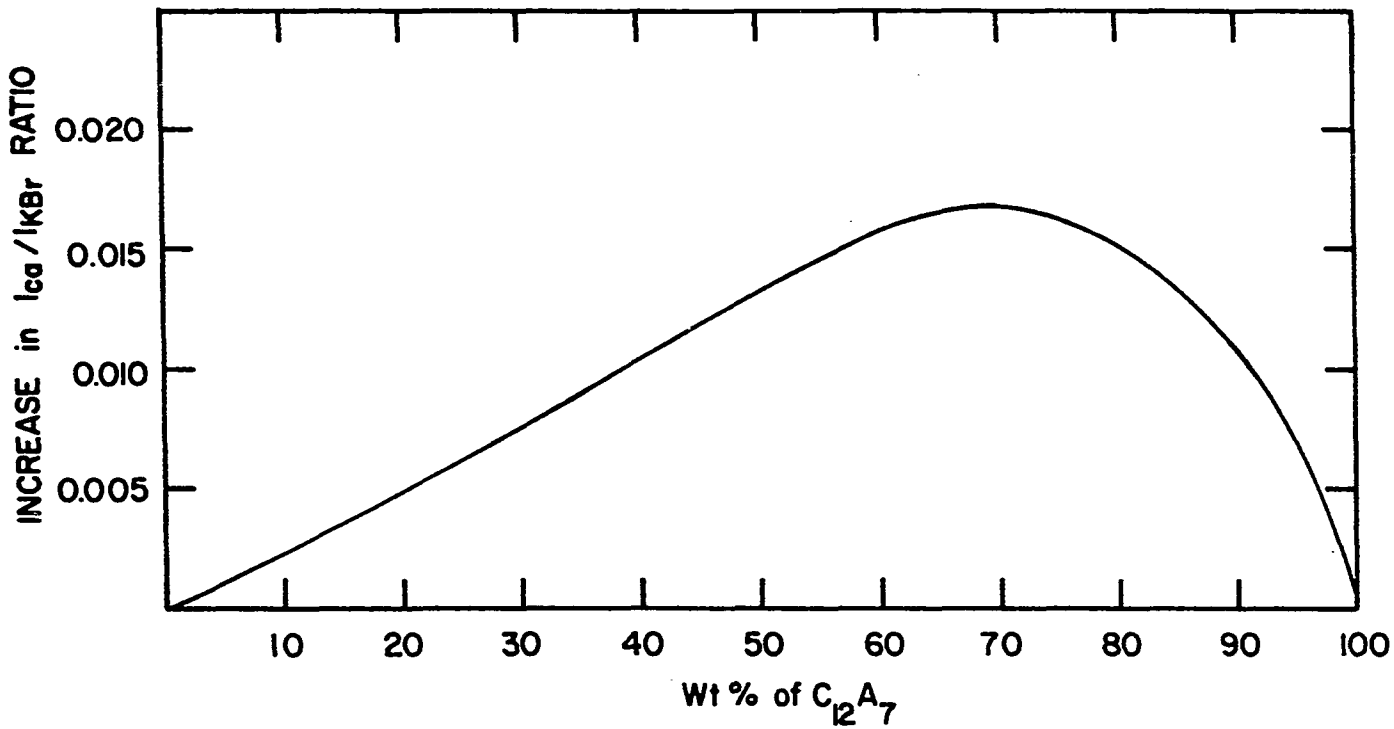

Fig. 10. Influence of $C_{12}A_7$ on the d = 2.97 peak of CA

The situation for C_3A was, however, a little different. The strongest peak of C_3A obtained from the sintering runs was d = 2.69 instead of d = 2.70 as obtained from pure C_3A compound. It was thus impossible to use the synthesized pure C_3A to construct a calibration curve like that for CA. Graphical resolution had to be used to separate the peak of C_3A from that of $C_{12}A_7$ empirically. Luckily this had only to be done for runs from the 1300°C series. In other cases, either the $C_{12}A_7$ phase did not appear or its amounts were too little to have any significant effect.

Leaching of the Sinters

Most of the sinters passed 325 mesh naturally. The small fraction which was larger than this size was ground to pass 325 mesh before it was extracted. Weighed samples were extracted with 3% Na_2CO_3 solutions using constant stirring to prevent settling. The extraction time was 15 min and the temperature was 65°C. Sufficient sodium carbonate solution was added to provide 1.67 moles of Na_2CO_3 for each mole of Al_2O_3 calculated to be present in the weighed samples. The extract was immediately filtered off and the residue washed with hot water. The filtrate was then analyzed for alumina and silica and the residue was examined using the X-ray diffraction method.

Analysis of the Extracts and Residues

The amount of alumina in the extract was determined by a complexometric titration (74). This is a simple and rapid procedure to determine

aluminum in solution. The extracts were first acidified to pH = 2 and then an excess of 0.05M CDTA (1.2-diaminocyclohexane tetra-acidic acid) was added. The pH was next brought to 5-5.5 using hexamethylenetetramine. Several drops of 0.5% xylenol orange was added as an indicator. The solution was titrated with 0.05M lead nitrate. The consumption of CDTA gave the sum of Fe and Al. Since there was no iron in the pure material samples, this number gave the amount of Al only.

The silica content of the extract was determined using the atomic absorption method. The AA unit used was a model 373 manufactured by Perkin-Elmer. Standards of known concentration of SiO_2 were first prepared and measured. The concentrations were chosen to give linear relationship between the absorption and the concentration. Measurements of the absorption of the samples were then compared to those of the standards to obtain the concentrations of SiO_2 in the extracts.

The residues, after being dried, were examined using the X-ray diffraction method described before. The purpose was to find out what products were formed as a result of the leaching action, and thus to know what reactions occurred during the leaching step.

DISCUSSION OF RESULTS

The exploratory experiments conducted in this research were intended to provide some basic information about the reactions between alumina and calcium oxide in the sintering step of the line sinter process. The design of this particular set of investigations enabled an evaluation of the kinetic formation of aluminates and their subsequent solubility in the leaching step. In so doing, the results of each experiment are presented and discussed on the basis of observed experimental trends and direct experimental results.

Results of Qualitative Analysis of the Sinters

The results of each of the following experiments will be discussed individually. Then conclusions based on all these data will be drawn to give a more detailed picture about the formation mechanism of the aluminates encountered in the sintering step.

X-ray diffraction analysis

This technique was applied to all the sinters and the residues of these sinters after the maleic acid treatment to preferentially remove the dicalcium silicate. A few representative X-ray patterns are given in Figs. 11-14.

The X-ray pattern of the powder from the 850°C, 2-hr pretreatment showed the existence of CaO and also a small amount of β-C_2S. The finding of β-C_2S at this temperature agrees with results reported by others (60, 66). The X-ray pattern of this sample after being leached

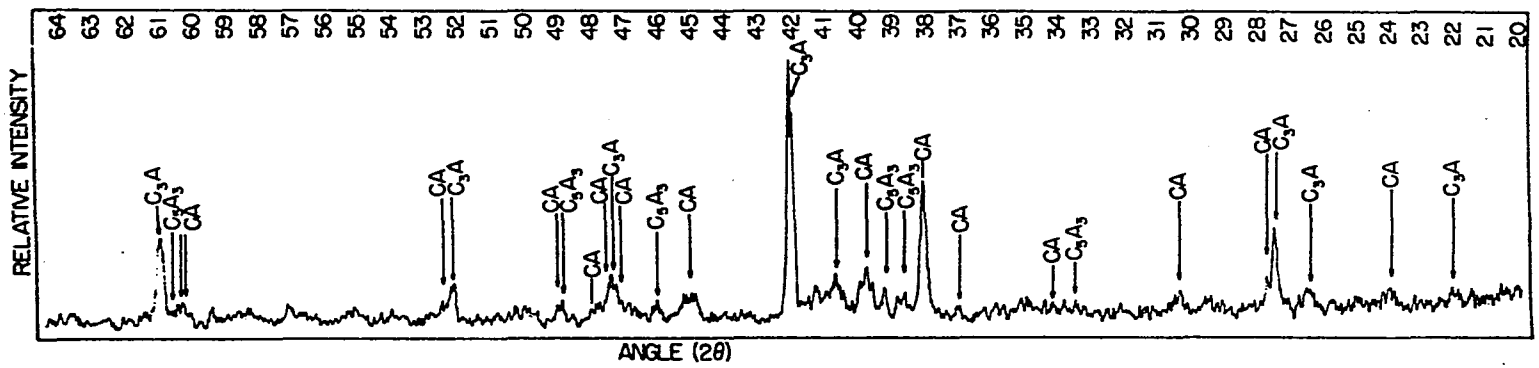

Fig. 11. X-ray patterns of the sinter (1200°C, 1 hr) after being leached by maleic acid-methanol solution. CA, C_3A and C_5A_3 were formed

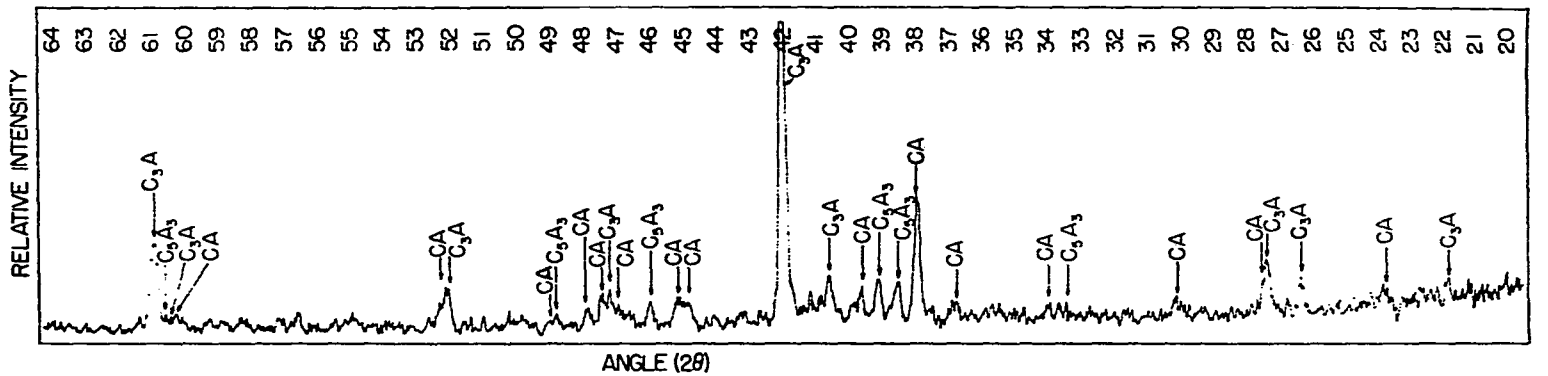

Fig. 12. X-ray patterns of the sinter (1200°C, 4 hr) after being leached by maleic acid-methanol solution. The intensities of the peaks of C_3A and C_5A_3 increased, while that of CA remained at about the same level

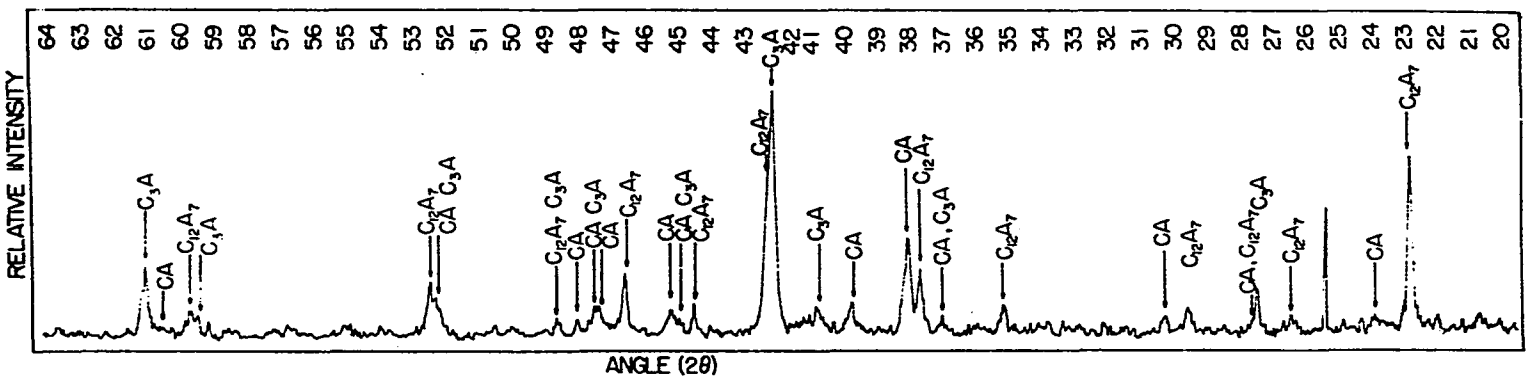

Fig. 13. X-ray patterns of the sinter (1300°C, 1 hr) after being leached by maleic acid-methanol solution. Three phases, CA, C_3A and $C_{12}A_7$ were found

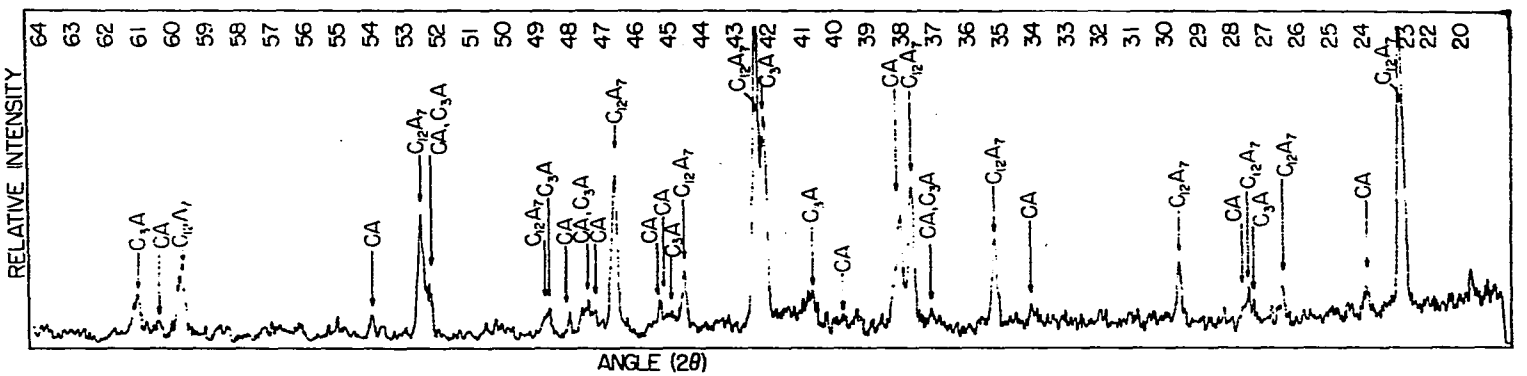

Fig. 14. X-ray patterns of the sinter (1300°C, 4 hr) after being leached by maleic acid-methanol solution. Both CA and C_3A decreased, but $C_{12}A_7$ increased

by maleic acid revealed only the existence of SiO_2 and Al_2O_3. The formation of some CA at this stage is possible, since at the site where the strongest peak of CA would have been found there was a small but definite peak. Intensities of other peaks of CA were probably too small to be detected.

The strength of peaks for free CaO was found to decrease with the increase of either sintering temperature or sintering time, which was an indication that CaO gradually disappeared through reaction with either the SiO_2 or Al_2O_3 powders. Data of free CaO content as obtained by chemical analysis are given in Table 5.

Table 5. Free CaO content of the sinters in wt %

Sintering temperature	Sintering time (hr)						
	0.2	0.5	1.0	2.0	4.0	7.0	10.0
1200°C	12.72	6.64	3.41	1.58	0.50	0	0
1250°C	12.0	5.0	2.26	1.1	0	—	—
1300°C	1.52	0	—	—	—	—	—

The C_2S was found in both β and γ crystalline forms. The general trend in each temperature series was for β-C_2S to be found after the shorter sintering times. With an increase in sintering time, the amount of γ-C_2S was found to increase as indicated by the intensities of the peaks on the X-ray patterns. The nuclei of the C_2S phase formed at low temperatures or short sintering times was probably smaller than the critical size necessary for the transformation of the high-temperature phase into the more stable low-temperature phase. Thus, the dusting phenomena associated with this transformation was not observed under

these conditions. However, when the sintering time or temperature was increased, the samples did disintegrate easily and rapidly upon cooling. This fact also indicated that alumina did not stabilize the β-phase chemically.

As for the formation of aluminates, an interesting phenomenon was observed. The CA and C_3A phases were observed in all the sintering runs conducted in this research. The $C_{12}A_7$ phase was found both in the 1300°C and 1350°C series of runs. At 1200°C and 1250°C, it was found in noticeable amount only after several hours of sintering. At 1200°C, another phase, C_5A_3, was formed and increased with time. This fact led to a series of trials of synthesizing this phase from binary mixtures of $CaCO_3$-Al_2O_3. Unfortunately, it was not successful. No matter what kind of sintering temperature or time was tried, only $C_{12}A_7$, CA and C_3A were observed in noticeable amount, with $C_{12}A_7$ increasing with time and CA and C_3A decreasing with time after reaching a maximum value. According to Chemekova and Udalov (15), this C_5A_3 phase could only be synthesized from binary mixtures under an extreme reducing atmosphere.

Two versions of the phase diagram of the CaO-Al_2O_3 system are shown in Figs. 15 and 16 (52, 53). In both cases there are no stability regions for a C_5A_3 phase. In Fig. 15, the experiments were conducted in an ordinary atmosphere and the $C_{12}A_7$ phase was observed as a stable compound. However, it has been pointed out (70) that the $C_{12}A_7$ phase is not strictly anhydrous, which causes some doubt about the correctness of this phase diagram for not showing the H_2O. When the study was done in a moisture-free atmosphere, the phase diagram in

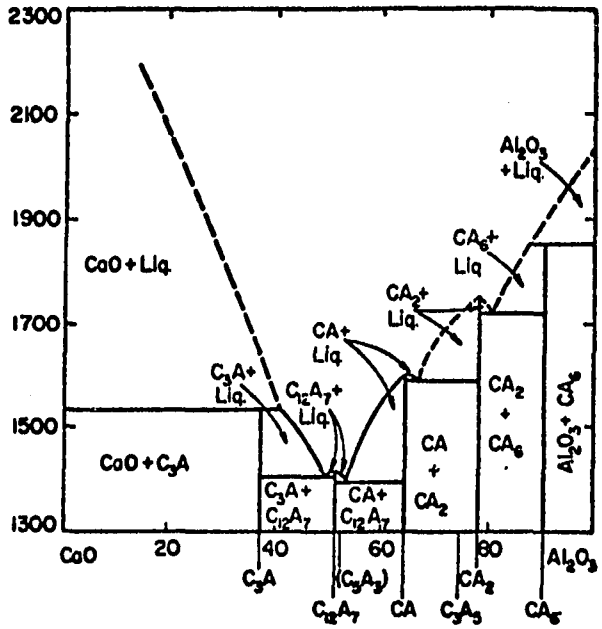

Fig. 15. Phase diagram of the $CaO-Al_2O_3$ system in ordinary atmosphere

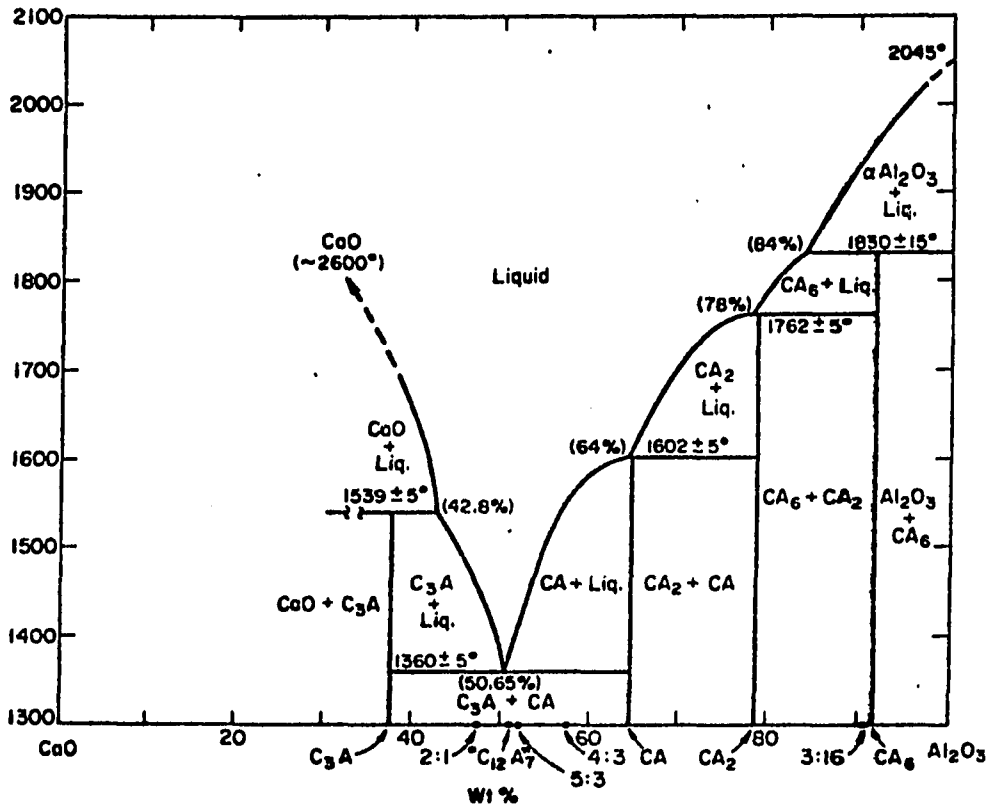

Fig. 16. Phase diagram of the $CaO-Al_2O_3$ system in a moisture-free atmosphere

Fig. 16 was obtained. Here, the $C_{12}A_7$ phase became an unstable compound also.

The reason for the formation of C_5A_3 in the ternary system at 1200°C is not known. The stability limits of C_5A_3 were never specified in the literature. It can only be guessed that the SiO_2 must play an important role in stabilizing the C_5A_3 while limiting the formation and growth of $C_{12}A_7$. From the facts that formation of C_5A_3 is more favorable under a reducing atmosphere and $C_{12}A_7$ needs excess oxygen (39) to be stabilized, it is possible that the SiO_2 or the silicate phase ties up the oxygen and thus slows the formation of $C_{12}A_7$ and promotes that of C_5A_3. However, when the temperature is higher, both the mobility of the oxygen ion within the particles and the influence of the oxygen in the atmosphere are higher and the C_5A_3 phase becomes unstable again. Another possibility is that the Si ion gets into the structure of C_5A_3 and stabilizes it temporarily. The real reason lying behind this phenomenon requires more careful study.

Scanning electron microscopy (SEM)

SEM is a powerful technique to characterize particles. It not only reveals the size and shape of particles but also the surface structures. A total of 8 SEM pictures are shown in Figs. 17-24.

The first two pictures (Figs. 17 and 18) are of pure SiO_2 gel and Al_2O_3. The original particle size of the SiO_2 gel was between 250μ and 74μ as given by the manufacturer. After 6 hours of grinding, it could be seen that its size had been greatly reduced. The particle size of alumina was much smaller than that of the SiO_2. The particle

Fig. 17. SEM micrograph of SiO_2 gel ground for 6 hours (500x)

Fig. 18. SEM micrograph of Al_2O_3 ground for 6 hours (500x)

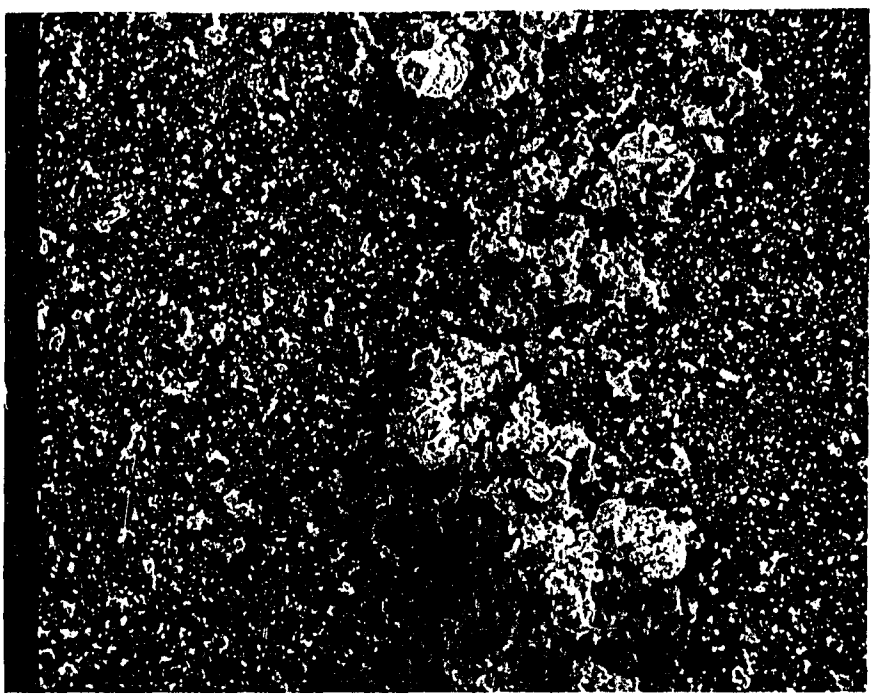

Fig. 19. SEM micrograph of the ternary mixture ground for 6 hours (1000x)

Fig. 20. A closer look at the above micrograph (3000x)

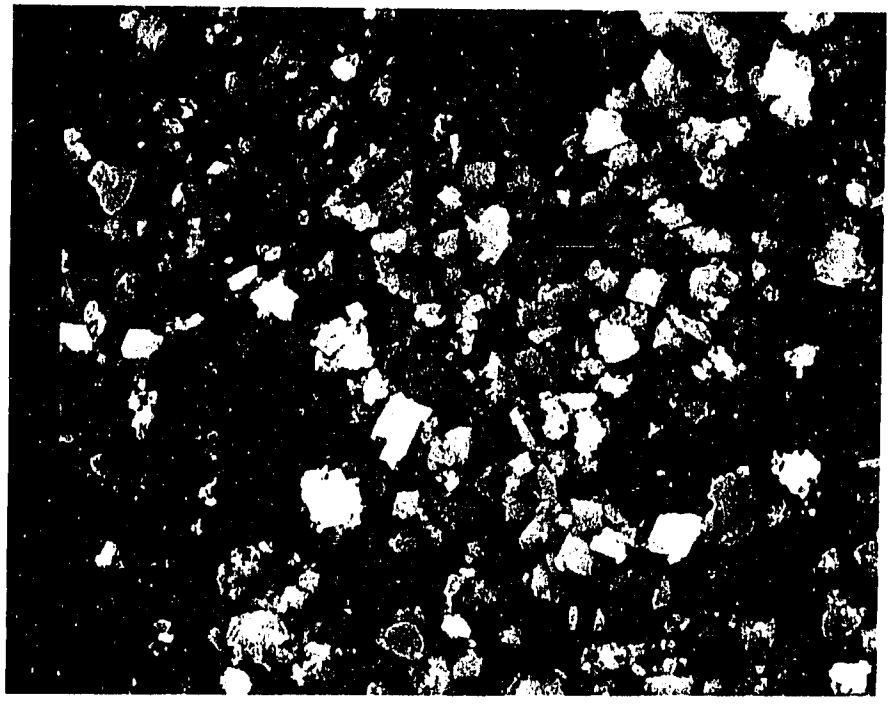

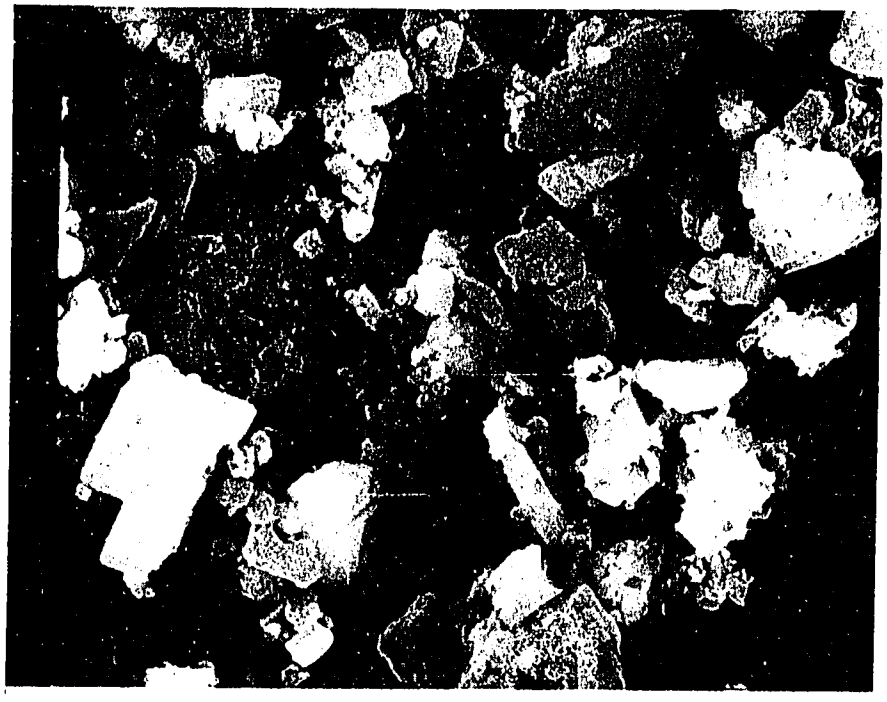

Fig. 21. SEM micrograph of the ternary powder sintered at 1250°C for 7 hours (2000x)

Fig. 22. A closer look at the above micrograph (6000x)

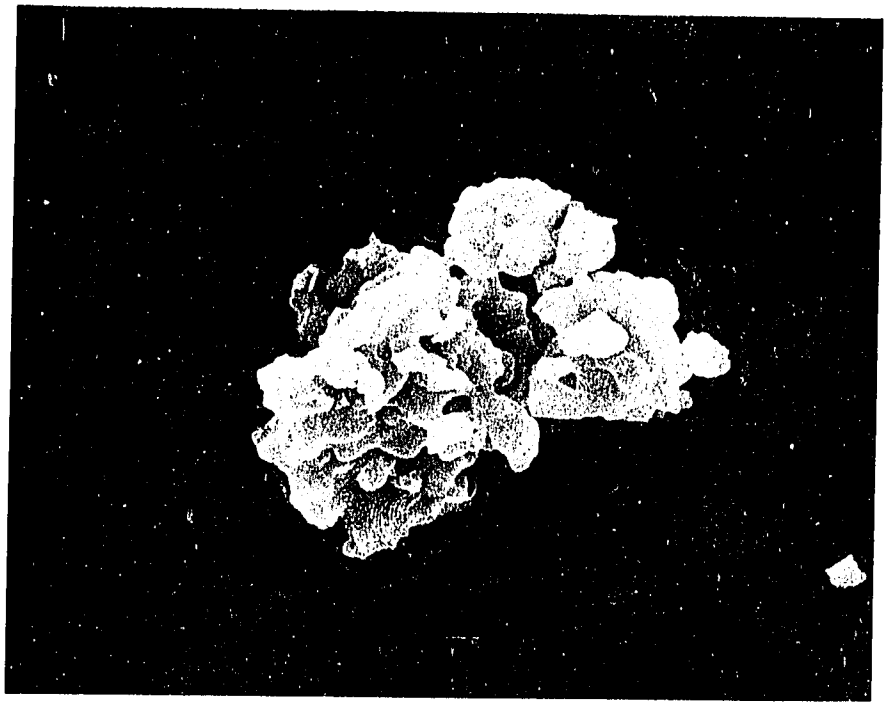

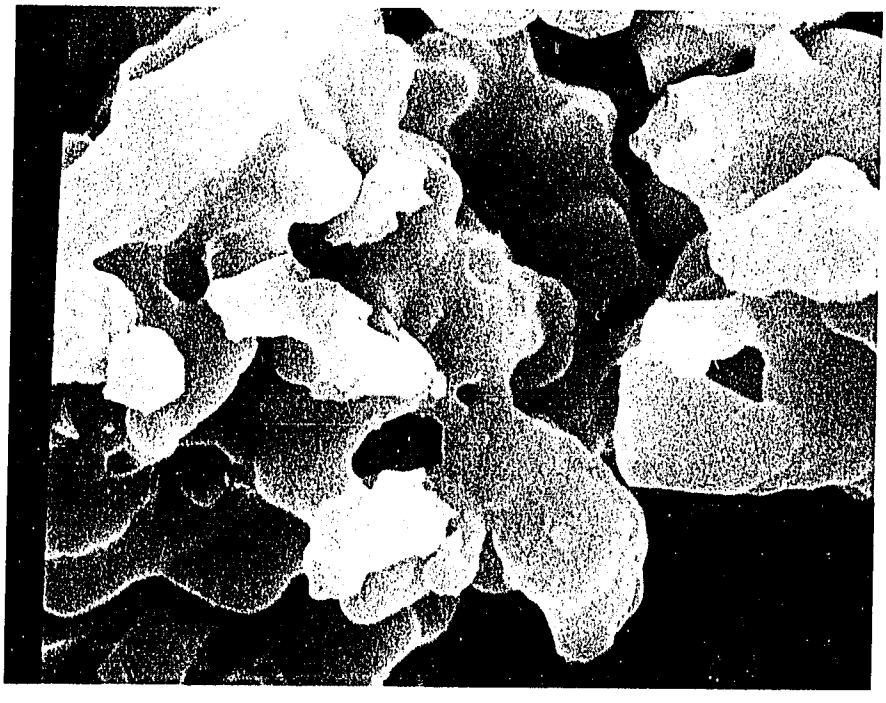

Fig. 23. SEM micrograph of the ternary sinter (1250°C, 7 hr) after being leached by 3% Na_2CO_3 solution (3000x)

Fig. 24. SEM micrograph of the ternary sinter (1250°C, 7 hr) after the maleic acid treatment (2000x)

size distribution of the Al_2O_3, as shown in Fig. 5, confirms that the grinding process also reduced its size. The large specific surface area of the Al_2O_3 was probably a direct result of its fineness. The next two pictures (Figs. 19 and 20) were of the starting ternary mixture in its loose powder form. Particles of different sizes and shapes were very well-mixed together.

The next four micrographs (Figs. 21-24) belong to a specific sinter, which was chosen as an example to illustrate the general features of the sinters. This special sinter had been heated at 1250°C for 7 hours. Pellets from this sintering run were very soft and crumbled easily with a little shake of the platinum boat. X-ray pattern of this sinter showed a small amount of γ-C_2S, while the majority was in the β-form. The aluminates formed at this stage were mainly CA and C_3A, along with a small amount of the $C_{12}A_7$ phase.

In Figs. 21 and 22, pictures of different magnifications of the sinter are shown. It can be easily seen that after this sintering step, the edges of particles were rounded and some particles were bound together through the interaction between them.

Micrographs of the sinter after it was leached using a 3% Na_2CO_3 solution and a maleic acid-methanol solution are shown in Figs. 23 and 24, respectively. The sodium carbonate solution removed most of the aluminates which constituted only about 22% of the total weight. When the sodium carbonate reacted with the aluminates, calcium carbonate was precipitated. In Fig. 23, the little square-shaped particles are probably calcium carbonate.

When the sinter was treated with maleic acid, the C_2S phase

dissolved away and left the aluminates in the residue. Actually, the maleic acid-methanol solution did not dissolve all the C_2S. There was always a little bit of C_2S left in the residue. Here, in Fig. 24, the many elongated particles consist of aluminates and were probably caused by many small aluminate particles sticking to the base material. This indicates that the aluminates and silicates coexist in many of the particles of the sinters.

Electron microprobe analysis (EMPA)

In the subsystem of C_2S-$C_{12}A_7$-CA (Fig. 4) where samples used in this work are located, the eutectic composition has a melting point of 1335°C. For all the runs made at 1200°C, 1250°C and 1300°C the appearance of the pellets did not change very much as the result of sintering. Evidently, the reactions occurring here were purely solid-solid reactions. However, when the sintering temperature was 1350°C, liquid formed in the pellets and as a result the pellets shrank considerably. When they were quenched in the air, disintegration of the pellets did not occur except for the run which lasted 4 hours. For the runs which lasted one or two hours, the pellets showed a small amount of disintegration after several days.

Those pellets which did not crumble were used in this EMPA work. Samples from other runs consisted mainly of fine particles which made the work much more difficult. Results obtained with these powders were not satisfactory because of the severe charging problem encountered in the analysis. Generally speaking, the data showed that every particle analyzed contained all three elements. They were rich in calcium and

silicon, calcium and aluminum or sometimes only in calcium. However, the other elements never failed to show up. This phenomenon was probably caused by the thorough mixing process and also the fineness of the alumina powder.

The results of EMPA of pellets from runs made at 1350°C for one and two hours are shown in Figs. 25-29. In Fig. 25, a scan was made at 2μ/step across an unreacted alumina powder. The direct output from EMPA was expressed in terms of weight percent of Ca, Al and Si elements. It was first converted into corresponding weight percentages of the oxides of these elements and then into mole fractions for each point along the scan.

It can be seen from this figure that the diameter of the unreacted alumina particle was about 16μ. Within this range of width, Si was not detected but Ca was found at low concentrations throughout the whole range. From this fact, it is clear that Ca ion is the diffusing cation in this system, which had been demonstrated many times before (23, 45, 55). However, in order to maintain the electrical neutrality, one of the following cases had to happen (45, 81):

1. counterdiffusion of another cation, Al^{+3} in the formation of aluminates;
2. diffusion of oxygen ions in the same direction as that of calcium ions;
3. diffusion of electrons and the transport of oxygen through the gaseous phase.

In their studies of reactions between CaO and Al_2O_3, Kohatsu and Brindley (45) found that the principal cation movement was made by Ca^{+2}

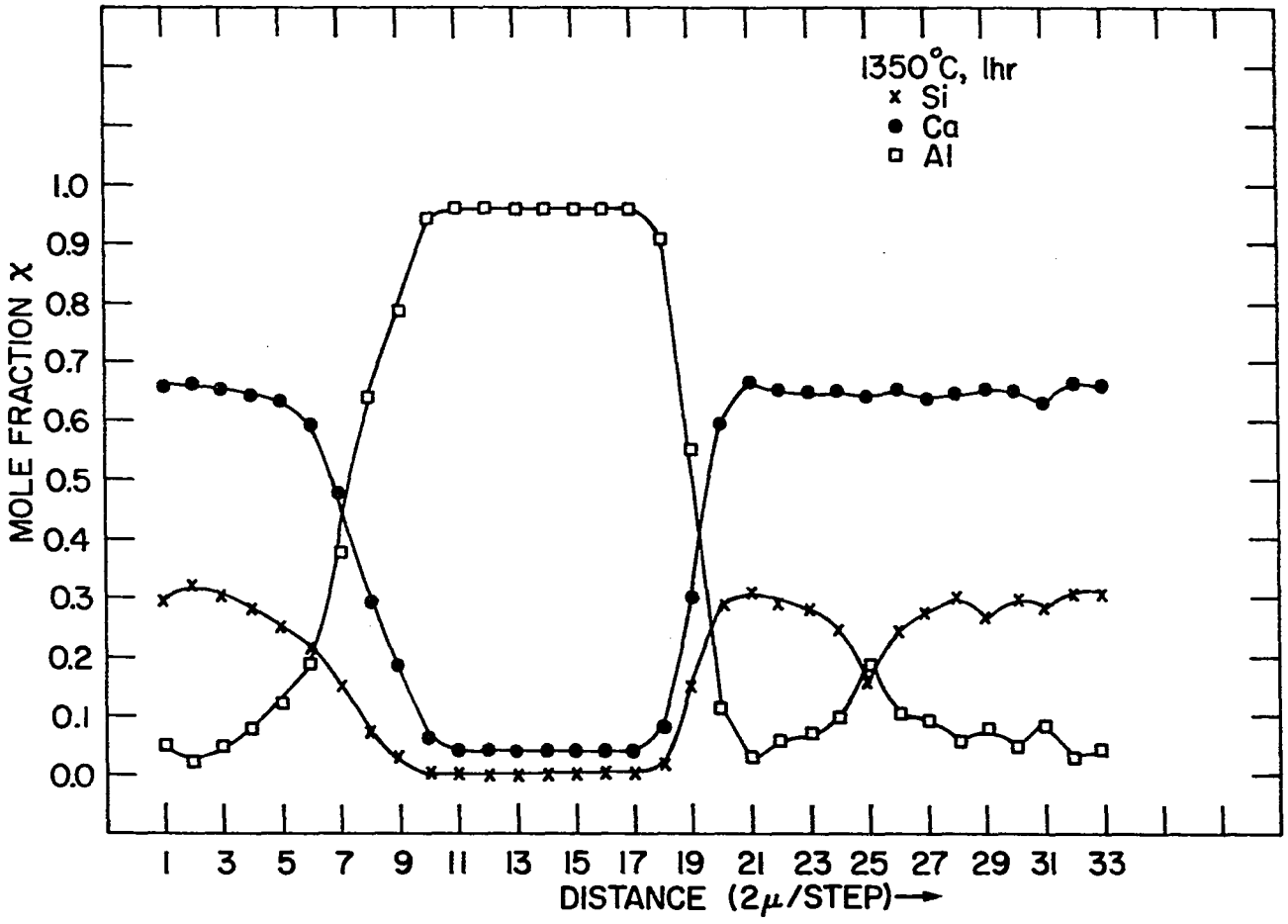

Fig. 25. Distribution of oxides across the $CaO-Al_2O_3-SiO_2$ pellet (sintered at 1350°C for 1 hr) as analyzed by EMPA

Fig. 26. Photomicrograph of a polished section of $CaO-Al_2O_3-SiO_2$ pellet sintered at 1350°C for 1 hr (940x)

Fig. 27. Energy dispersive X-ray analysis of calcium for Fig. 26. Except for the black area, the calcium is distributed evenly in the pellet (940x)

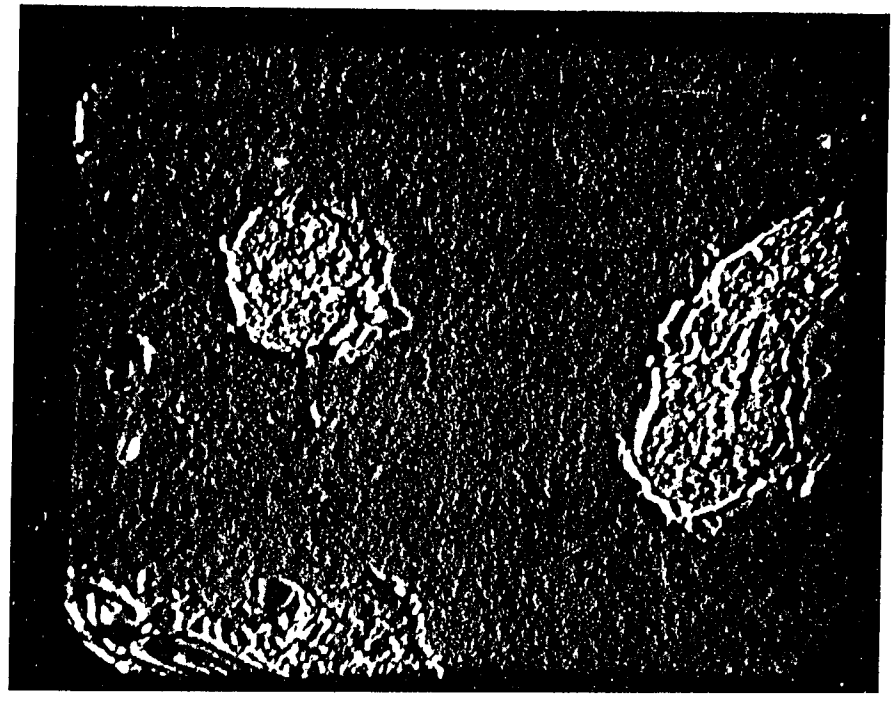

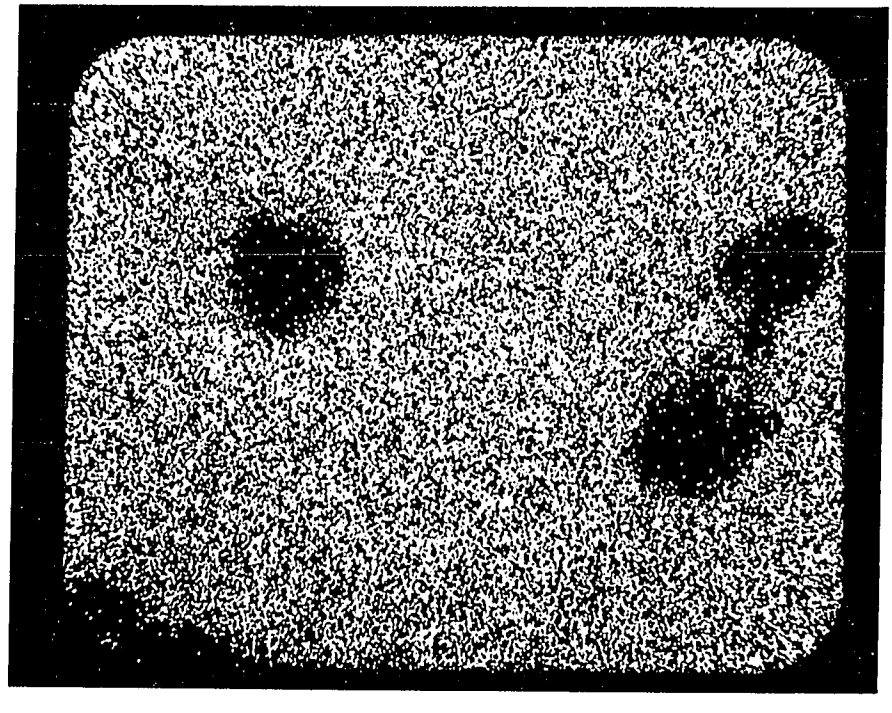

Fig. 28. Energy dispersive X-ray analysis of silicon for Fig. 26. Its distribution is not as uniform as that of calcium (940x)

Fig. 29. Energy dispersive X-ray analysis of aluminum for Fig. 26. There are three areas where only aluminum exists. This indicates unreacted alumina particles (940x)

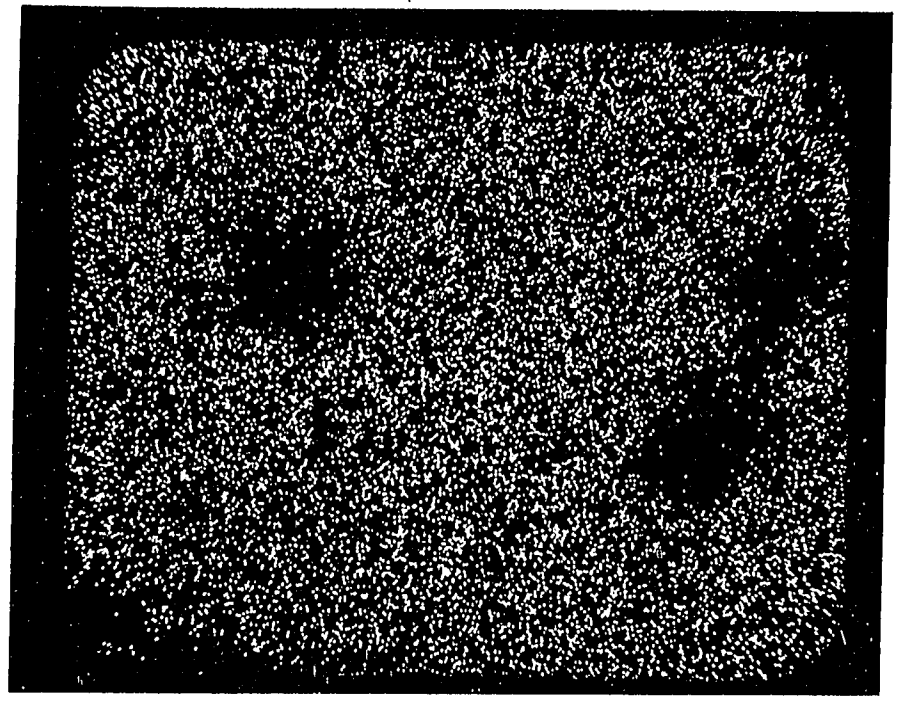

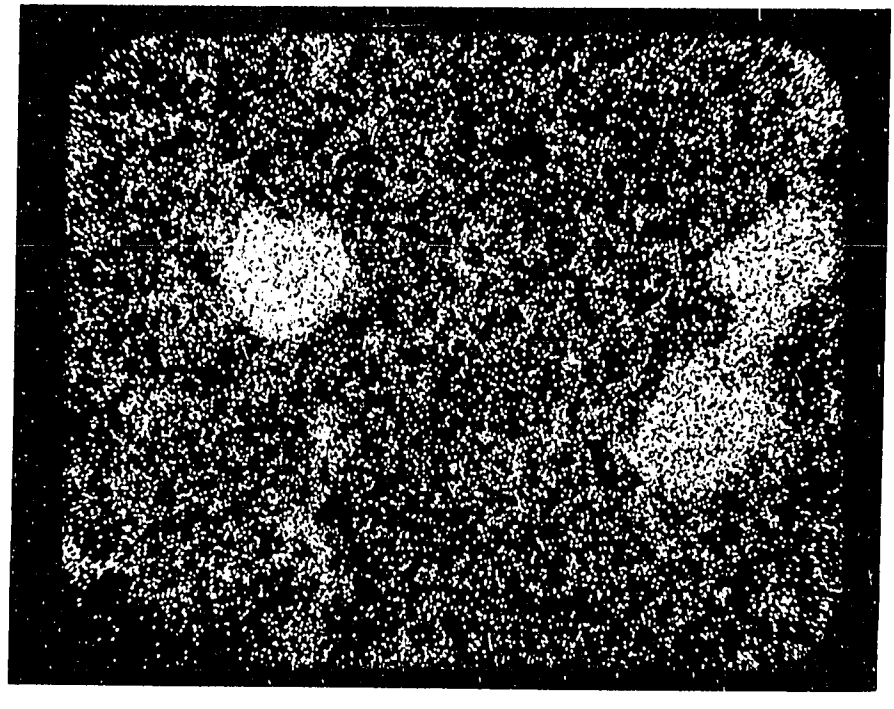

only. This would remove the possibility of the first case mentioned above. As to the other cases, there has never been any detailed study to decide which one was the real mechanism occurring in the reactions between CaO and Al_2O_3. In the author's viewpoint, the diffusion of oxygen ion is more likely to happen in this system. Nevertheless, the diffusion rate of Ca^{+2} would be much greater than any of these possibilities so that the rate-controlling step would depend on the diffusion of oxygen ion or the transport of oxygen gas.

The next four figures, Figs. 26-29, show corresponding photomicrographs of a polished section of a pellet from the 1350°C, 1 hr sintering test and the energy dispersive X-ray distribution of Ca, Si and Al across this section. It can be seen that there are still unreacted alumina particles remaining in the matrix produced when liquid formed in the system.

In Fig. 30, data from the analysis of pellets sintered at 1350°C for 2 hours are plotted on the phase diagram of the $CaO-Al_2O_3-SiO_2$ system. In this case, the scan was made across the whole pellet at 10μ/step. A total of 110 points were analyzed. All these points were generally distributed within the subsystem of $C_2S-C_{12}A_7-CA$. These points, scattered across a wide range of composition, indicate that the overall equilibrium of the pellet was still far away. If the pellets had been sintered longer, there would have been a narrower range of composition. In the ultimate, point analyses would give the same composition as that of the overall particle. However, judging from the difference between this pellet (1350°C, 2 hr) and the one

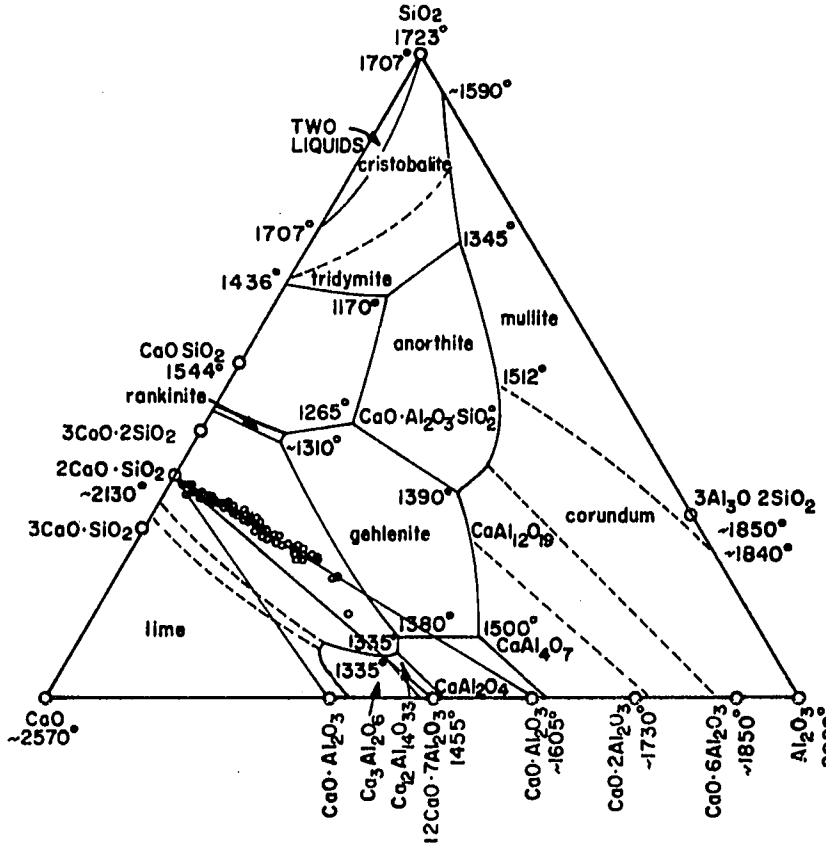

Fig. 30. Point analysis (as dots) by EMPA of polished section of a $CaO-Al_2O_3-SiO_2$ pellet sintered at 1350°C for 2 hours

discussed earlier (1350°C, 1 hr), it is apparent that there has been much progress toward equilibrium.

High-temperature X-ray diffraction analysis

Samples of starting components were first examined individually. At room temperature, $CaCO_3$ was found to be in the form of calcite, SiO_2 gel to be amorphous and Al_2O_3 to be poorly crystallized in its γ-form. Upon heating, calcium carbonate decomposed into calcium oxide, SiO_2 gel transformed slowly into cristobalite beginning at 1300°C, and Al_2O_3 changed into its α-form over the range of 1000°C-1200°C.

Next, the binary mixtures of calcium carbonate and silica gel (molar ratio 2:1) and calcium carbonate and alumina (molar ratio 12:7), along with the ternary mixture were tested on the high-temperature X-ray machine. In the mixture of $CaCO_3$ and SiO_2, dicalcium silicate ($2CaO \cdot SiO_2$) was the only compound detected. It increased with time and temperature. The identification of this compound and later other aluminates was done by obtaining high-temperature X-ray patterns of their pure compounds synthesized earlier. Generally speaking, the atomic structures would expand upon heating. The heating thus increased the d values somewhat and decreased the corresponding 2θ angles. The identification of the metastable C_5A_3 was accomplished using the room-temperature X-ray pattern and the realization of the temperature effect.

In the case of $CaCO_3$ and Al_2O_3, several types of aluminates were observed during the course of the heating. X-ray patterns obtained at 900°, 1000°, 1100°, and 1250°C are shown in Figs. 31 and 32. At 900°C,

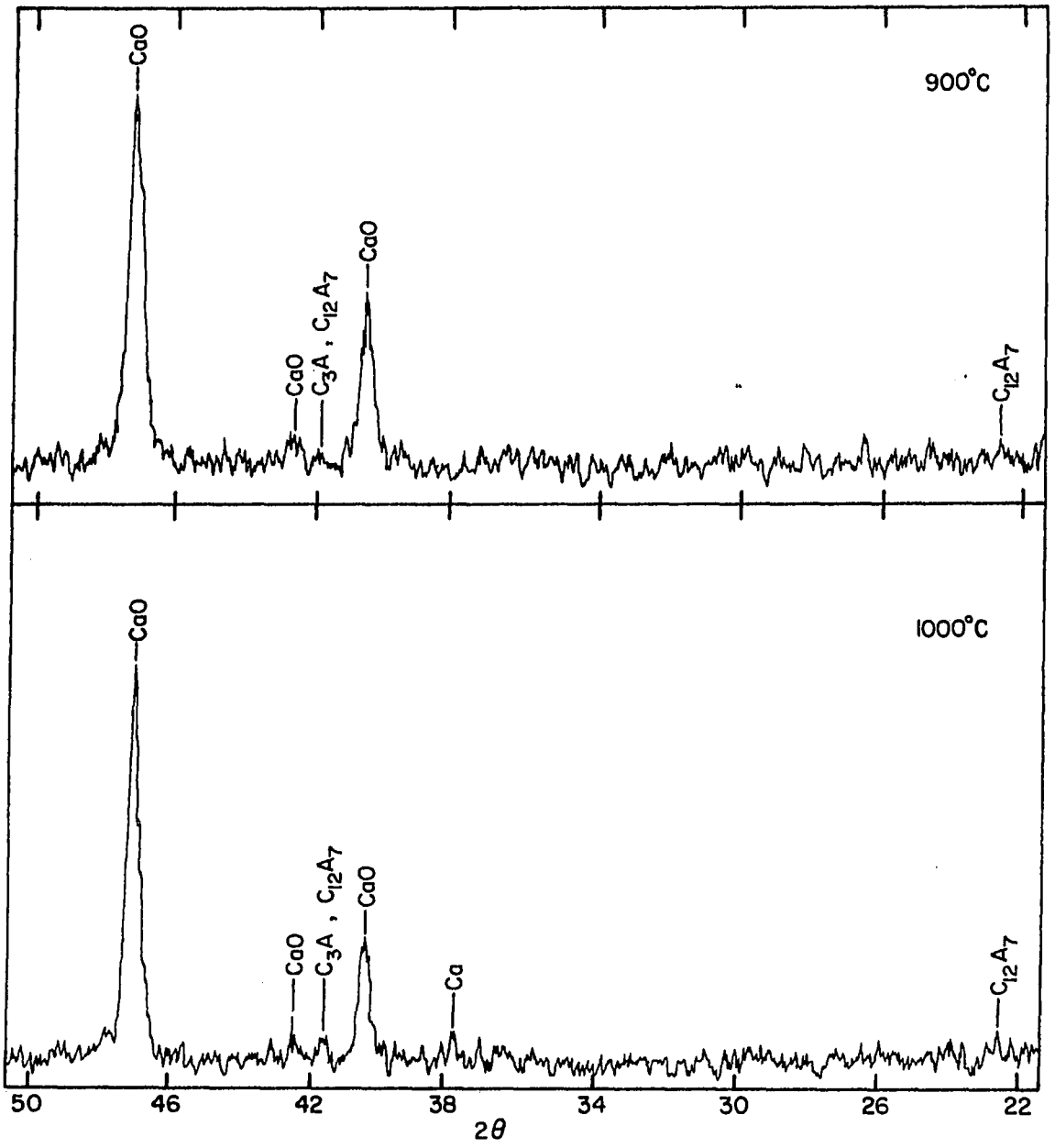

Fig. 31. High-temperature X-ray patterns of a mixture of $CaCO_3$ and Al_2O_3 (molar ratio 12:7) at 900°C and 1000°C

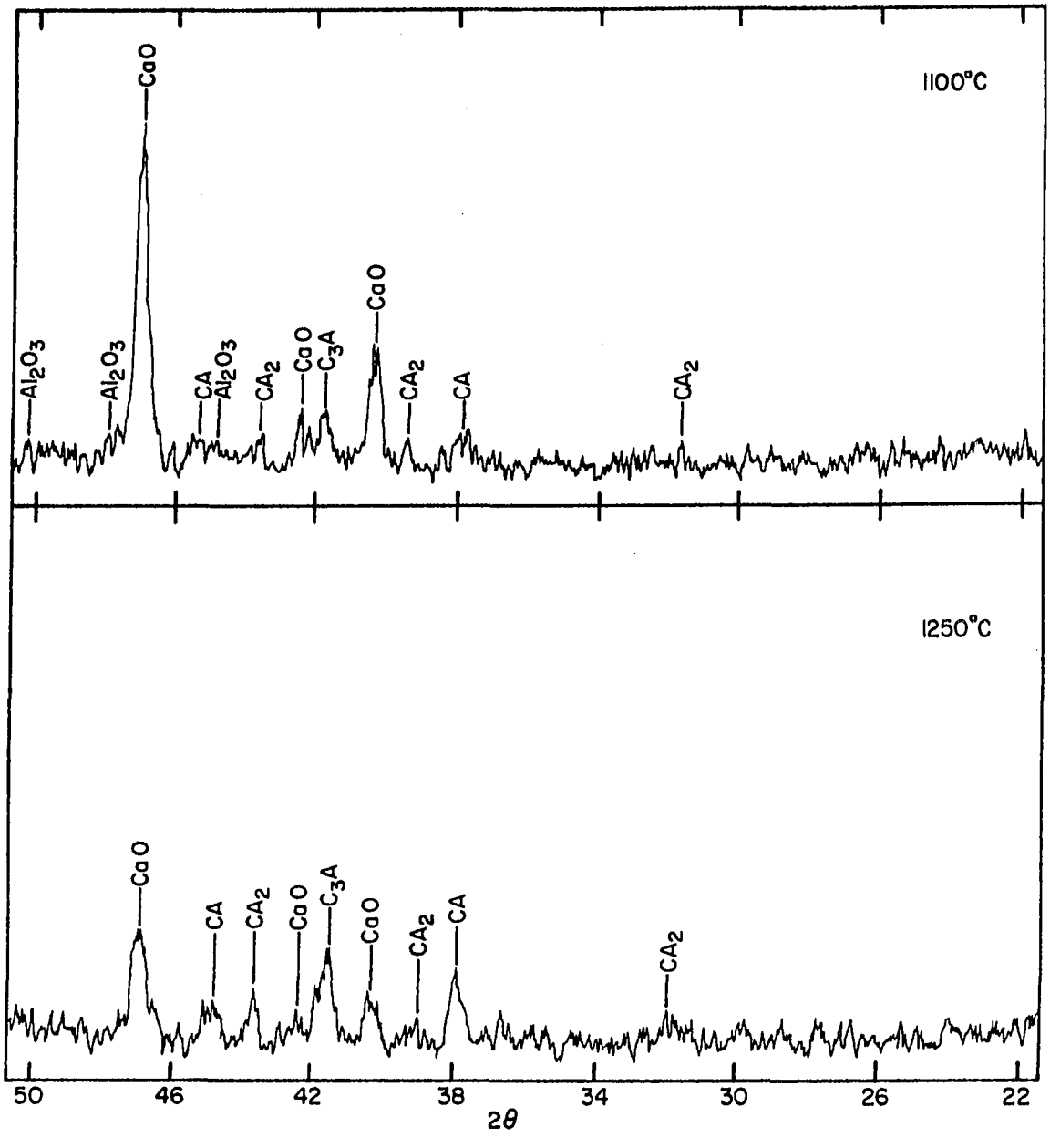

Fig. 32. High-temperature X-ray patterns of a mixture of $CaCO_3$ and Al_2O_3 (molar ratio 12:7) at 1100°C and 1250°C

it seems that small amounts of $C_{12}A_7$ are formed as shown in Fig. 31. However, the peaks did not grow with temperature or time. At 1000°C, it appears that $C_{12}A_7$ might still exist, but the formation of CA and C_3A is definite. As the temperature was further increased (Fig. 32), both CA and C_3A increased. At 1100°C, CA_2 was formed and persisted until the end of the experiment.

In discussing the results of the high-temperature X-ray diffraction analysis, one thing must be kept in mind, i.e., that the quantity of the sample used in each run was about 0.1 gm or less. The chances for the composition to deviate from that of the desired composition is thus greater than would be the case for samples of 1 gm or 5 gms.

Comparison of the decrease in CaO in mixtures of $CaCO_3$ and SiO_2 with that in mixtures of $CaCO_3$ and Al_2O_3 under the same conditions, showed that the reaction between CaO and SiO_2 probably proceeds at a faster rate than the reaction between CaO and Al_2O_3. This fact would definitely have some effect in the ternary system.

High-temperature X-ray patterns of the ternary mixture are shown in Figs. 33 and 34. At 900°C, only C_2S and unreacted CaO can be clearly identified. No aluminates were visible at this stage. This was probably caused by too small amounts being formed in the system. As the temperature increased to 1100°C, CA and C_3A began to appear and finally, at 1250°C, C_5A_3 was also observed. The $C_{12}A_7$ phase was not seen through the entire experiment.

The finding of C_5A_3 at 1250°C is not necessarily in contradiction to what was reported earlier. There are two possibilities to explain this phenomenon. The first, and very likely the true reason, is the

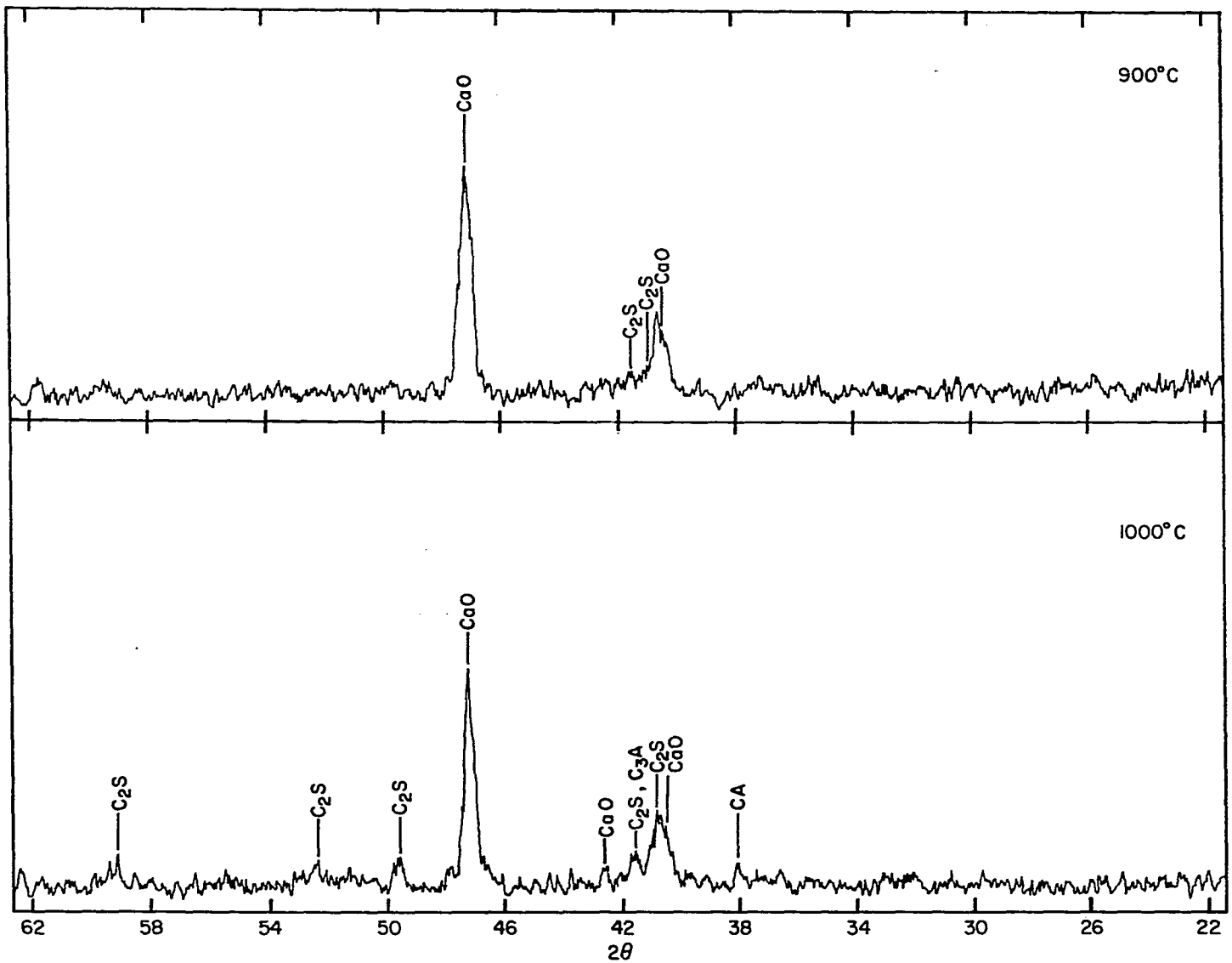

Fig. 33. X-ray patterns of the ternary mixture of $CaO-Al_2O_3-SiO_2$ at 900°C and 1000°C

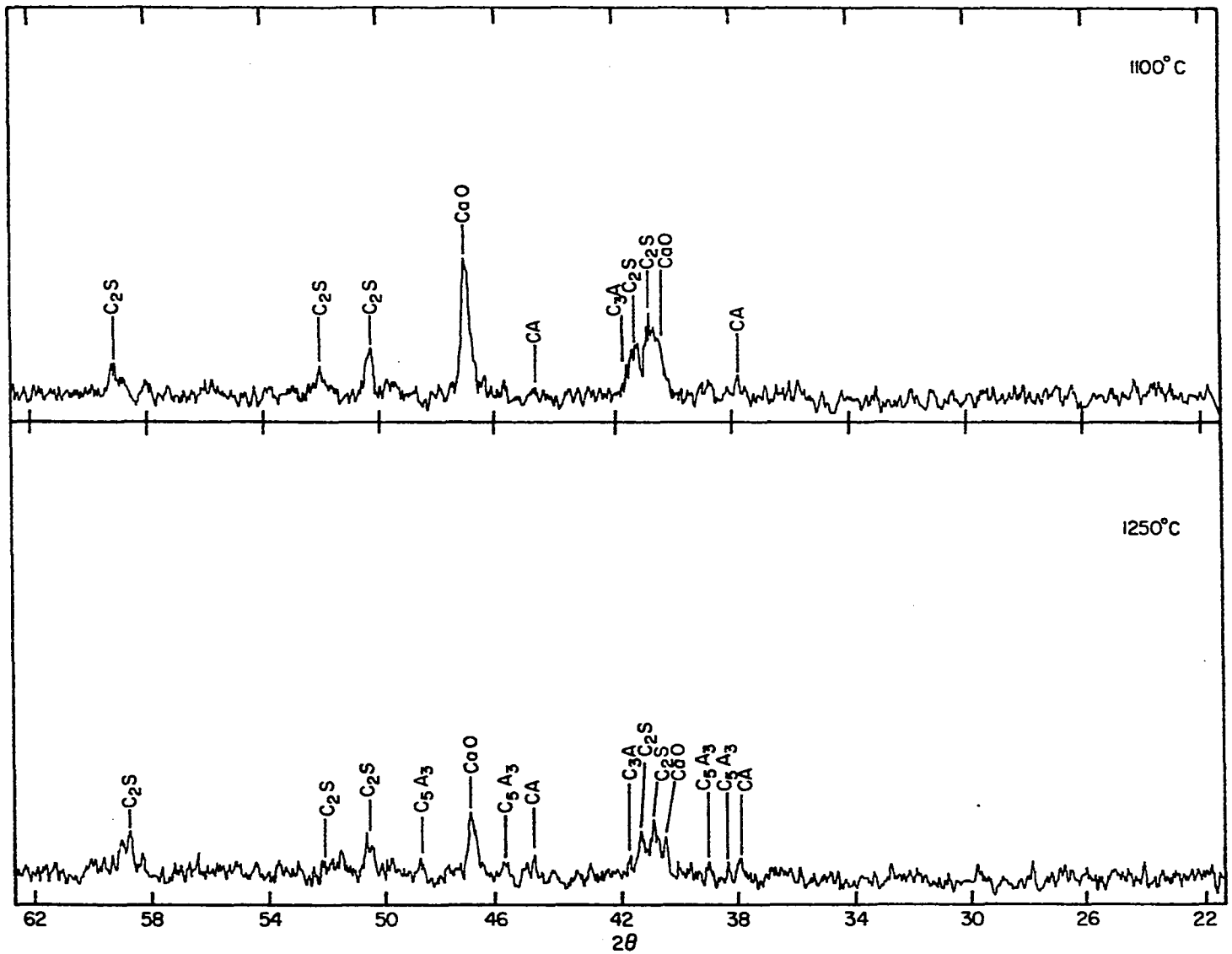

Fig. 34. X-ray patterns of the ternary mixture of $CaO-Al_2O_3-SiO_2$ at 1100°C and 1250°C

fact that the temperature of the sample at the top of the holder was below the desired 1250°C. A thermal gradient of 15°C across the depth of the sample was not uncommon. A second possibility is that a small variation in composition of the batch helped to stabilize the C_5A_3 phase up to 1250°C.

Overall, the components in this ternary system behaved like two binary systems, $CaO-Al_2O_3$ and $CaO-SiO_2$, when the sintering temperature was below the eutectic temperature (1335°C). No ternary compounds were observed in the product from any of the runs made below this temperature.

Differential thermal analysis (DTA)

Like the high-temperature X-ray diffraction analysis, DTA was carried out first on the individual components, then on the binary mixtures and finally on the ternary mixture. The amount of the sample used here was also small, only in the range of 20-30 mg.

When $CaCO_3$ was heated at 10°C/min, the TG curve began to deviate at about 644°C and it flattened out at 844°C. From the DTA curve, the endothermic peak corresponding to the decomposition of $CaCO_3$ peaked at 824°C, which meant at this temperature the decomposition rate was at its maximum. When pellets were made out of this component, the necessity for CO_2 gas to diffuse out slowed down the decomposition process. To compensate for this, the pellets were held at 850°C for 2 hours while the decomposition took place.

For Al_2O_3 powders, two endothermic peaks were observed at 96°C and 520°C, respectively. Corresponding weight losses were also observed.

This indicated that the endothermic peaks were associated with the desorption of foreign gases from the surface of the powder. Beyond 600°C, there was no change in the TG curve. However, at 1220°C, there was an exothermic peak which probably corresponded to the transformation of γ-Al_2O_3 into α-Al_2O_3.

In the case of SiO_2 gel, a big endothermic peak and corresponding weight loss were observed at about 60°C. After that there was not much change in either curve, except that between 1250°C and 1360°C, there was a small, broad endothermic peak. This was caused by the crystallization of this amorphous material into cristobalite form.

The DTA and TG curves of the binary and ternary mixtures are shown in Figs. 35, 36 and 37. In all three figures, it is clear that the decomposition of $CaCO_3$ was not changed by the addition of SiO_2 and/or Al_2O_3. After the $CaCO_3$ decomposition, however, the binary mixture of $CaCO_3$ and SiO_2 (molar ratio 2:1) and that of $CaCO_3$ and Al_2O_3 (molar ratio 12:7) behave quite differently. In the case of $CaCO_3$-SiO_2 (Fig. 35), two distinct exothermic peaks are seen at 844°C and 900°C. The first one occurs right after the completion of the decomposition of $CaCO_3$. It probably is caused by the formation of a C_2S phase on the surface of the SiO_2 particles. The second peak might correspond to the phase transformation of the C_2S already formed. Other changes of the DTA curve after this temperature are probably caused by another phase transformation of the C_2S or the crystallization of unreacted SiO_2 into cristobalite.

In the mixtures of $CaCO_3$ and Al_2O_3 (Fig. 36), the DTA curve did not produce sharp peaks after the decomposition of $CaCO_3$. It simply

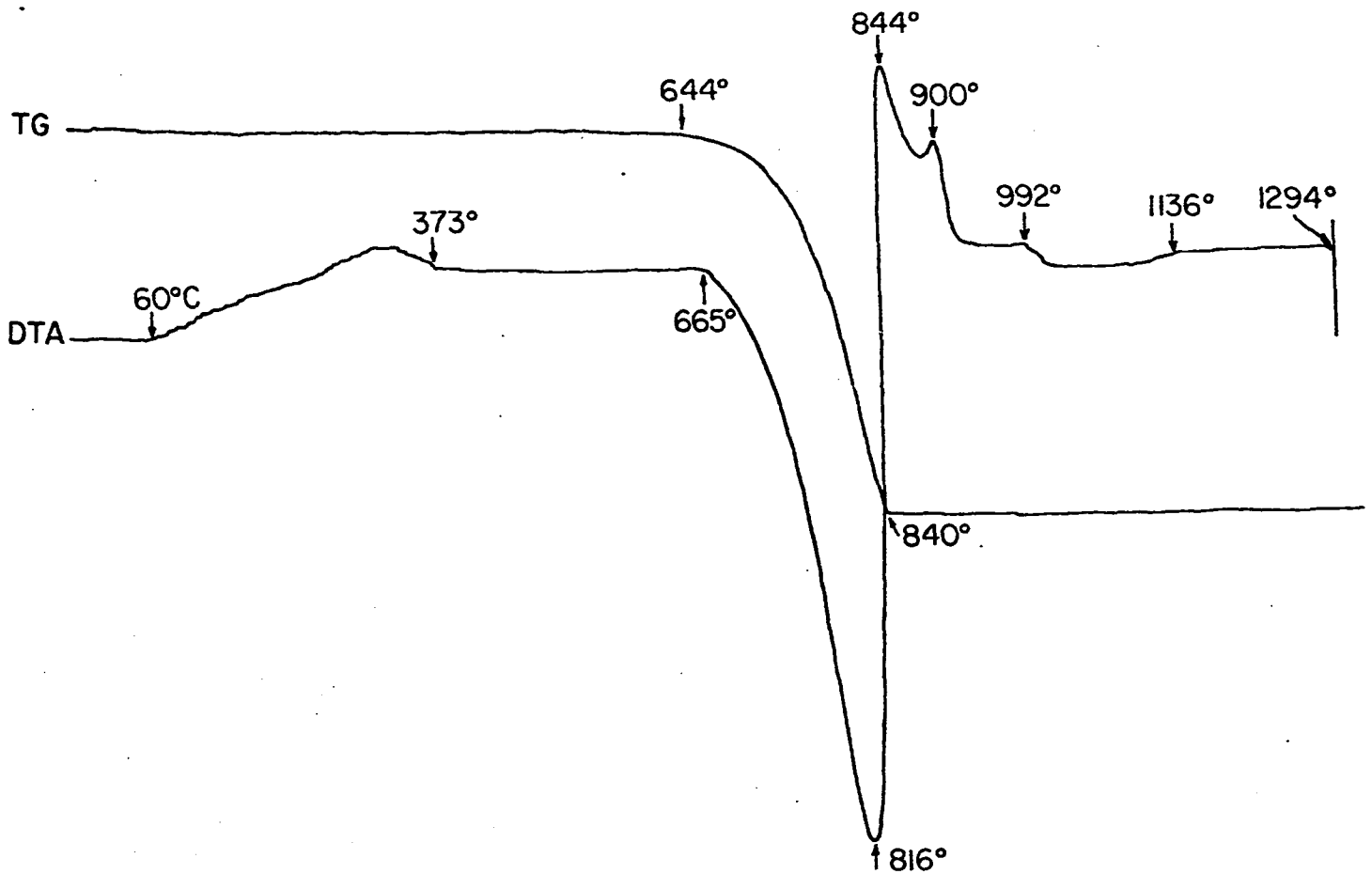

Fig. 35. DTA and TG curves for a binary mixture of $CaCO_3$ and SiO_2 gel. Heating rate = 10°C/min, sample amount = 25.4 mg, DTA range = 25 μV

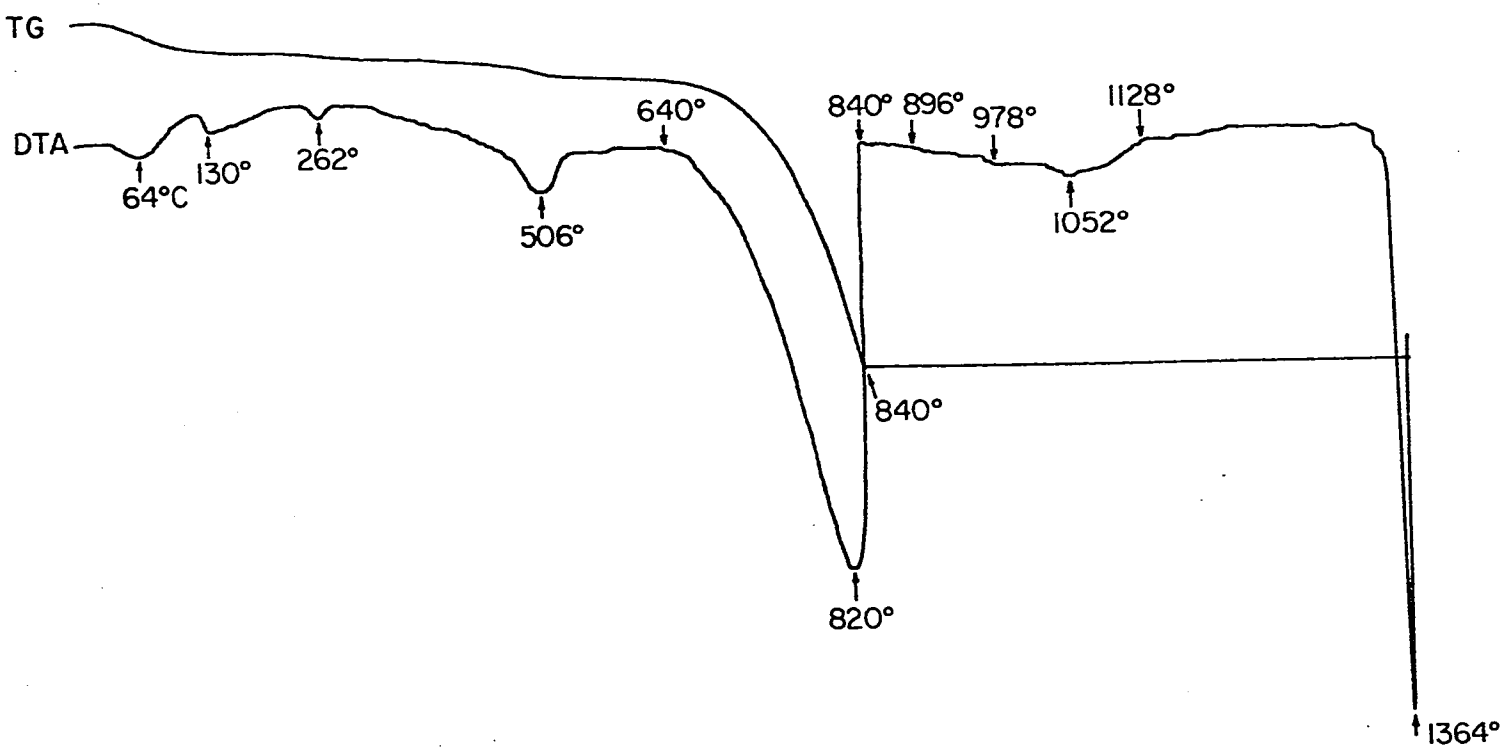

Fig. 36.. DTA and TG curves for a binary mixture of $CaCO_3$ and Al_2O_3. Heating rate = 10°C/min, sample amount = 26.2 mg, DTA range = 25 μV

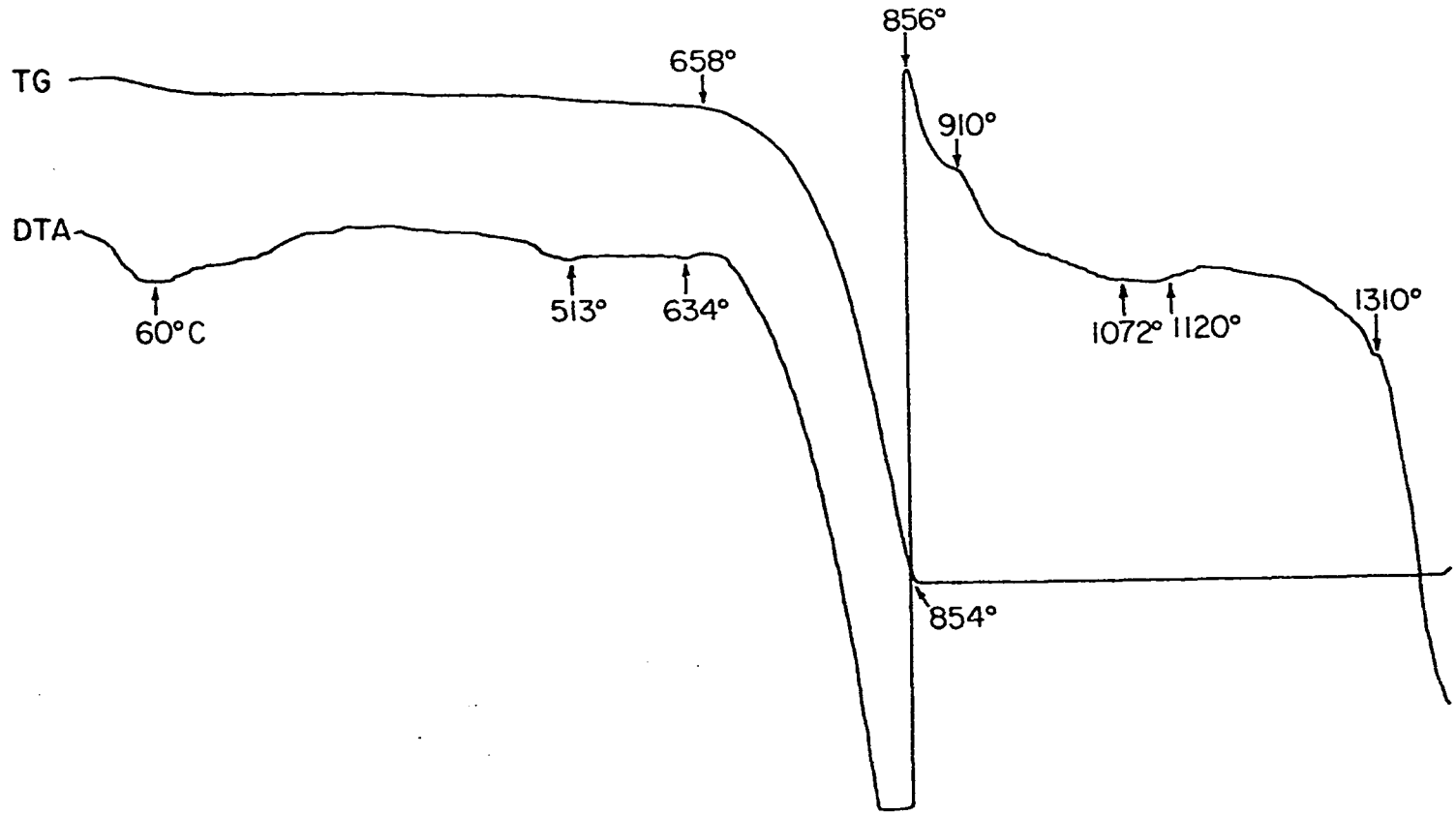

Fig. 37. DTA and TG curves for the ternary mixture of $CaCO_3$, Al_2O_3 and SiO_2 gel. Heating rate = 10°C/min, sample weight = 34.5 mg, DTA range = 25 μV

drifted gradually downward until about 1052°C, then rose back to 1128°C. This seems to suggest that the reaction between these two components only occurs on an atomic scale, i.e. the reaction heat is too small to be detected by this equipment. It also means that diffusion was important throughout this region of temperature change. At 1364°C, a sharp endothermic peak appears, indicating melting. This temperature corresponds very well to that in the phase diagram of $CaO-Al_2O_3$ shown in Fig. 16.

When the ternary mixture was heated (Fig. 37), the two exothermic peaks characteristic of the $CaCO_3-SiO_2$ binary mixture were observed. This again demonstrates indirectly that the components are actually reacting like two binary systems. At 1310°C, the DTA curve begins to deviate downward (or endothermically) sharply, suggesting that eutectic liquid is being formed.

Based on work reported thus far, a few conclusions can be drawn about the reactions that occur during the sintering of the ternary mixture. First, the components of the mixture behave like two binary systems, $CaO-Al_2O_3$ and $CaO-SiO_2$, below the eutectic point (1335°C). The reactions proceed strictly in solid state through the diffusion of Ca ion along with the migration of either oxygen ion or electrons and oxygen gas. Only one compound, C_2S, is formed between CaO and SiO_2, while several aluminates, C_3A, $C_{12}A_7$, C_5A_3, CA and CA_2, are observed over the temperature range studied.

Secondly, the reaction rate between CaO and SiO_2 is faster than that between CaO and Al_2O_3. Since C_2S is capable of dissolving some CaO into its structure, it is necessary to add more $CaCO_3$ to compensate for the amount thus lost and unavailable for reaction with Al_2O_3.

Finally, the reaction between CaO and Al_2O_3 is carried out through the formation of a sequence of compounds. This is caused by the preferred diffusion of Ca ion. The first compound formed between CaO and Al_2O_3 is very likely $C_{12}A_7$ but the amount present does not grow to any appreciable extent because of the unfavorable atmosphere. Then CA is formed as the calcium ion continues to diffuse into alumina. Then at some point, such as when the whole alumina particle has converted into CA, the C_3A phase begins to form. When the temperature is above 1100°C and there is still unreacted alumina, the CA_2 phase will form. Finally, when both the alumina and calcium oxide are used up, the $C_{12}A_7$ or C_5A_3 will grow at the expense of CA and C_3A.

Results of Quantitative Analysis of the Sinters

Samples obtained from the sintering runs were first leached by a maleic acid-methanol solution, and then analyzed quantitatively by both chemical and X-ray diffraction analysis. The quantities of the residues after maleic acid treatment are shown in Table 6. The overall composition of the ternary mixture by weight was as follows: CaO: 61.98%, SiO_2: 26.67% and Al_2O_3: 11.53%. Ideally, there would be about 76.51% of C_2S in the final sinter if all the SiO_2 had been converted into C_2S, and about 23.49% of the sinter would remain in the residue. Evidently, this was not the case in the actual sinter. This results primarily from incomplete reactions during sintering and also from the fact that the C_2S phase does not dissolve completely in the maleic acid-methanol solution as noted when the

Table 6. Residues of the sinters after the maleic acid treatment (in wt % of the original sample)[a]

Sintering temperature (°C)	Sintering time (hr)						
	0.2	0.5	1.0	2.0	4.0	7.0	10.0
1200	33.1	30.9	30.1	29.2	29.1	28.8	28.6
1250	34.6	30.4	30.3	29.8	27.8	27.7	27.2
1300	31.7	29.6	28.0	27.2	26.6	25.3	—
LR[b]	26.5	—	—	—	—	—	—

[a]All numbers reported here were averages of at least five tests.

[b]LR run was made at 1400°C for 6 hours.

procedure was discussed earlier. When pure γ-C_2S or β-C_2S was used, the residues weighed 5.4% based on seven tests.

The sintering run marked as LR was made at 1400°C for 6 hours and also with a very slow cooling rate: 1°C/min. The purpose of this run was to try to get the mixture to reach equilibrium. Since a liquid phase is formed at 1400°C, a slow cooling rate was used to obtain equilibrium crystallization.

Similar maleic acid treatments were also performed on pure CA, $C_{12}A_7$ and C_3A compounds. Results showed only negligible solubility (less than 1% by weight). This amount of dissolution was probably the result of free CaO in these compounds.

Chemical analysis

Results of chemical analysis on the residues from the maleic acid treatment are shown in Table 7. This set of data along with free CaO contents (Table 5) and weight percentages of the residues (Table 6) can be used to check the alumina contents and the molar ratio of CaO to

Table 7. Chemical analysis of the residues from the maleic acid treatment (wt %)

Runs[a]	CaO	SiO_2	Al_2O_3
1	41.49	23.56	34.95
2	46.25	16.80	36.95
3	48.39	13.84	37.77
4	52.51	8.18	39.30
5	52.69	6.41	40.90
6	52.52	5.76	41.85
7	52.59	4.92	42.49
8	41.64	24.62	33.73
9	47.70	14.16	38.14
10	50.49	10.45	39.06
11	50.84	8.19	40.97
12	51.14	5.38	43.49
13	49.92	5.91	44.16
14	50.23	4.94	44.83
15	51.57	12.28	36.15
16	52.20	8.70	39.10
17	53.53	5.90	40.57
18	53.19	4.90	41.91
19	51.91	5.27	42.82
LR	50.70	6.36	42.93

[a]Runs 1-7 were sintered at 1200°C, with increasing time; runs 8-14 at 1250°C; runs 15-19 at 1300°C. Run LR was made at 1400°C for 6 hours.

SiO_2 in the maleic acid-methanol solution. To convert the Al_2O_3 contents in the residues into those of the original sinters, we have to multiply the weight percent of Al_2O_3 from Table 7 with the corresponding weight percentages in Table 6. For example, for Run 1 (1200°C, 0.2 hr), the weight percentage of the residue is 33.1%, while the Al_2O_3 in the residue is 34.95%, so the Al_2O_3 content in the original sinter is 33.1% x 0.3495 = 11.57%. The average of the alumina content in the original sinter of the 20 runs in Table 7 is 11.68%, which is within

reasonable range of the number 11.53% reported earlier. This fact also suggests that none of the alumina is lost during the maleic acid treatment.

If we deduct the free CaO content and also the CaO in the residue from the total content of CaO in the sinter, we then obtain the amount of CaO which goes into the maleic acid-methanol solution. A similar calculation can be carried out for SiO_2. We then can calculate the molar ratio of CaO/SiO_2 in the solution. The results are reported in Table 8.

Table 8. Molar ratio of CaO/SiO_2 in the C_2S phase which dissolves in the maleic acid-methanol solution

Runs	Molar ratio CaO/SiO_2
1-7	2.01, 2.04, 2.09, 1.98, 1.99, 2.00, 1.98
8-14	2.09, 2.03, 2.02, 2.02, 2.03, 2.05, 2.04
15-19, LR	2.07, 2.06, 2.01, 2.00, 2.04, 2.08
Total average = 2.03	

It thus appears that the molar ratio of CaO/SiO_2 is not exactly 2.00, but rather 2.03. This means that a small amount of CaO can dissolve into the structure of the dicalcium orthosilicate. This is probably due to the fact that the reaction between CaO and SiO_2 is faster than that between CaO and Al_2O_3. It also suggests that a small excess of $CaCO_3$ is needed when samples are prepared for the lime sinter process.

Quantitative X-ray diffraction analysis

This quantitative work was performed only on the residues from the maleic acid treatment. The intensity ratio for the strongest peak for each pure aluminate (CA, $C_{12}A_7$ and C_3A) to that of KBr are shown in Table 9. These ratios were the basis for all the X-ray work for the determination of quantities of CA, $C_{12}A_7$ and C_3A in this portion of the research.

Table 9. Intensity ratios of the strongest peaks for three aluminates to the d = 2.392 peak of KBr

Intensity ratio[a]	CA d = 2.97	$C_{12}A_7$ d = 4.89	C_3A d = 2.70
I/I_{KBr}	0.8208	0.8531	1.568

[a]All numbers reported in the quantitative X-ray analysis are averages of ten measurements.

Standards consisting of mixtures of known composition of these three compounds and also of pure dicalcium silicate were then measured by the procedures described earlier. The results compared very well with the known compositions. Since the d = 2.97 peak of CA and d = 2.70 peak of C_3A are influenced by the presence of $C_{12}A_7$, calibration work was necessary to obtain accurate results. Known proportions of CA and $C_{12}A_7$ were prepared and intensity ratios of their respective peaks were determined. The measured values for the CA peak were then compared to the would-be values calculated from the measurement of 100% pure CA. The increases in intensity ratios shown in Table 10 and Fig. 10 are purely due to the influence from $C_{12}A_7$.

Table 10. Calibration of d = 2.97 peak of CA under the influence of $C_{12}A_7$

Added wt % of $C_{12}A_7$[a]	30	50	66.7	75	80	90
$\frac{I_{CA}}{I_{KBr}}$	0.2539	0.4237	0.2903	0.2214	0.1794	0.09288
$\Delta(\frac{I_{CA}}{I_{KBr}})$	0.0077	0.0133	0.0167	0.0162	0.0152	0.0108
$\frac{I_{C_{12}A_7}}{I_{KBr}}$	0.2640	n.d.[b]	0.5817	0.6570	0.6863	0.7776
Measured wt % of $C_{12}A_7$	30.9	n.d.	68.2	77.0	80.5	91.1

[a]The rest of the sample was CA, except in the first case where in addition to 30% of $C_{12}A_7$, 40% of C_3A was added.

[b]Not determined.

For the compound C_3A, the situation was not so fortuitous. The characteristic peak at d = 2.70 for C_3A obtained from sintering runs actually shifted to about d = 2.69, which made the calibration work based on pure synthesized C_3A unreliable since the d = 2.68 peak of $C_{12}A_7$ would be closer to the characteristic peak of C_3A in the sinters than in pure mixtures. To cope with this situation, the following empirical procedure was used to evaluate the absolute intensity of C_3A peak. First, the routine counter readout and diffraction strip chart for the discussed peak and its backgrounds were obtained. Next, the C_3A peak on the strip chart was separated empirically from that for

$C_{12}A_7$. Then the area under the real C_3A peak was compared to that under the composite C_3A peak by counting the number of small squares on the chart. Finally, the real intensity of the C_3A peak was calculated from the actual measurement and the data counted from the chart. From the results reported later, it seemed that this small shift in the C_3A peak did not have a significant effect on the resulting measurements.

The results of measurements of the quantities of CA, C_3A and $C_{12}A_7$ are reported in Table 11. The weight percentages of each of these compounds in the residues were first obtained from the quantitative X-ray work. They were then converted to weight percentages in the sinters by simply multiplying them by their respective numbers from Table 6. The results are shown in Figs. 38-40.

Table 11. Conversions of aluminates in the sinters for different runs

Sintering time (hr)	Sintering temperature (°C)							
	1200		1250			1300		
	CA	C_3A	CA	C_3A	$C_{12}A_7$	CA	C_3A	$C_{12}A_7$
0.2	0.27	0.096	0.30	0.156	0	0.324	0.205	0.269
0.5	0.331	0.189	0.423	0.239	0	0.369	0.305	0.275
1.0	0.398	0.268	0.527	0.336	0	0.325	0.218	0.398
2.0	0.467	0.370	0.56	0.408	0	0.270	0.150	0.562
4.0	0.442	0.406	0.57	0.372	0.053	0.220	0.106	0.682
7.0	0.400	0.360	0.607	0.320	0.088	0.18	0.066	0.754
10.0	0.358	0.309	0.636	0.240	0.118	—	—	—

The results can be summarized as follows. At 1200°C, both CA and C_3A increased with time to maxima and then decreased slowly. The C_5A_3 could also be seen at this temperature beginning with the 0.5 hr run.

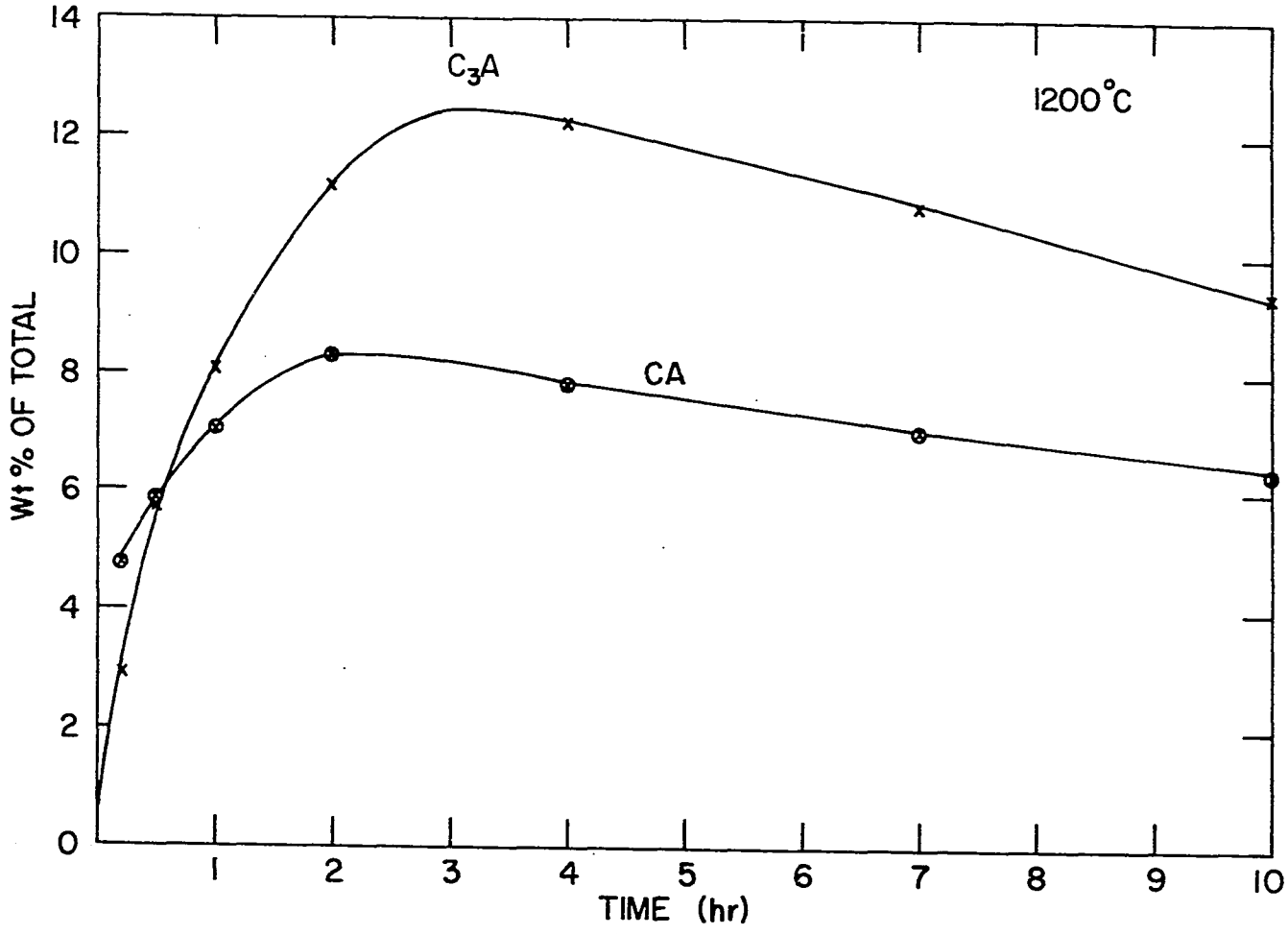

Fig. 38. Formation of CA and C_3A at 1200°C. The C_5A_3 phase also formed at this temperature

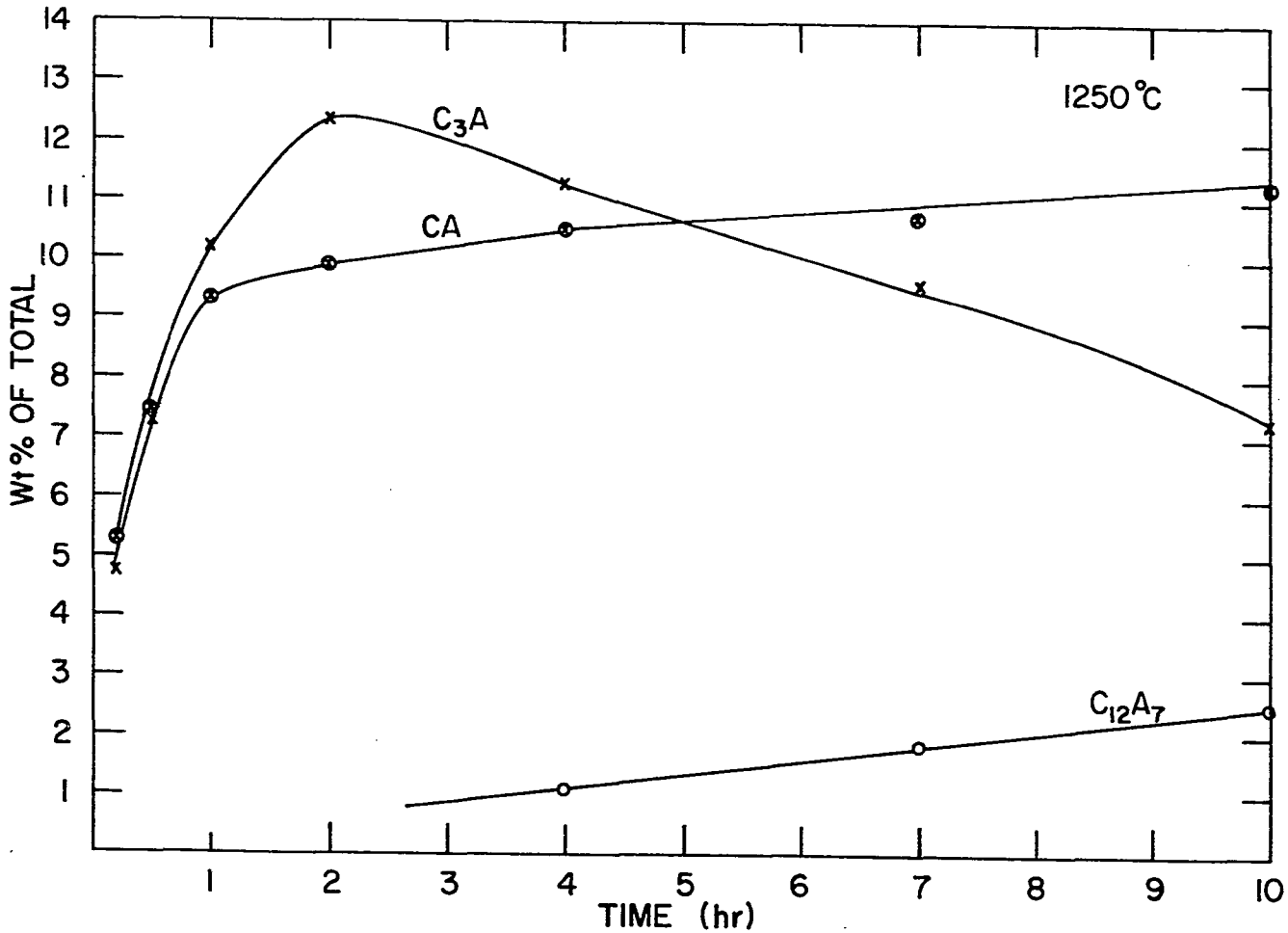

Fig. 39. Formation of aluminates at 1250°C

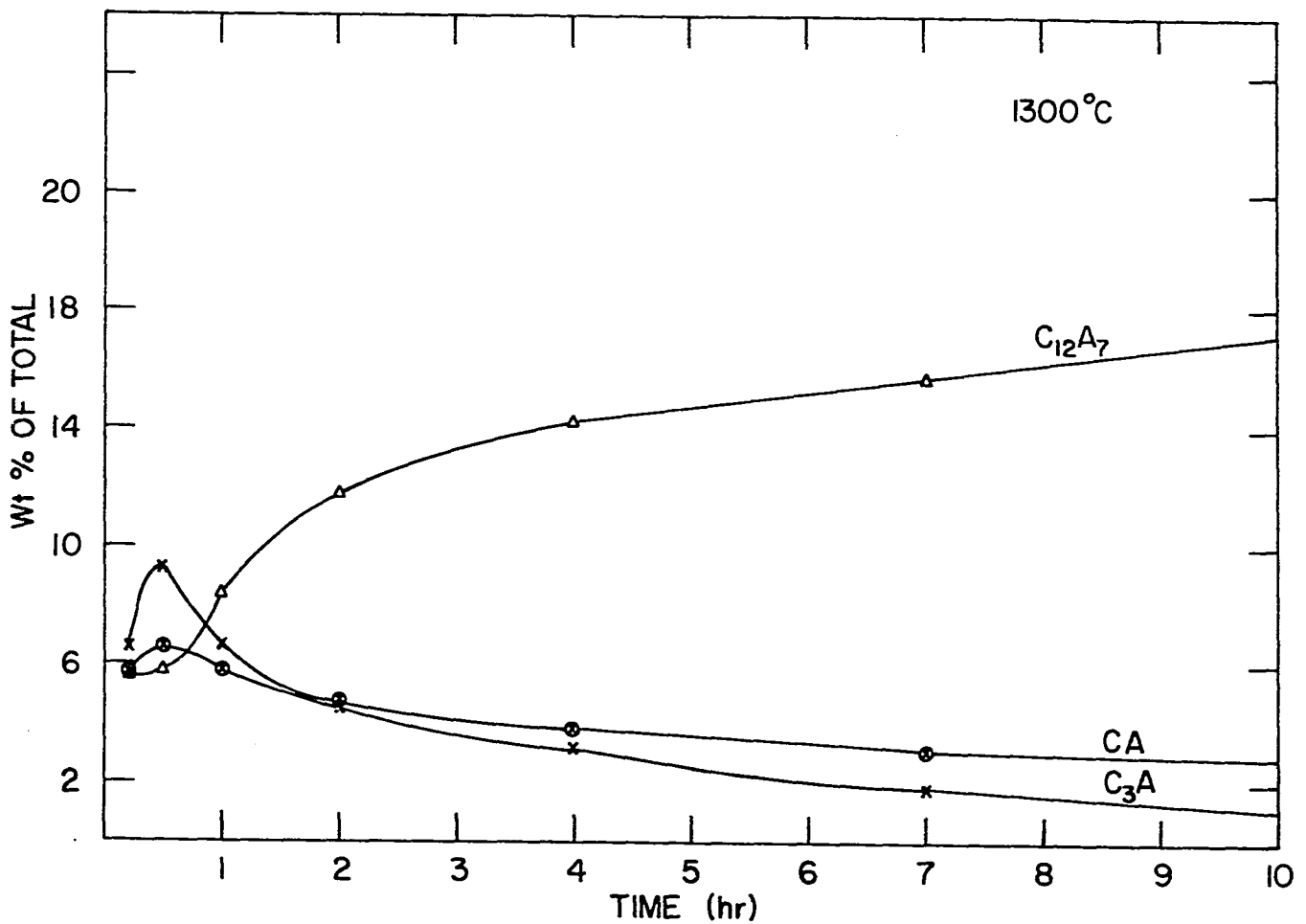

Fig. 40. Formation of aluminates at 1300°C

It increased with time from then on. The $C_{12}A_7$ phase probably formed in the 7- and 10-hour runs but not in the others. At 1250°C, the C_3A phase behaved the same as it did at 1200°C. However, the CA phase increased over the entire span. The $C_{12}A_7$ phase was found only after 4 hours of sintering and the C_5A_3 phase was not found at all. When the sintering temperature was increased to 1300°C, the $C_{12}A_7$, along with CA and C_3A was found from the beginning. While CA and C_3A increased to maxima at the 0.5 hr run and then decreased, the $C_{12}A_7$ phase continued to increase with time.

In Table 11, the conversions of the three aluminates, CA, $C_{12}A_7$ and C_3A, for different runs are given. These numbers were calculated by dividing the alumina contents in each compound by the total alumina content in the sinter. Thus, a 50% conversion of the CA phase meant that half the Al_2O_3 in the sinter had transformed into CA.

Kinetic analysis of the formation of aluminates

With the conversion data of aluminates on hand, we can now try to find an equation which can best describe the formation kinetics for each aluminate. The kinetic equations tried here include:

Ginstling-Brounshtein equation:

$$\frac{K_{GB}}{r^2} t = 1 - \frac{2x}{3} - (1 - x)^{2/3} \qquad (27)$$

Valensi-Carter equation:

$$\frac{K_{vc}}{r^2} t = \frac{Z}{(Z - 1)} - (1 - x)^{2/3} - \frac{(1 + (Z - 1)x)^{2/3}}{(Z - 1)} \qquad (28)$$

Phase boundary equation:

$$\frac{K_{PB}}{r} t = 1 - (1 - x)^{1/3} \tag{29}$$

Avrami-Erofeev equation:

$$\ell n(1 - x) = - K_{AE} r^2 t^m \tag{30}$$

where K's are reaction constants, r is the radius of the particles, t is the reacting time, x is the conversion and Z and m are constants.

The first two equations are based on diffusion-controlled mechanisms. The third one is based on a phase-boundary-reaction-controlled mechanism, while the Avrami-Erofeev equation is derived from the concept of nucleation and crystal growth.

Since the particle size of the alumina powder is not uniform and the samples differ from each other to some extent, it is thus necessary to incorporate the particle size distribution of Al_2O_3 into the kinetic equations to get accurate results. The particles are divided into 16 groups based on data obtained from the Coulter counter. The diameters of each group are set up according to the following relationship:

$$d_1,\ d_2(= pd_1),\ d_3(= p^2 d_1),\ \ldots\ d_{16}(= p^{15} d_1) \tag{31}$$

The smallest diameter and the p value in this case are 0.63μ and 1.26, respectively. In order to illustrate how to introduce the particle size distribution into kinetic equations, the Ginstling-Brounshtein equation will be used as an example. Similar procedures can be applied to the other equations. When the size distribution is substituted

into the Ginstling-Brounshtein equation, a set of 16 equations are obtained:

$$\begin{cases} \dfrac{K_{GB}t}{d_1^2} = 1 - \dfrac{2x_1}{3} - (1 - x_1)^{2/3} \\ \dfrac{K_{GB}t}{p^2 d_1^2} = 1 - \dfrac{2x_2}{3} - (1 - x_2)^{2/3} \\ \quad \vdots \\ \dfrac{K_{GB}t}{p^{30} d_1^2} = 1 - \dfrac{2x_{16}}{3} - (1 - x_{16})^{2/3} \end{cases} \tag{32}$$

For a certain time t, the conversions for each group are x_1, x_2 ... x_{16}. The overall conversion x will then be:

$$x = \sum_{n=1}^{16} m_n x_n, \tag{33}$$

where m_n is the weight fraction of each group. Theoretically, using the above 17 equations, we can now solve for the 17 unknowns: x_1, x_2 .... x_{16} and K_{GB}. The overall conversion x, time t, constants p and d_1 are already known. However, this set of equations are too complex to be solved analytically. Empirical methods had to be used as described below.

First, the Ginstling-Brounshtein equation is plotted as a function of x. This plot facilitates the calculation procedure. Then, when $x_1 = 1.0$, i.e. the particles in the first group (smallest) have just completely reacted, we can calculate the value of $K_{GB}t$ from the first equation of the set. With this number of $K_{GB}t$, we then know $\frac{K_{GB}t}{p^2 d_1^2}$, $\frac{K_{GB}t}{p^4 d_1^2}$, ... $\frac{K_{GB}t}{p^{30} d_1^2}$. Thus from the plot made earlier, we can obtain the conversions of the other groups x_2, x_3, ... x_{16}. Then

the overall conversion can be calculated from Eq. (33). One set of data (x, $K_{GB}t$) is therefore obtained. The second set of such data can be obtained by assuming that the particles in group 2 have just completely reacted. Of course, at this time the conversion of the first group is already 1.0. For small values of $K_{GB}t$, we can assume x_1 = 0.5, 0.75, 0.9, ... etc. Finally, a plot of x versus $K_{GB}t$ can be obtained. One such plot for the Ginstling-Brounshtein equation is shown in Fig. 41. When a real conversion value is obtained, we can get the $K_{GB}t$ value from this plot and then divide it by the reaction time to get the reaction constant K_{GB}. The uniformity of this K value is then used to evaluate the kinetic equations. An equation which can best describe the real reactions will produce a uniform K.

Through a series of trials, it was found that both the Ginstling-Brounshtein and the Valensi-Carter equations fit the data quite well, with the latter being slightly better. The other two equations failed to produce uniform K values.

In the Valensi-Carter equation, a Z factor is included to account for the change in volume. The Z factor is defined as the volume of the reaction product formed per unit volume of reactant consumed. Since in the case of reactions between CaO and Al_2O_3 the diffusing cation is the Ca^{+2}, the alumina particles are thus considered as the host, i.e. the reactant named in the definition of the Z factor. The densities of Al_2O_3, CA, C_3A and $C_{12}A_7$ as obtained from the literature are 3.99, 2.98, 3.03 and 2.70 gm/cm^3, respectively. Thus the Z factors for CA, C_3A and $C_{12}A_7$ are 2.08, 3.49 and 2.87, respectively. An implicit assumption is made in the calculation, that the phases formed during the

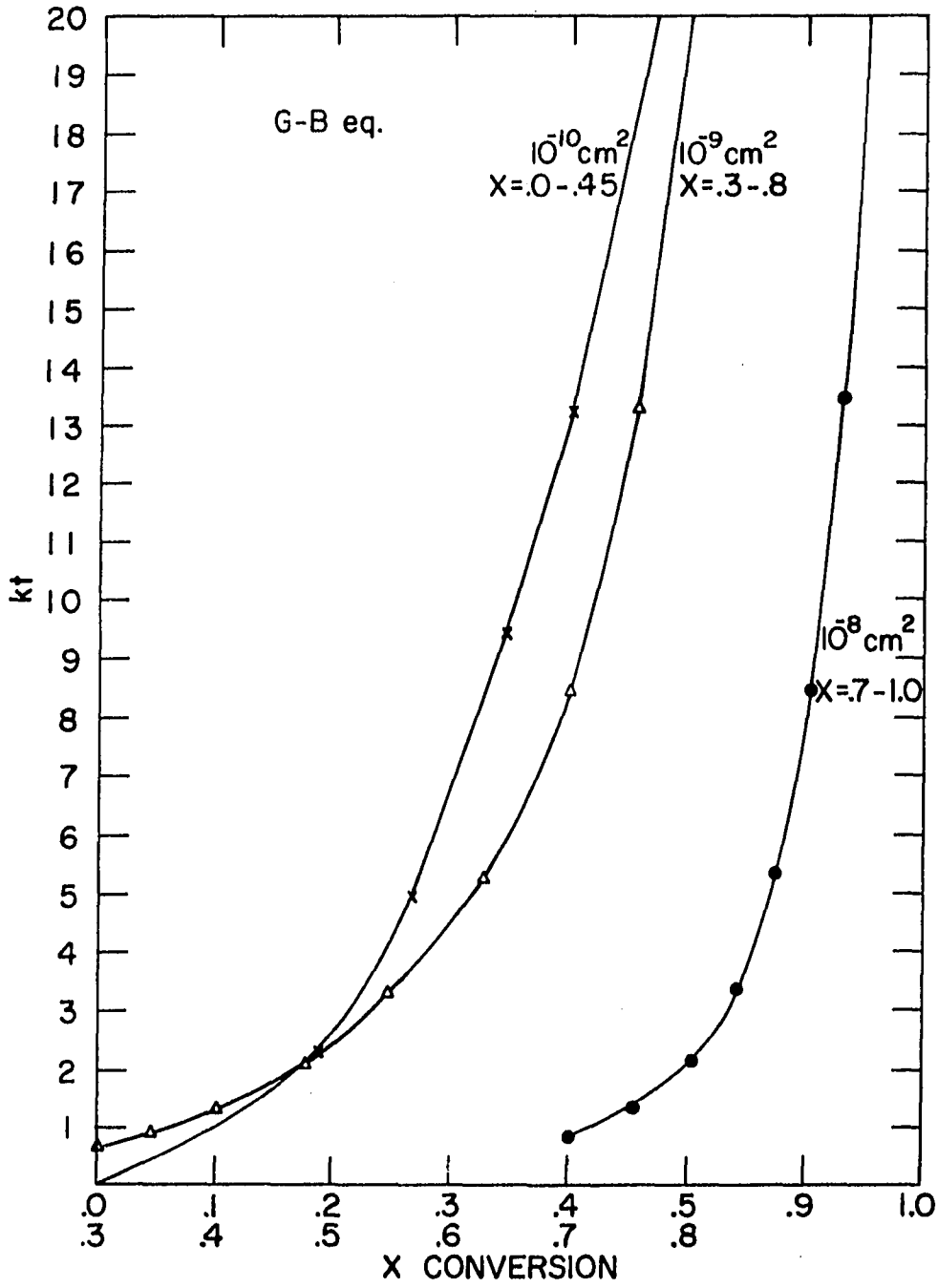

Fig. 41. Relation between $K_{GB}t$ and conversion as calculated from the Ginstling-Brounshtein equation and the particle size distribution of Al_2O_3

reactions have the ideal densities. The Valensi-Carter equations for the three aluminates are therefore as follows.

For CA:

$$\frac{K_{vc}t}{d^2} = 1.926 - (1 - x)^{2/3} - (1 + 1.08x)^{2/3}/1.08 \qquad (34)$$

For C_3A:

$$\frac{K_{vc}t}{d^2} = 1.402 - (1 - x)^{2/3} - (1 + 2.49x)^{2/3}/2.49 \qquad (35)$$

For $C_{12}A_7$:

$$\frac{K_{vc}t}{d^2} = 1.535 - (1 - x)^{2/3} - (1 + 1.87x)^{2/3}/1.87 \qquad (36)$$

The plots of the right-hand sides of the above three equations are given in Fig. 42. Values of x versus $K_{vc}t$ for these three equations are calculated according to the particle size distribution of Al_2O_3 and are shown in Figs. 43-45.

In Figs. 46-55, the calculated Kt values for different aluminates at different temperatures are plotted versus sintering time. As can be seen, both the Ginstling-Brounshtein and Valensi-Carter equations generate fairly good straight lines for both increasing and decreasing sections. Now the formation of the three aluminates being studied will be discussed separately.

The C3A phase Formation kinetics can be studied only for that section of the sintering runs during which the quantity of the phase of interest is increasing with time. When the quantity begins to decrease, it simply means that a different kind of reaction is occurring and the data obtained can no longer be used. One value of K was obtained

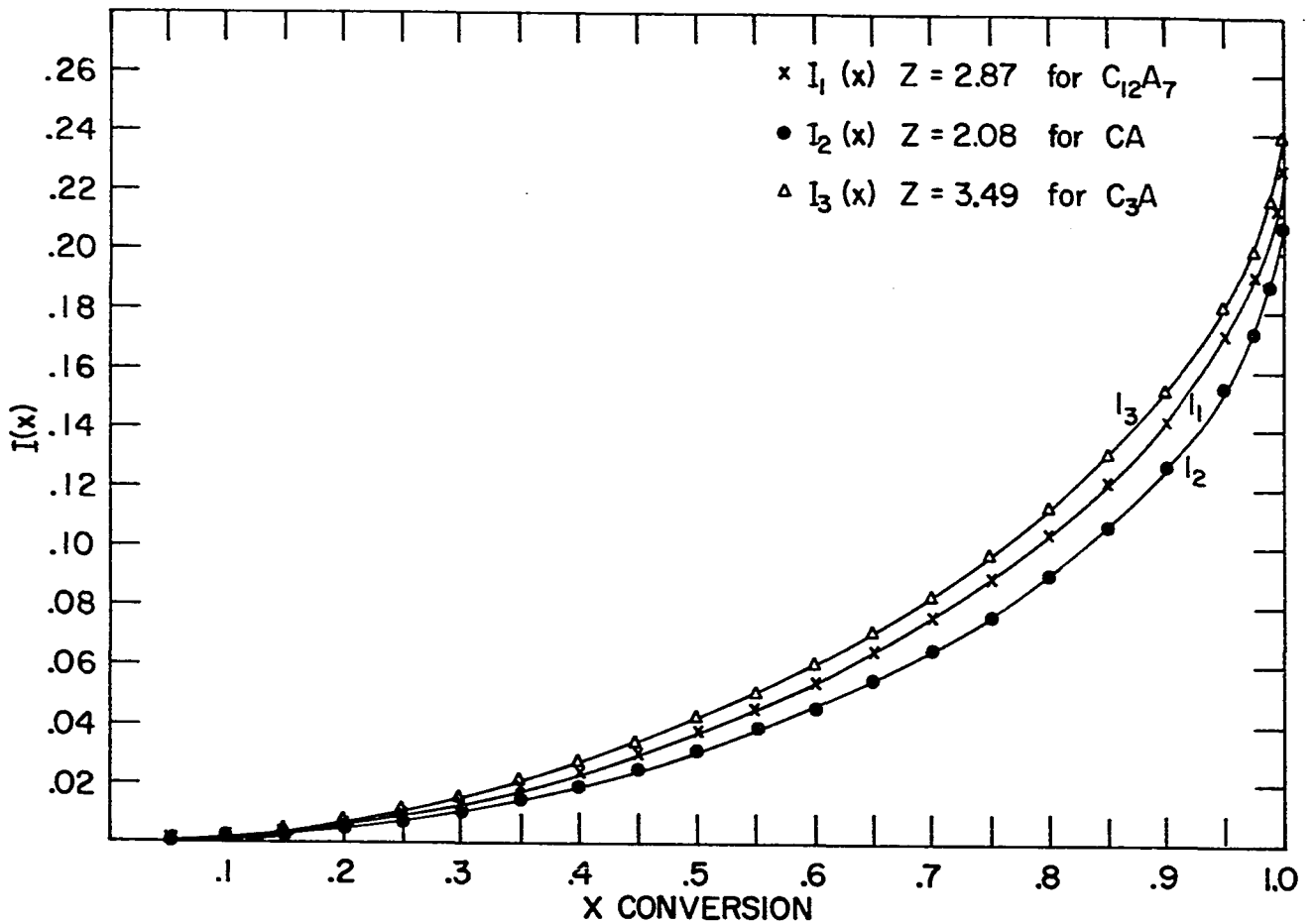

Fig. 42. The Valensi-Carter equations for $C_{12}A_7$, CA and C_3A as functions of conversion

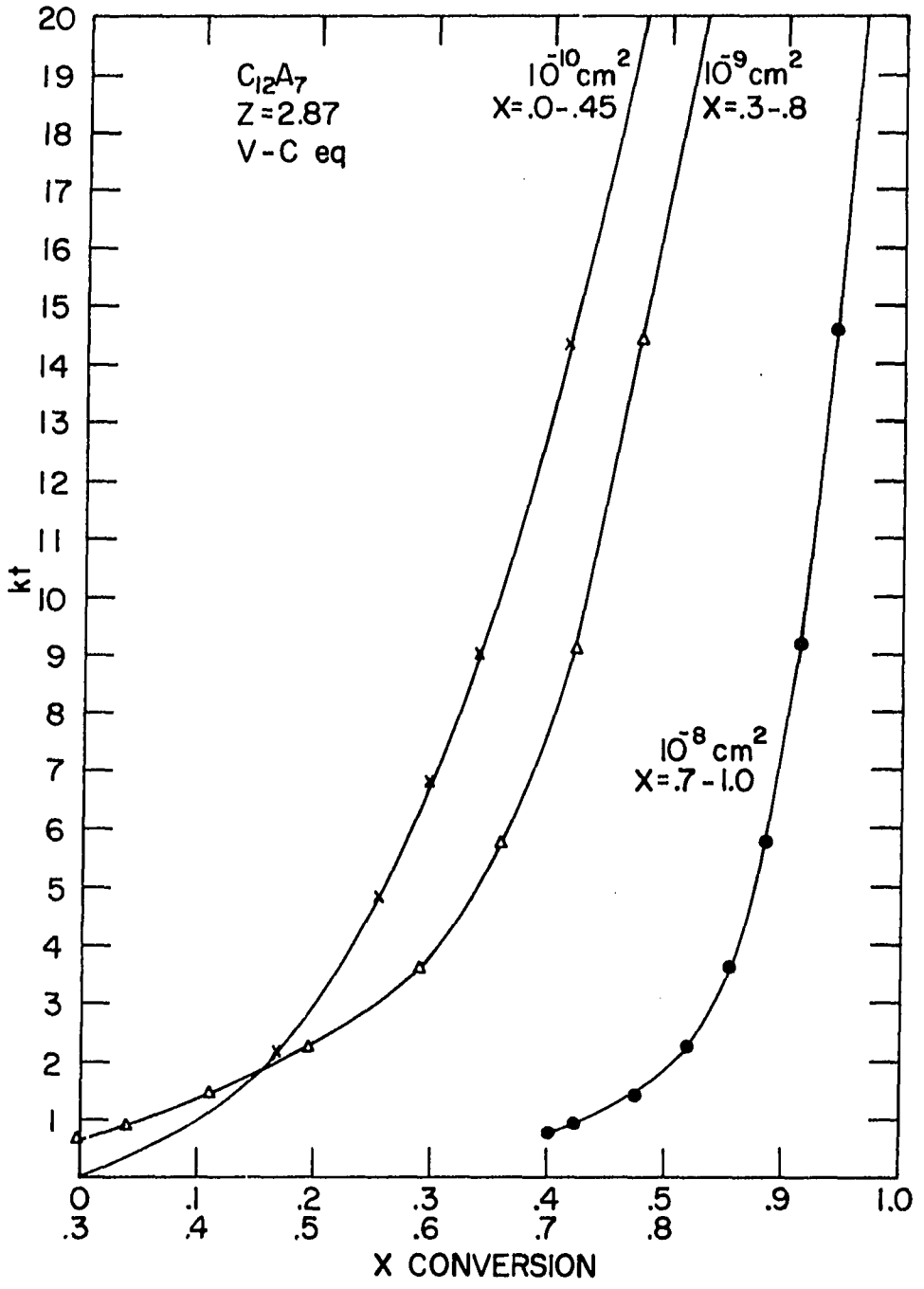

Fig. 43. Relation between $K_{VC}t$ and x as calculated from the Valensi-Carter equation for $C_{12}A_7$ and the particle size distribution of Al_2O_3

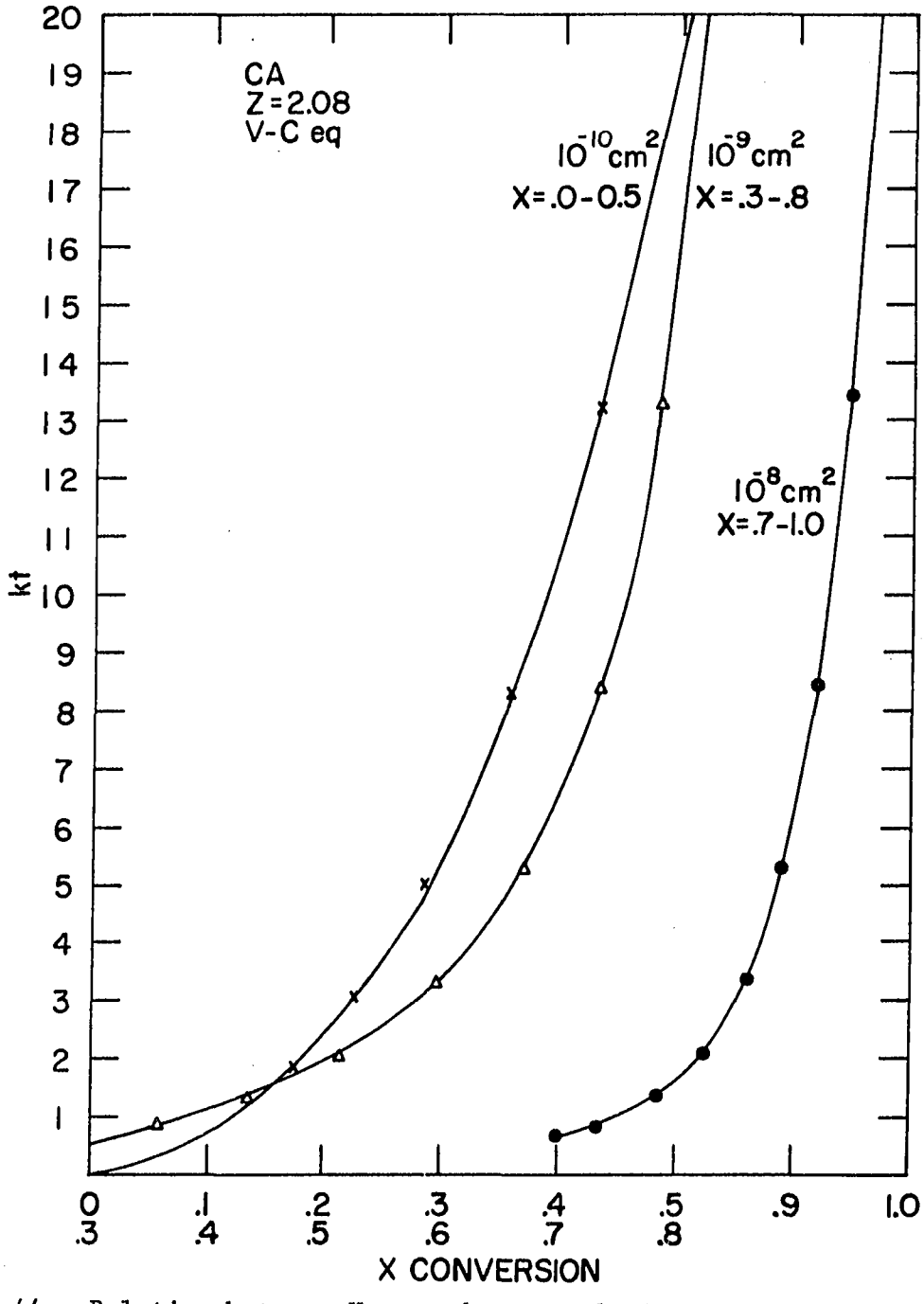

Fig. 44. Relation between $K_{VC}t$ and x as calculated from the Valensi-Carter equation for CA and the particle size distribution of Al_2O_3

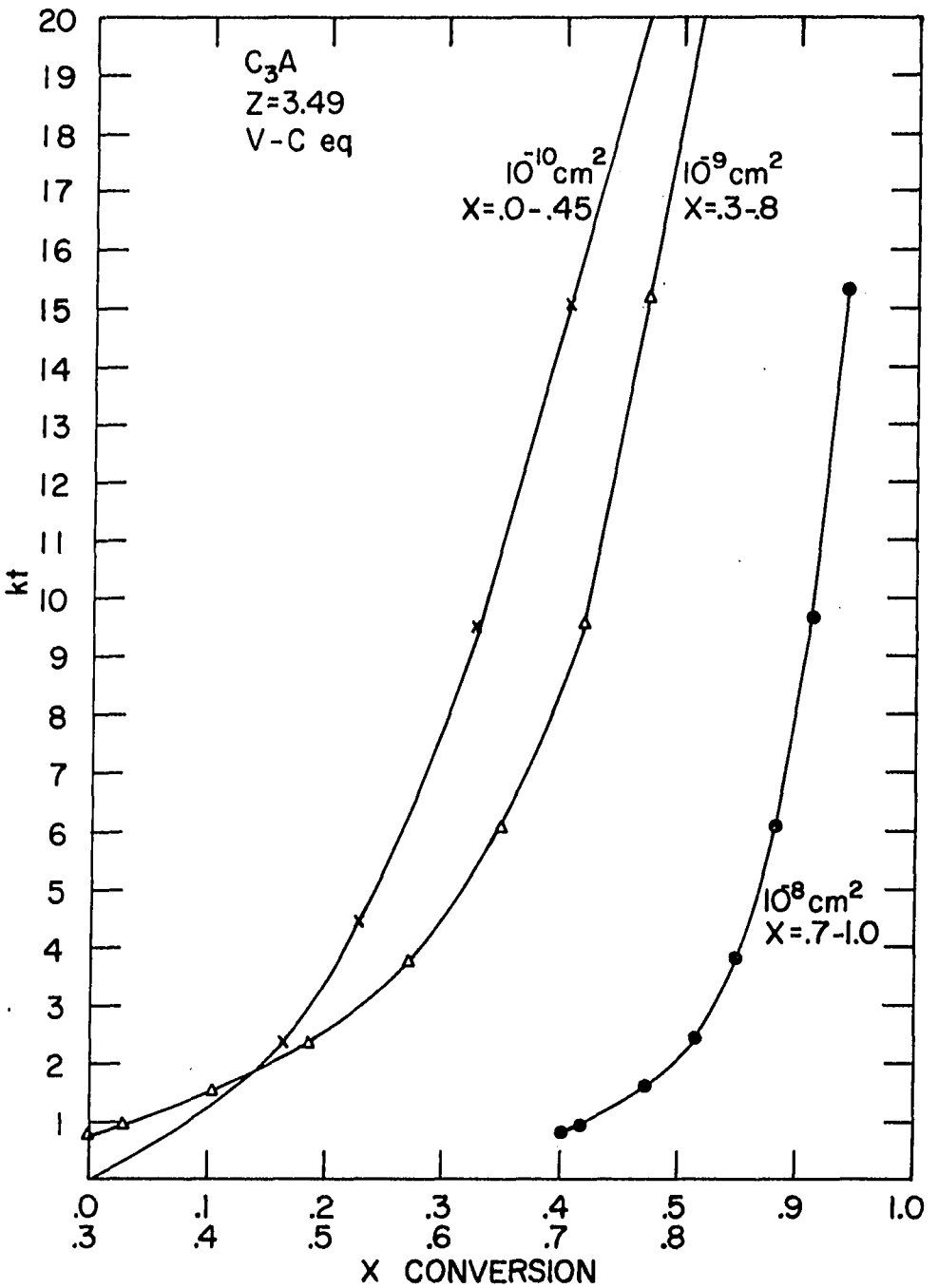

Fig. 45. Relation between $K_{VC}t$ and x as calculated from the Valensi-Carter equation for C_3A and the particle size distribution of Al_2O_3

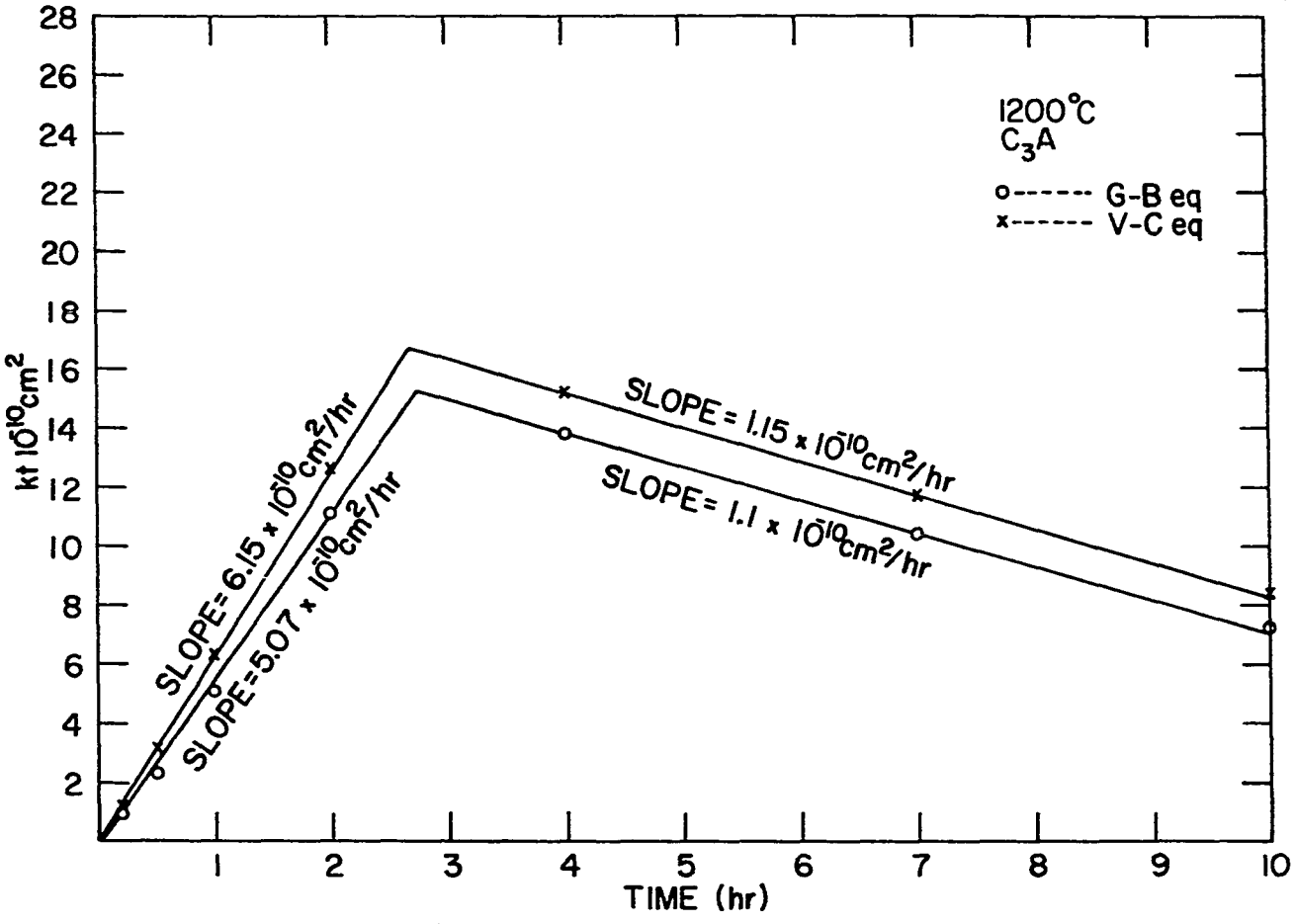

Fig. 46. Relation between Kt and sintering time for the C_3A phase at 1200°C

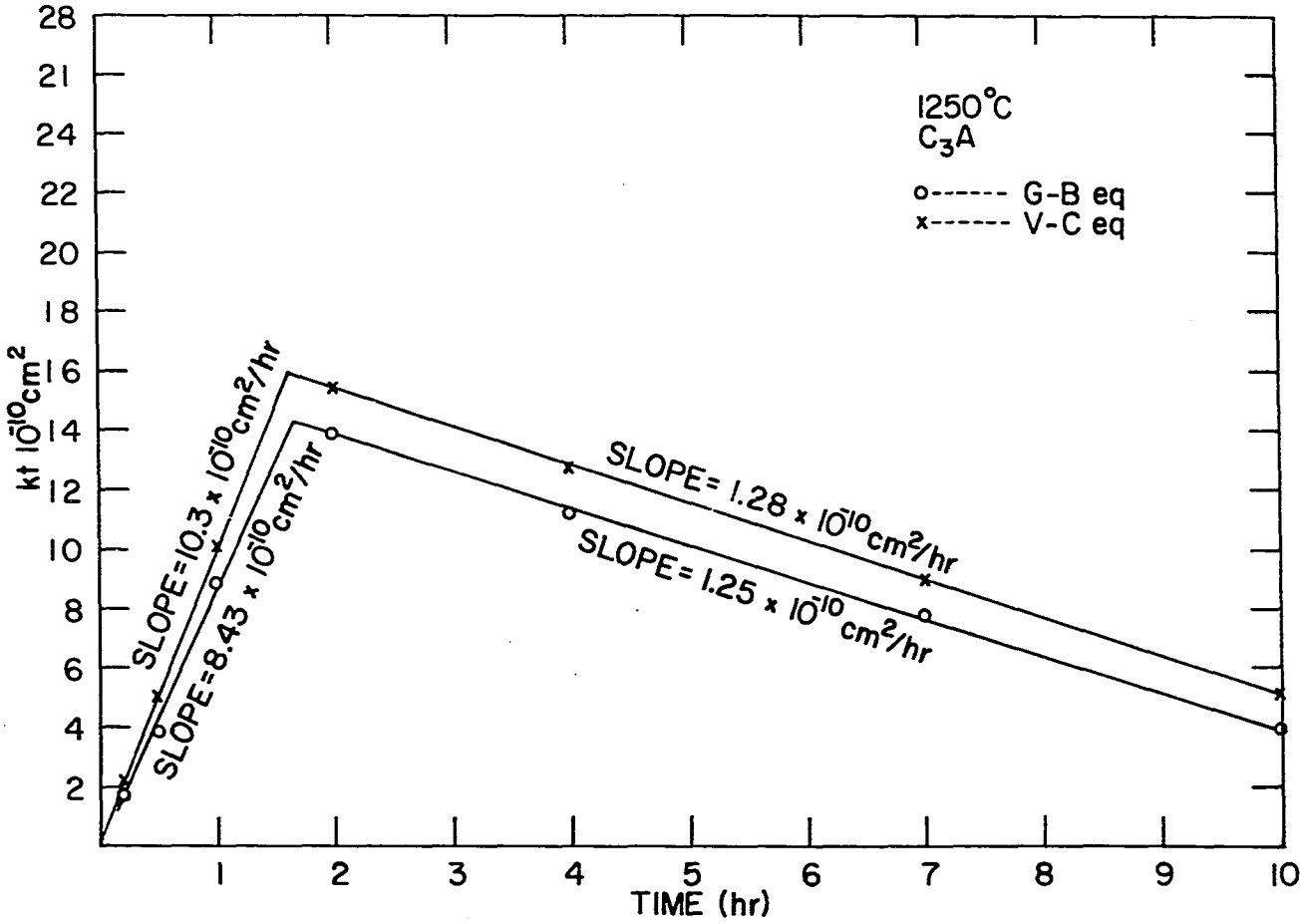

Fig. 47. Relation between Kt and sintering time for C_3A at 1250°C

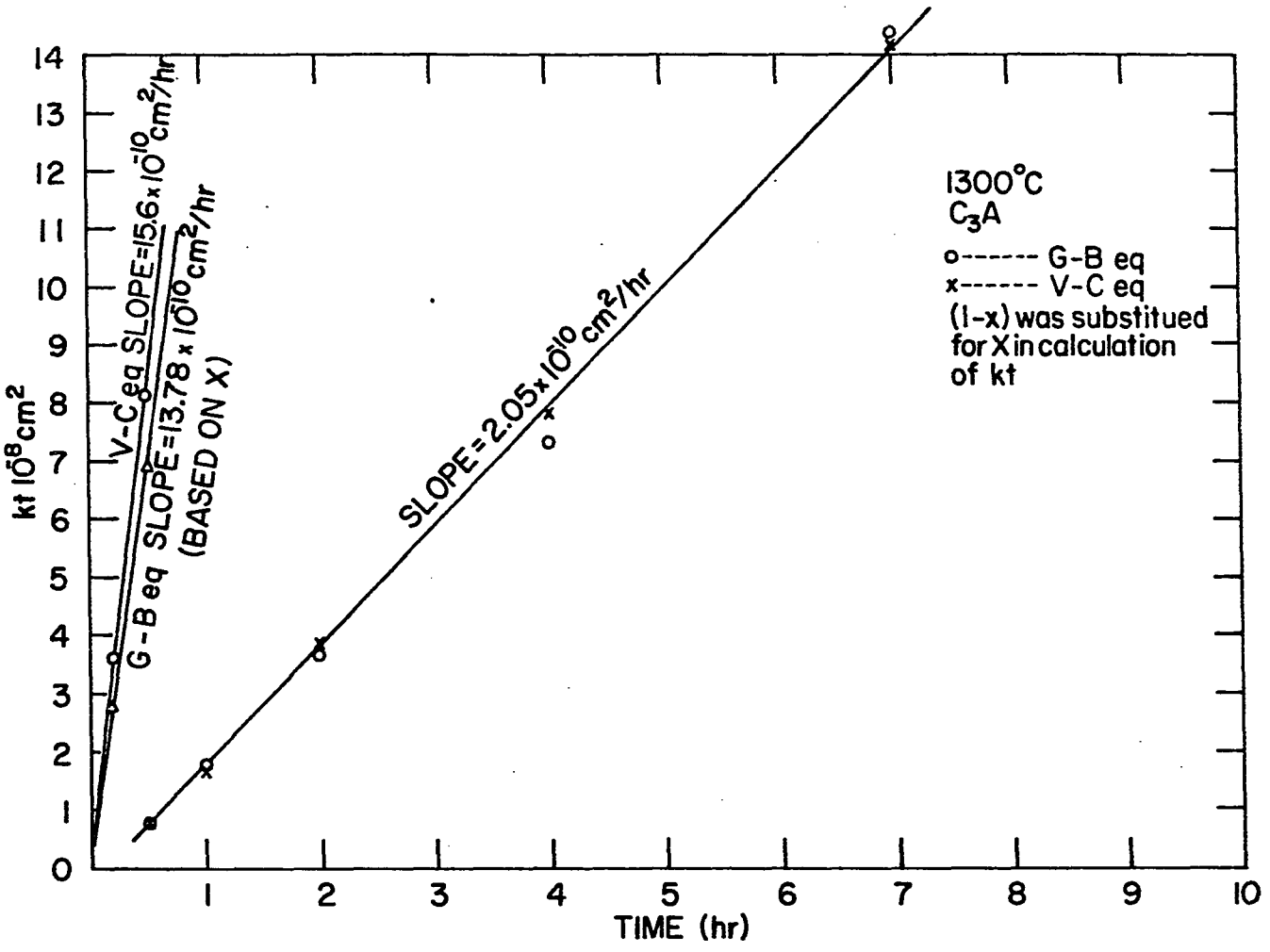

Fig. 48. Relation between Kt and sintering time for C_3A at 1300°C. Values of (1 - x) were substituted for x in the calculation of Kt except for the beginning period

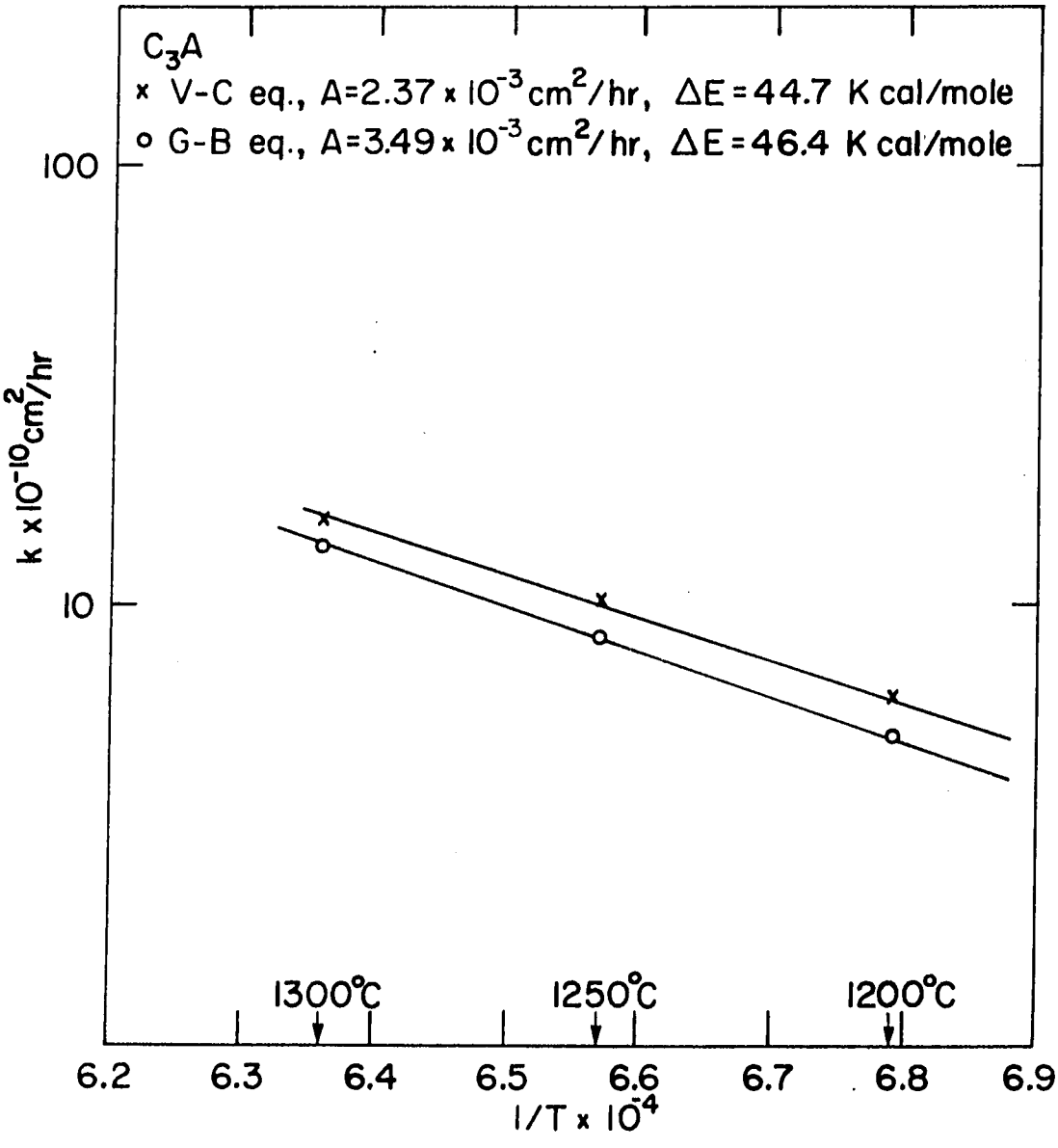

Fig. 49. Relation between ℓn K and $\frac{1}{T}$ for the formation of C_3A

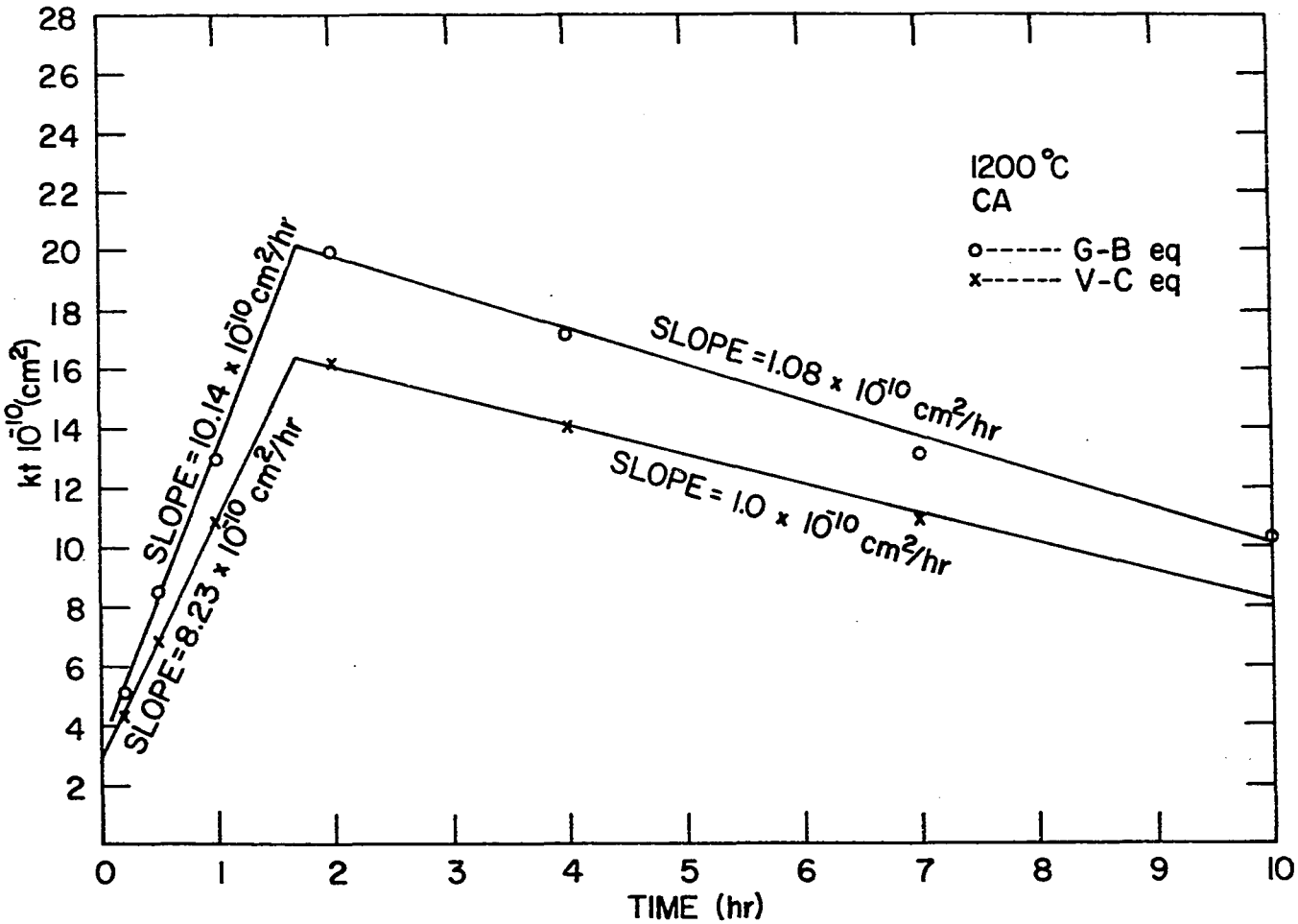

Fig. 50. Relation between Kt and sintering time for CA at 1200°C

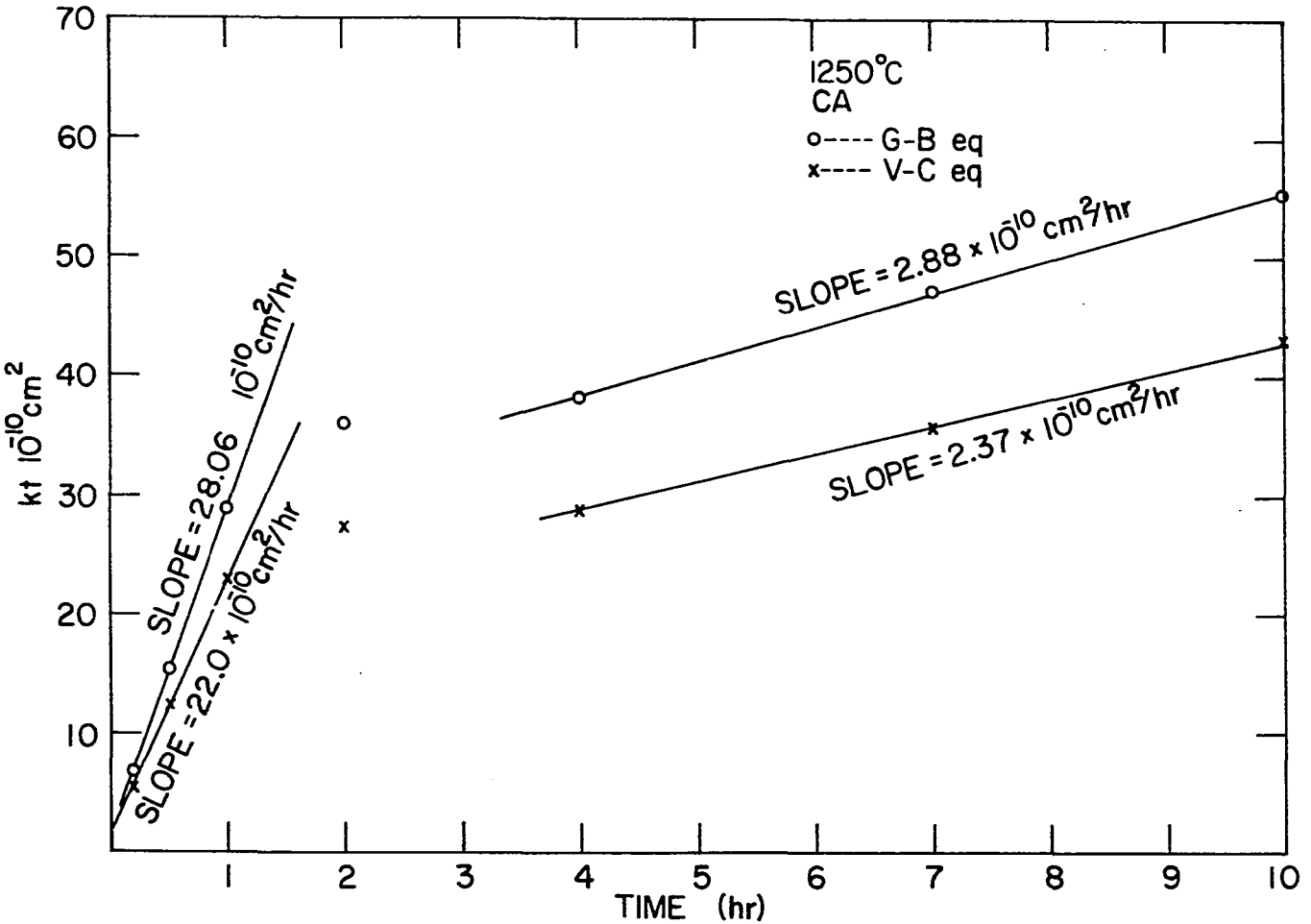

Fig. 51. Relation between Kt and sintering time for CA at 1250°C

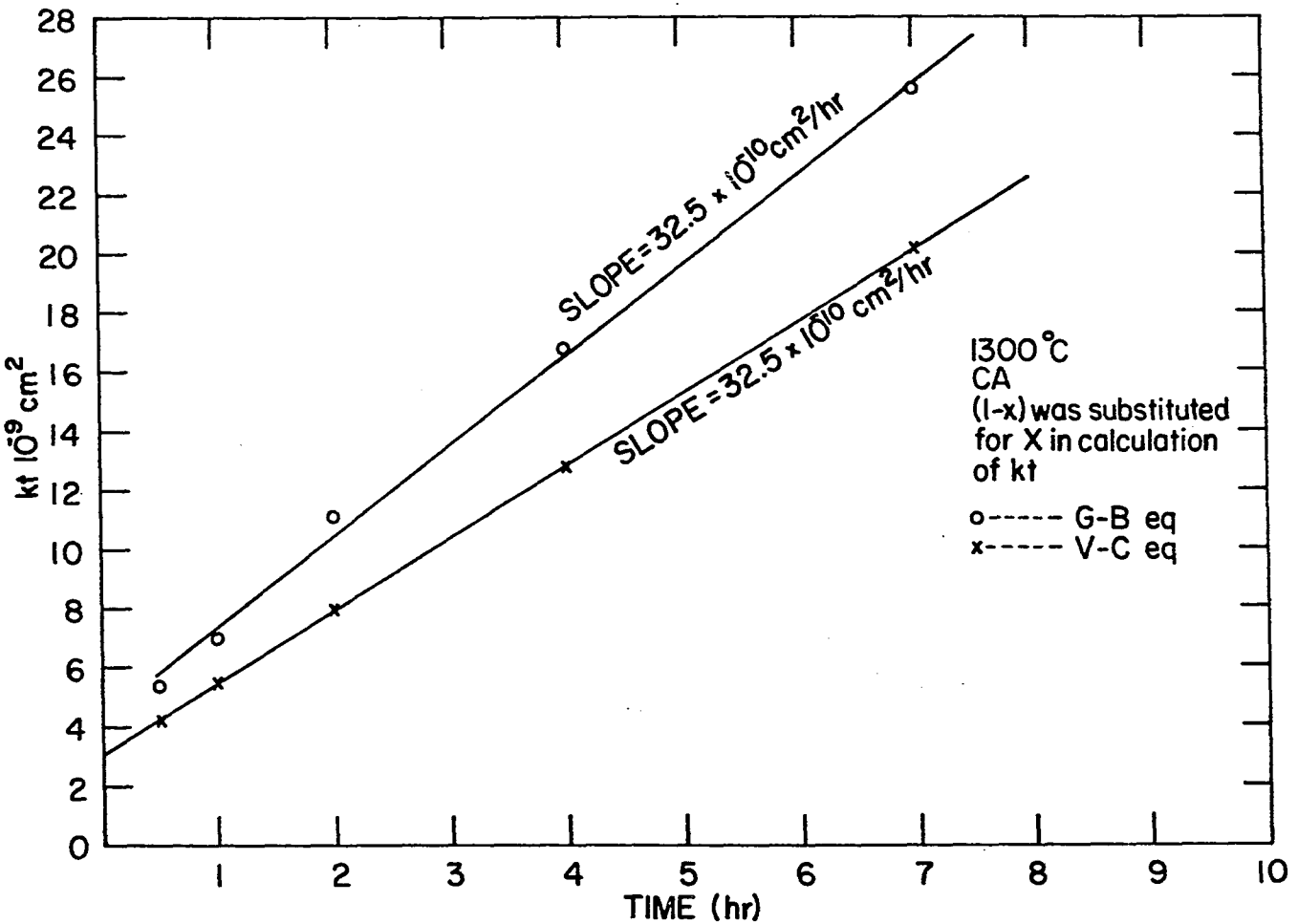

Fig. 52. Relation between Kt and sintering time for CA at 1300°C. Values of (1 - x) were substituted for x in the calculation of kt

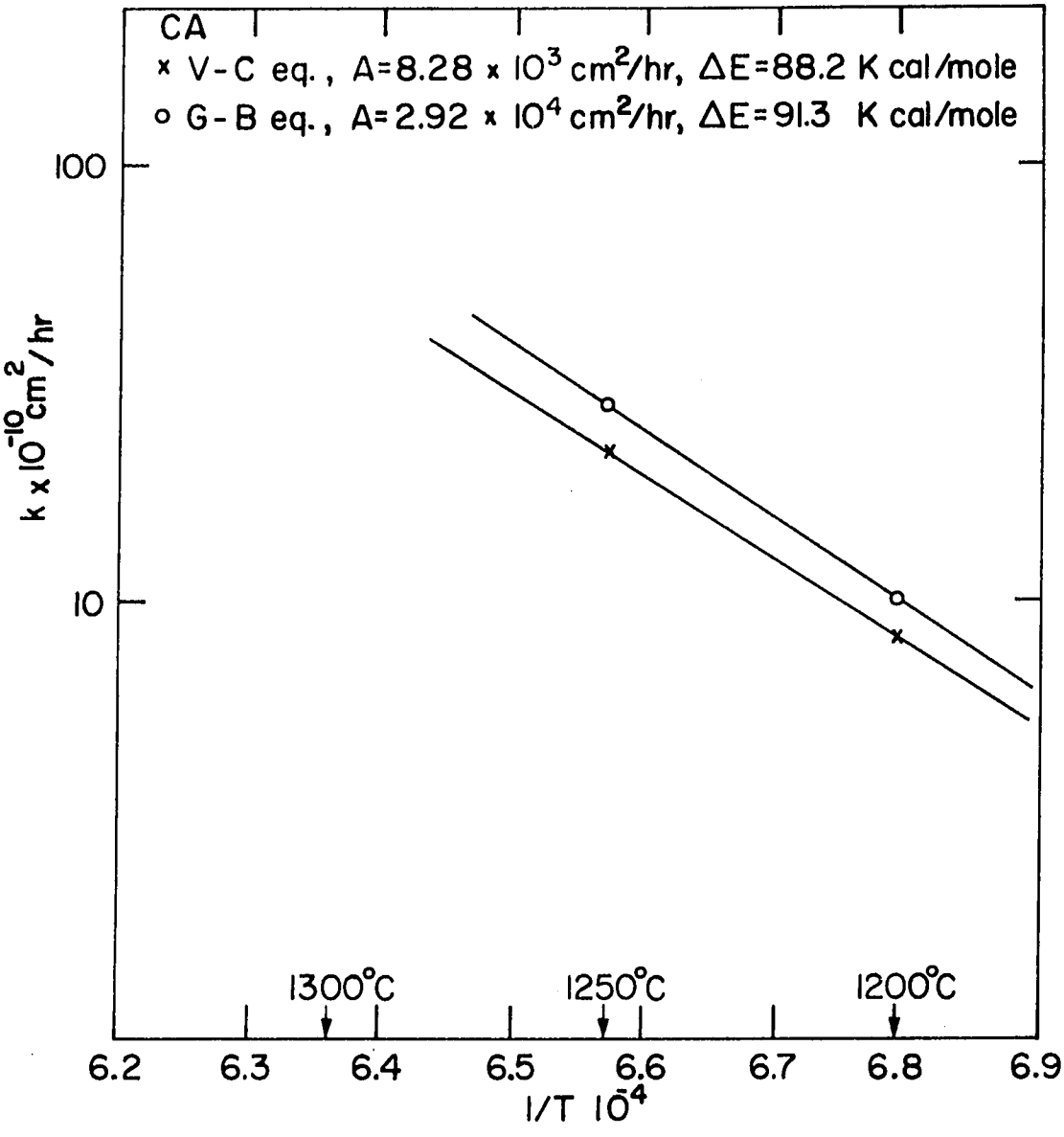

Fig. 53. Relation between ℓn K and $\frac{1}{T}$ for the formation of CA

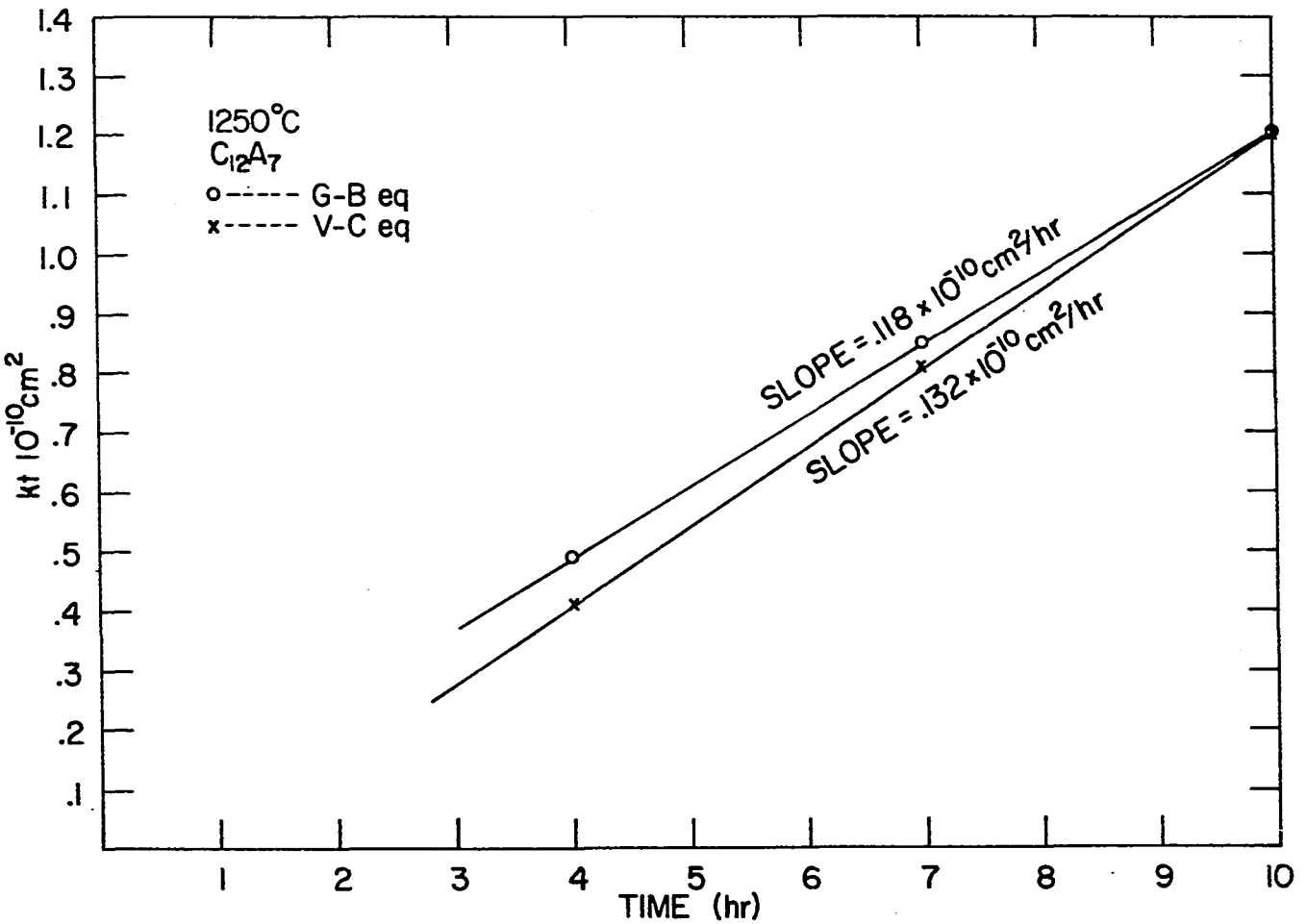

Fig. 54. Relation between Kt and sintering time for $C_{12}A_7$ at 1250°C

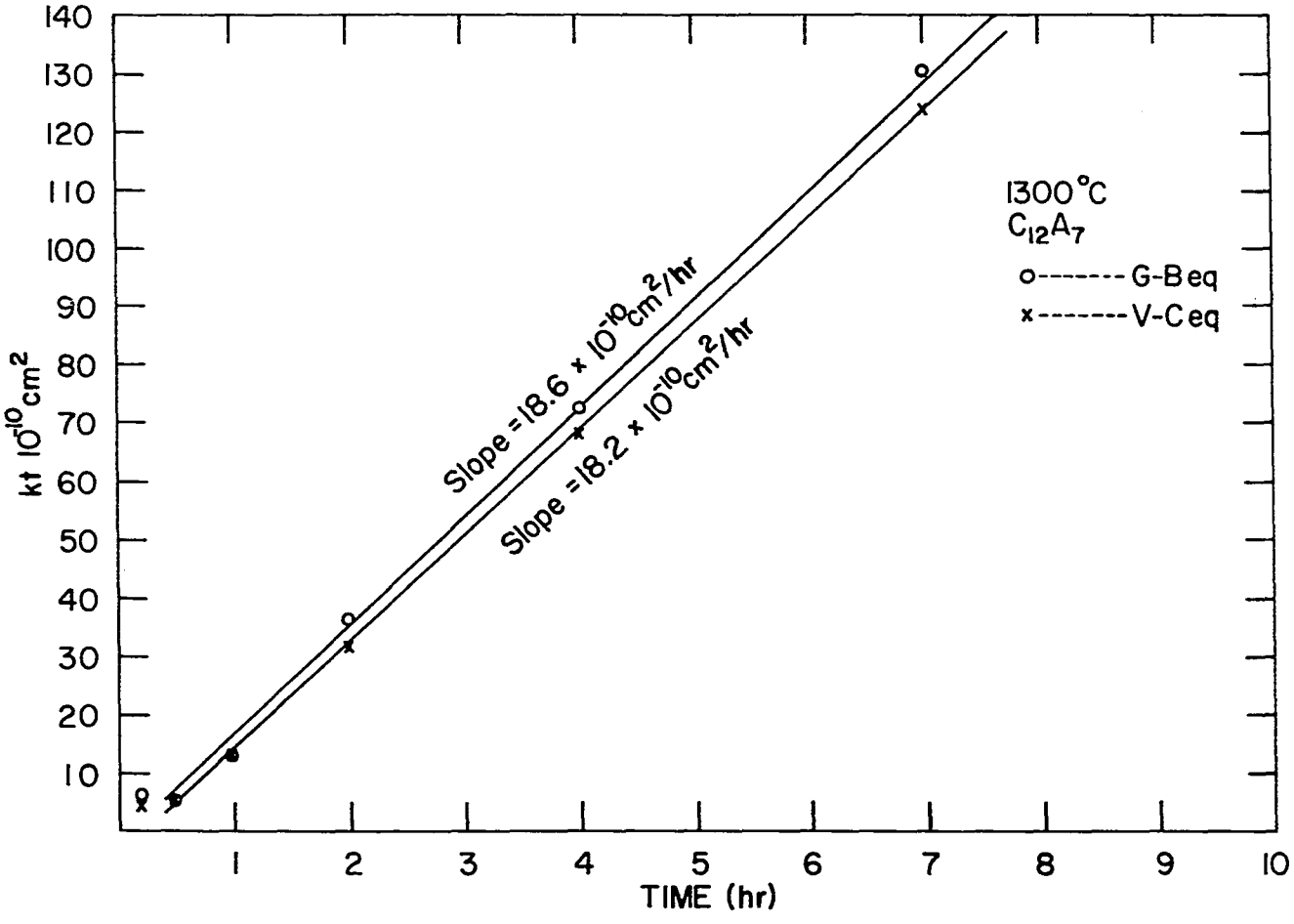

Fig. 55. Relation between Kt and sintering time for $C_{12}A_7$ at 1300°C

for each temperature investigated. The value of K would be expected to follow the Arrhenius equation, $K = A \exp(-Q/RT)$. To determine if this is true, a graph of ℓn K versus 1/T was plotted as shown in Fig. 49. The straight line obtained indicates that the two diffusion-controlled kinetic equations describe quite well the formation of C_3A. The activation energy obtained in this case is 45.6 Kcal/mole, which is about the same as the value (48.2 Kcal/mole) obtained by MacKenzie and Banerjee (59). They used three moles of CaO and one mole of Al_2O_3 as the starting material, which is different than for the current study. Yet the activation energy for the formation of C_3A is essentially the same, suggesting that the true mechanism governing the formation of this compound is universal regardless of the starting material.

The quantities of C_3A decreased with time for all three temperatures tested after reaching a maximum in each case. The kinetic equations of both Ginstling-Brounshtein and Valensi-Carter are derived for the conversion of particles. If the equations are written for the unconverted part of the particles, an equivalent expression will be obtained with (1 - x) substituted for x, where x has the same meaning as before. At 1300°C, this idea was applied to the decreasing section of the time versus conversion plot for C_3A and later to the CA phase. The results for C_3A are plotted on Fig. 48 and show that a straight line is obtained, indicating again that the reactions are controlled by a diffusion process.

The reasons why the kinetics for the decreasing sections were not studied should be expanded upon. At 1200°C, when C_3A decreased, CA also decreased and C_5A_3 was formed as a result. At 1250°C, however,

when C_3A decreased, both CA and $C_{12}A_7$ were on the rise. Yet at 1300°C, both CA and C_3A decreased to form $C_{12}A_7$. Thus, it is meaningless to study these sections of the curves because they are related to different reactions.

The CA phase All studies indicated that this phase was the first dominant one in our system. The activation energy for its formation was determined to be 89.8 Kcal/mole as shown in Fig. 53. Only data from runs at 1200°C and 1250°C were used. At 1300°C, the K value was too different to be in line with the other two values. Ito, et al. (40, 41) studied the formation of this phase from the reactions between $C_{12}A_7$ and CA_2. They found that the apparent activation energies for the formation of the CA phase on the surface of $C_{12}A_7$ and CA_2 phases are 120 Kcal/mole and 84 Kcal/mole, respectively. Obviously, our value of 89.8 Kcal/mole is very close to what they reported as the formation energy of CA on the CA_2 phase. In order for CA to be formed on the CA_2 phase, Ca ion has to diffuse through the layer of CA from the other side to reach the interface between CA and CA_2. Thus it appears that the activation energy we obtained is really the activation energy of the diffusion process of Ca ion in the CA phase. The decreasing sections of the curves were not studied for the same reasons given for C_3A.

The $C_{12}A_7$ phase At 1250°C, the CA phase increased with $C_{12}A_7$, while C_3A decreased. At 1300°C, both CA and C_3A decreased to form $C_{12}A_7$. It is obvious that we should not compare these two sets of data directly as we did for the C_3A and CA cases.

The reason why CA increased with $C_{12}A_7$ at 1250°C probably lies in

the stability of the $C_{12}A_7$ phase and the existence of unreacted alumina. When C_3A is converted to $C_{12}A_7$, some Ca ion has to diffuse away, since the C_3A phase is richer in calcium than $C_{12}A_7$. In the presence of unreacted Al_2O_3, more CA will be formed as a result.

When the temperature is increased to 1300°C, the $C_{12}A_7$ phase is more stable than ever. The Ca ion which diffuses away from C_3A will then react with CA to form $C_{12}A_7$ at the interface of CA and $C_{12}A_7$, thus causing the CA phase to decrease, too.

We can now propose an overall mechanism which will describe the formation of the different aluminates in the sample. The first product between CaO and Al_2O_3 is probably $C_{12}A_7$ which does not increase with time immediately because of stability reasons. When the temperature and time increase, CA is formed and at the same time $C_{12}A_7$ either disappears or exists in very minute amounts. As alumina particles are converted to CA, the continued diffusion of calcium ion will then form the intermediate phase, C_3A. Finally when the calcium oxide is totally consumed, the $C_{12}A_7$ phase will begin to form again, this time at the expense of CA and C_3A. At lower temperatures, some C_5A_3 instead of $C_{12}A_7$ will form. A few simple diagrams will help to illustrate the above summary. In the diagrams (Fig. 56), the C_5A_3 phase is not shown for purposes of simplicity. The calcium content of C_5A_3 is between that of CA and $C_{12}A_7$, so it will be formed at the interface between CA and $C_{12}A_7$. Under the right conditions, the C_5A_3 phase will grow instead of $C_{12}A_7$. In our high temperature X-ray study, the CA_2 phase was observed. This phase would be formed between CA and Al_2O_3 and its

$CaO|C_{12}A_7|Al_2O_3$ (a)

$CaO|C_{12}A_7|CA|Al_2O_3$ diffusion direction of Ca ion → (b)

$CaO|C_3A|C_{12}A_7|CA|Al_2O_3$ (c)

$C_3A|C_{12}A_7|CA$ (d)

Fig. 56. Mechanisms of formation of aluminates: (a) $C_{12}A_7$ is the primary product; (b) CA is the first dominant phase; (c) C_3A is formed as more Ca ion diffuse into the CA phase; and (d) $C_{12}A_7$ is finally formed at the expense of CA and C_3A

formation is probably caused by local excesses of Al_2O_3.

Thermodynamic study of reactions in the CaO-Al2O3 system

The study of the formation of aluminates will not be complete without a look at the thermodynamic aspects of the reactions. The standard free energy change of the reactions as a function of temperature will be calculated and compared with the experimental results. The calculations are based on the following equations:

$$\frac{d\left(\frac{\Delta(G_T^o)}{T}\right)}{dT} = -\frac{\Delta H_T^o}{T^2} \tag{37}$$

where $$\Delta H_T^o = \Delta H_{298}^o + \int_{298}^{T} \Delta Cp^o dT \tag{38}$$

and $$\Delta Cp^o = \sum_{i=1}^{n} q_i Cp_i^o \tag{39}$$

Equation (37) can also be written in a more practical way as:

$$\frac{\Delta G_T^o}{T} - \left(\frac{\Delta G_T^o}{T}\right)_{298} = -\int_{298}^{T} \frac{\Delta H_T^o}{T^2} dT \tag{40}$$

Since the Cp_i^o, ΔH_{298}^o, and ΔG_{298}^o are known for all the compounds in the

$CaO-Al_2O_3$ system, the ΔG^o value as a function of temperature can be calculated. In Table 12, data collected from the literature are shown. The sources of these data are: 1) Bonnickson (10): for Cp's of aluminates; 2) Coughlin (18) for ΔH^o_{298} and ΔG^o_{298} of aluminates; 3) JANAF table (89) for the ΔH^o_{298} and ΔG^o_{298} of α and $\gamma-Al_2O_3$; and 4) Kelley (42) for the values of CaO. Similar studies have been made in the past (6, 63), but the investigators used different values for Cp's, ΔH^o_{298}'s and ΔG^o_{298}'s. Also, in the present calculation, the molar ratio of CaO/Al_2O_3 will be fixed at 1.8, which is the ratio in our samples. The transformation of $\alpha-Al_2O_3$ to $\gamma-Al_2O_3$ was observed to occur somewhere between 1000°C and 1100°C in the high temperature X-ray tests, so it will be assumed to occur at $T > 1300^oK$.

The free energy changes for the formation of aluminates from CaO and Al_2O_3 under the constraint of 1.8 mole CaO/mole Al_2O_3 are calculated at first. The respective reactions are as follows:

$$C + A \rightarrow CA \qquad (41)$$

$$\frac{12}{7} C + A \rightarrow \frac{1}{7} C_{12}A_7 \qquad (42)$$

$$\frac{9}{5} C + \frac{3}{5} A \rightarrow \frac{3}{5} C_3A \qquad (43)$$

$$\frac{1}{2} C + A \rightarrow \frac{1}{2} CA_2 \qquad (44)$$

The calculated functions of ΔG^o_T are

Reaction 41:

$$\Delta G^o_T = -1147 + 49.39T - 7.97T \ln T + 3.11 \times 10^{-3}T^2 + 3.2 \times 10^5 \frac{1}{T}$$

$$T \leq 1300^oK \qquad (45)$$

Table 12. Thermodynamic properties of several compounds of interest in this investigation

Compounds	$-\Delta H^{o}_{f,298}$ cal/mole	$-\Delta G^{o}_{f,298}$ cal/mole	S^{o}_{298} cal/mole-^{o}K	$Cp^{o}(T)$ (298^{o}K-1800^{o}K) cal/mole-^{o}K
CaO	151,900	144,400	9.5	$11.67 + 1.08 \times 10^{-3}T - 1.56 \times 10^{5}T^{-2}$
α-Al_2O_3	400,400	378,078	12.174	$27.43 + 3.06 \times 10^{-3}T - 8.47 \times 10^{5}T^{-2}$
γ-Al_2O_3	396,000	373,790	12.55	$16.37 + 11.1 \times 10^{-3}T$
C_3A	850,000	807,000	49.1	$62.28 + 4.58 \times 10^{-3}T - 12.01 \times 10^{5}T^{-2}$
				298-1310^{o}K
$C_{12}A_7$	4,630,500	4,400,200	249.7	$301.96 + 65.5 \times 10^{-3}T - 55.3 \times 10^{+5}T^{-2}$
				1310-1700^{o}K
				$228.52 + 98.44 \times 10^{-3}T$
CA	554,800	526,800	27.3	$36.01 + 5.96 \times 10^{-3}T - 7.96 \times 10^{5}T^{-2}$
CA_2	954,300	904,300	42.5	$66.09 + 5.48 \times 10^{-3}T - 17.8 \times 10^{5}T^{-2}$

$$\Delta G^{o}_{T} = -\ 965 - 27.43T + 3.09T\ \ell n\ T - 0.91 \times 10^{-3}T^{2} - 1.035 \times 10^{5}\ \frac{1}{T}$$

$$T > 1300^{o}K \qquad (46)$$

Reaction 42:

$$\Delta G^{o}_{T} = -\ 8709 + 39.88T - 6.761T\ \ell n\ T + 1.797 \times 10^{-3}T^{2} + 2.613 \times 10^{5}\ \frac{1}{T}$$

$$T \leq 1300^{o}K \qquad (47)$$

$$\Delta G^{o}_{T} = 7041 - 110.25T + 14.79T\ \ell n\ T - 4.575 \times 10^{-3}T^{2} - 5.572 \times 10^{5}\ \frac{1}{T}$$

$$T > 1300^{o}K \qquad (48)$$

Reaction 43:

$$\Delta G^{o}_{T} = -\ 2145 + 41.09T - 6.54T\ \ell n\ T + 2.928 \times 10^{-3}T^{2} + 2.198 \times 10^{5}\ \frac{1}{T}$$

$$T \leq 1300^{o}K \qquad (49)$$

$$\Delta G^{o}_{T} = 3964 - 5.005T + 0.096T\ \ell n\ T + 0.516 \times 10^{-3}T^{2} - 0.342 \times 10^{5}\ \frac{1}{T}$$

$$T > 1300^{o}K \qquad (50)$$

Reaction 44:

$$\Delta G^{o}_{T} = -\ 10760 + 71.29T - 10.84T\ \ell n\ T + 4.45 \times 10^{-3}T^{2} + 4.06 \times 10^{5}\ \frac{1}{T}$$

$$T \leq 1300^{o}K \qquad (51)$$

$$\Delta G^{o}_{T} = -\ 579 - 5.523T + 0.22T\ \ell n\ T + 0\text{-}43 \times 10^{-3}T^{2} - 0.175 \times 10^{5}\ \frac{1}{T}$$

$$T > 1300^{o}K \qquad (52)$$

Table 13 contains the data calculated from these equations at 100°K intervals from 1000°K to 1700°K. As can be seen from this table and the corresponding sections, the compound most likely to form below 1300°K (1027°C) is $C_{12}A_7$. However, at temperatures above 1300°K, the most negative value is for the free energy change for the formation of CA. This is quite in accordance with what was observed during the experimental investigation. At lower temperatures, the $C_{12}A_7$ phase appeared for a short time. Then, as the temperature was increased, CA became the dominant phase and $C_{12}A_7$ would appear later.

Table 13. Standard free energy changes (ΔG_T^o) in calories for Reactions 41-44

Temperature °K	Reaction number			
	41	42	43	44
1000	- 13382	- 13474	- 3084	- 9495
1100	- 14159	- 14511	- 3583	- 10091
1200	- 14943	- 15570	- 4080	- 10692
1300	- 15726	- 16646	- 4570	- 11290
1400	- 9886	- 6676	- 1082	- 5250
1500	- 10330	- 6756	- 1352	- 5493
1600	- 10771	- 6831	- 1611	- 5729
1700	- 11213	- 6910	- 1859	- 5954

The free energy changes for the reactions between aluminates and CaO or Al_2O_3 can be obtained algebraically from Eqs. (45-52). The following reactions were selected for study in this way.

$$\frac{1}{12} C_{12}A_7 + \frac{5}{12} A \rightarrow CA \quad (53)$$

$$\frac{3}{35} C_{12}A_7 + \frac{27}{35} C \rightarrow \frac{3}{5} C_3A \quad (54)$$

$$\frac{3}{5} CA + \frac{6}{5} C \rightarrow \frac{3}{5} C_3A \quad (55)$$

$$\frac{1}{2} CA + \frac{1}{2} A \rightarrow \frac{1}{2} CA_2 \quad (56)$$

$$\frac{5}{14} C_3A + \frac{9}{14} CA \rightarrow \frac{1}{7} C_{12}A_7 \quad (57)$$

Calculated data for the above reactions and for Reactions 41-44 are shown in Fig. 57. Examination of these data shows that the $C_{12}A_7$ can be converted to CA, and CA to CA_2, when there is an excess of Al_2O_3. However, the other three reactions produce positive free energy changes, indicating that they will not proceed spontaneously. This seems contradictory to our observation of C_3A formation throughout

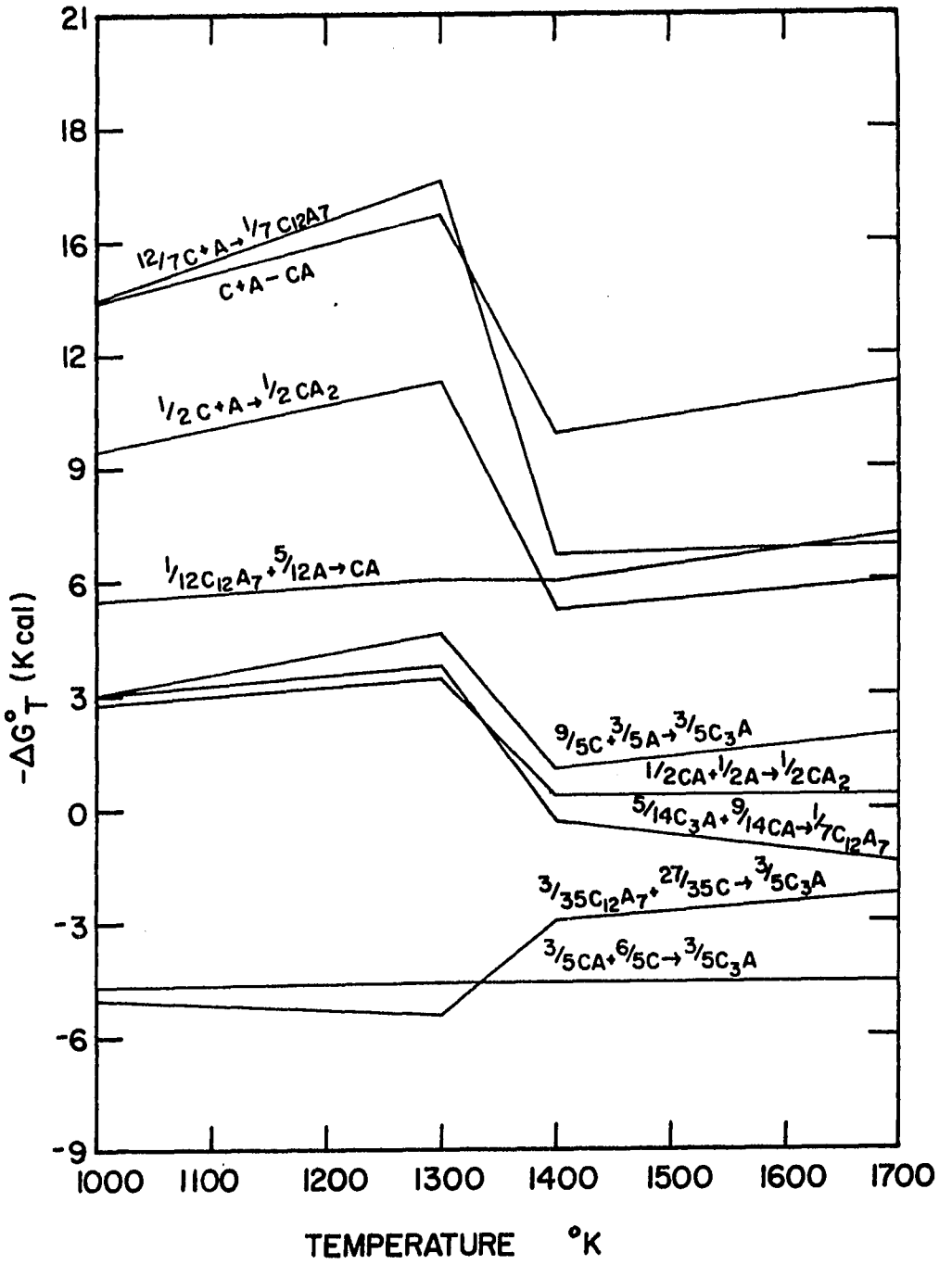

Fig. 57. Calculated free energy changes as a function of temperature for the indicated reactions

our runs. However, we know that the reactions in this system are controlled by diffusion. When the CA or $C_{12}A_7$ phase builds up on the outside of Al_2O_3 particles, the Ca ion has to diffuse through these phases to react with the Al_2O_3. Thus, formation of the Ca rich phase, C_3A, as an intermediate product upon CA or $C_{12}A_7$ is quite conceivable. When the calcium oxide is consumed, this phase will readily convert to $C_{12}A_7$ or CA as observed in the kinetic studies.

Finally, a comment has to be made concerning the reliability of these thermodynamic calculations. It is found that different sets of thermodynamic values will give results of different magnitude, sometimes even different signs (6, 63). Thus, the choice of values for ΔH^o_{298}, ΔG^o_{298} and Cp(T) is very critical to the outcome of the calculations. As a result, we should only use them as a reference in our consideration of the reactions occurring during the sintering stage.

Results of Leaching Studies

The extraction ratios (recoveries) of alumina from the sinters by extraction with a 3% Na_2CO_3 solution are shown in Fig. 58. The extraction ratios increase with both sintering time and sintering temperature. However, the curves seem to flatten out, reaching about 90%, as both parameters increase.

The extraction ratios of pure aluminates, CA, C_3A and $C_{12}A_7$, were also determined under the same leaching conditions. It was found that the extraction ratios of alumina from these compounds were 91.0%

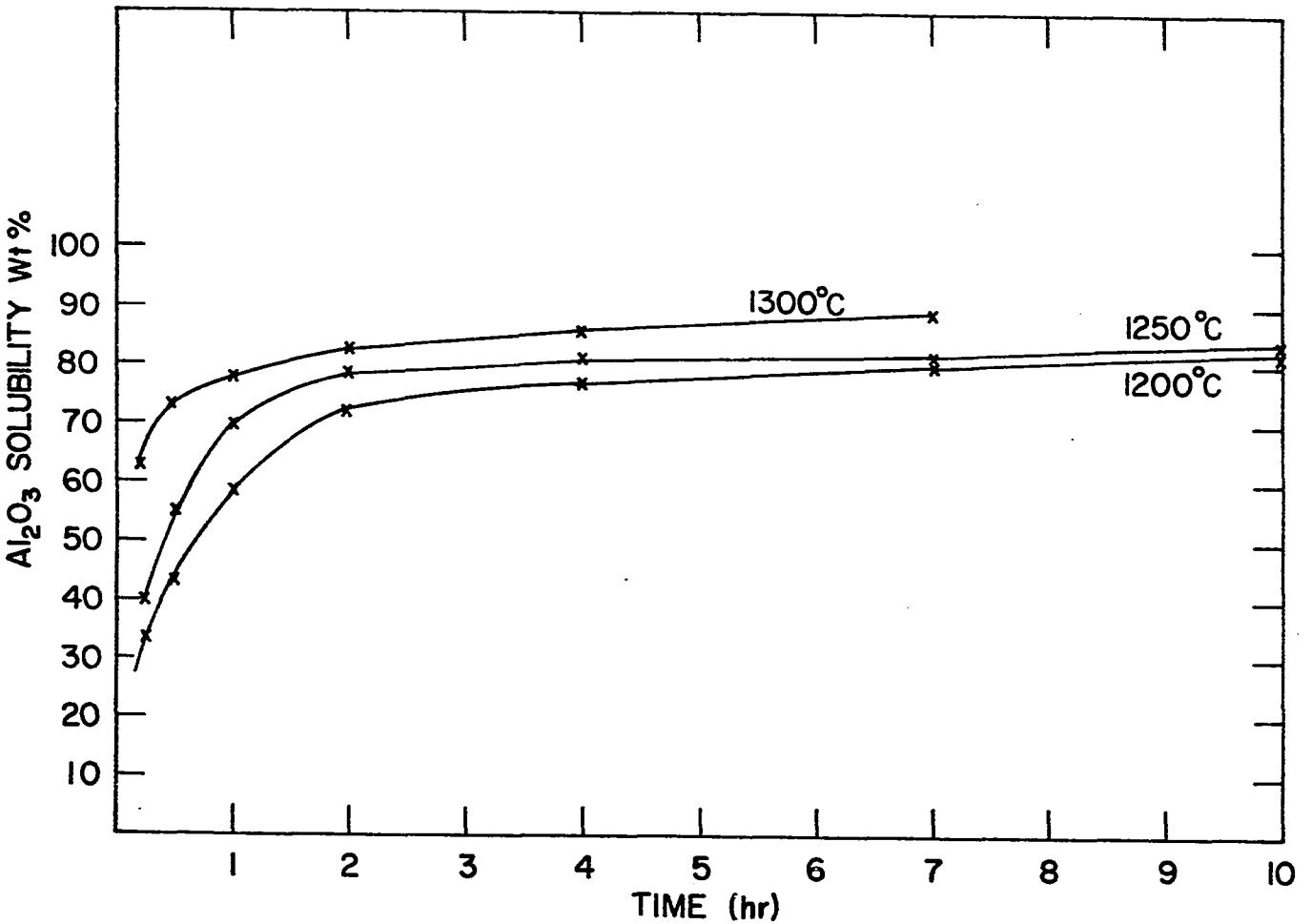

Fig. 58. Extraction ratios (recoveries) of Al_2O_3 for different sintering runs. Extraction was done at 65°C for 15 min with a 3% Na_2CO_3 solution

for CA, 89.1% for $C_{12}A_7$ and 55.5% for C_3A. When the starting γ-Al_2O_3 transformed into α-Al_2O_3, only about 2.5% would dissolve in the solution. Based on these data and the kinetic measurements, the real extraction ratios were compared with the theoretical values. The results showed a good fit between them. Since the equilibrium products in this system are CA and $C_{12}A_7$, it is evident that the maximum extraction rate should be around 90% as indicated from both theoretical calculations and experimental measurements.

The silica contents in the filtrates were also determined and are expressed as weight ratios to the alumina in Fig. 59. The ratios were relatively high for the 0.2 hr runs at each sintering temperature. They then decreased sharply for the 0.5 hr and 1 hr runs and increased again as sintering times were increased. However, the ratios seemed to become relatively constant with further increase in sintering time.

To better understand the reactions occurring during the leaching stage, qualitative X-ray diffraction work was carried out on the residues from the leaching runs. This work was first done on the residues from the leaching of pure aluminates. In all three cases, CA, $C_{12}A_7$ and C_3A, calcite ($CaCO_3$) was precipitated out in the residue. In addition, β-$Al(OH)_3$ was found in the residue of CA; another form of calcite, aragonite and a small amount of unreacted $C_{12}A_7$ were found in the residue of $C_{12}A_7$; and unreacted C_3A and its hydrate C_3AH_6 were observed in the C_3A residue. The leaching reactions for these three aluminates can then be expressed by the following equations (56, 57):

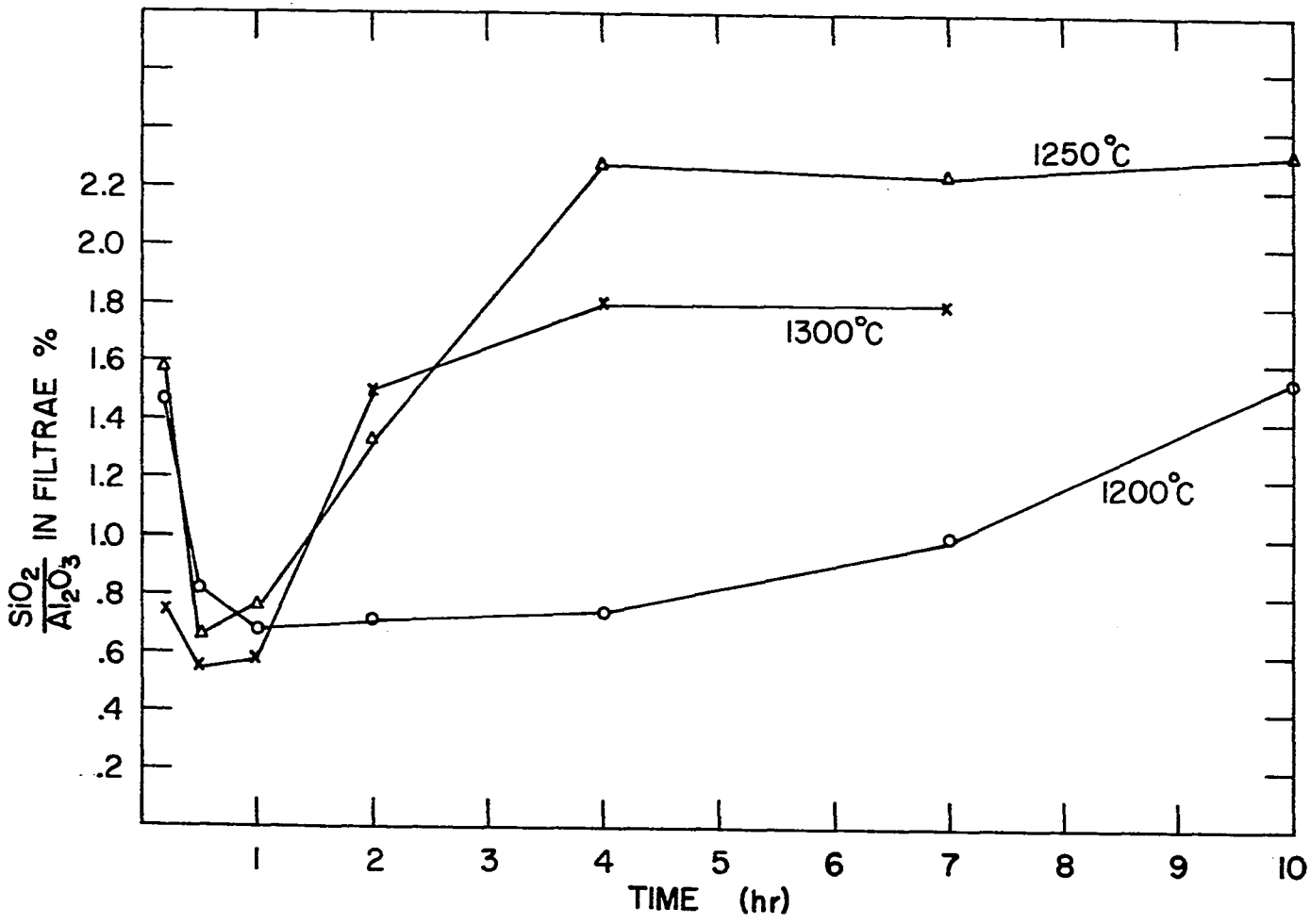

Fig. 59. The SiO_2 contents in the filtrates as a function of sintering temperature and time

$$CaO \cdot Al_2O_3 + Na_2CO_3 \rightleftharpoons CaCO_3\downarrow + 2NaAlO_2 \quad (58)$$

$$12CaO \cdot 7Al_2O_3 + 12Na_2CO_3 + 5H_2O \rightleftharpoons 12CaCO_3\downarrow + 14NaAlO_2 + 10NaOH \quad (59)$$

$$3CaO \cdot Al_2O_3 + 3Na_2CO_3 + 2H_2O \rightleftharpoons 3CaCO_3\downarrow + 2NaAlO_2 + 4NaOH \quad (60)$$

The relatively low solubility of C_3A could be a result of the formation of $3CaO \cdot Al_2O_3 \cdot 6H_2O (C_3AH_6)$ on the surface of the C_3A particles. It would effectively shield the unreacted C_3A from the solution. Lundquist and Leitch (56) found that regrinding of the residues and subjecting them to a subsequent second leaching could improve the alumina extraction.

When pure C_2S was subjected to the same leaching condition, it was found that about 7% (wt) of the SiO_2 in the sample went into solution. X-ray diffraction analysis of the residues showed the formation of $CaCO_3$. It is thus likely that the following reaction occurs to some extent under the present leaching conditions.

$$2CaO \cdot SiO_2 + 2Na_2CO_3 + H_2O \rightleftharpoons 2CaCO_3\downarrow + Na_2O \cdot SiO_2 + 2NaOH \quad (61)$$

When the real sintered samples are leached, there will likely be other side reactions between C_2S and the aluminates in solution (5, 50), all of which will tend to reduce the alumina concentration in the filtrate while increasing that of SiO_2. According to Lecis and Guidi (50), the following two reactions tend to take place:

$$3(2CaO \cdot SiO_2) + 6NaAlO_2 + 15H_2O \rightleftharpoons 3Na_2SiO_3 + 2(3CaO \cdot Al_2O_3 \cdot 6H_2O)\downarrow + 2Al(OH)_3 \quad (62)$$

$$2Na_2SiO_3 + 2NaAlO_2 + 4H_2O \rightleftharpoons Na_2O\cdot Al_2O_3\cdot 2SiO_2\cdot 2H_2O + 4NaOH \quad (63)$$

Arlyuk (5), however, asserted from a thermodynamic viewpoint that the most probable precipitates are $C_6AS_3H_{32}$ and C_4ASH_{12} according to the following two reactions:

$$3(2CaO\cdot SiO_2) + 2NaAlO_2 + 33H_2O \rightleftharpoons 6CaO\cdot Al_2O_3\cdot 3SiO_2\cdot 32H_2O\downarrow + 2NaOH \quad (64)$$

$$2(2CaO\cdot SiO_2) + 2NaAlO_2 + 12H_2O \rightleftharpoons 4CaO\cdot Al_2O_3\cdot SiO_2\cdot 12H_2O\downarrow + Na_2O\cdot SiO_2 \quad (65)$$

When the X-ray diffraction analysis was applied to our samples, the identification of possible precipitates became a real problem because of the tiny quantities involved. From the experimental extraction ratio and the calculated value, we know that there is not much alumina lost through side reactions. The X-ray patterns show that most of the peaks belong to either α- or γ-C_2S. When the maleic acid treatment removes these C_2S peaks, those that are left belong mostly to $CaCO_3$ and unreacted C_3A. The only possible precipitate is C_3AH_6. So, it seems that the reactions proposed by Lecis and Guidi (50) are the most likely to take place in our experiments, though they will not proceed to any significant extent and produce appreciable amounts of sodium aluminum silicate hydrate as indicated by Eq. (63).

CONCLUSIONS

The exploratory work presented in this dissertation combined with the derived results enable the following conclusions to be reached:

1. When a ternary mixture of CaO, Al_2O_3 and SiO_2 is heated to any temperature below the eutectic temperature predicted from the equilibrium phase diagram, it will simply behave like two binary systems, CaO-Al_2O_3 and CaO-SiO_2. For the temperature range 1200°C-1350°C studied, only binary compounds formed.
2. The reactions between CaO and SiO_2 start at a lower temperature and proceed faster than those between CaO and Al_2O_3. As a result, some calcium oxide will enter the structure of dicalcium silicate.
3. The reactions between CaO and Al_2O_3 are carried out through the diffusion of Ca ion, accompanied by the diffusion of either oxygen ion or electrons with oxygen transported through the gas phase. Because of the nature of this process, layer-like products are formed. The C_3A, $C_{12}A_7$ or C_5A_3, CA and CA_2 are all observed at one time or another during the sintering runs.
4. The first aluminate to be formed between CaO and Al_2O_3 is probably $C_{12}A_7$, which quickly reacts with Al_2O_3 to form CA as sintering temperature and time increase. When Ca ion diffuses through the CA layer to react with Al_2O_3, it forms the C_3A phase. As time progresses, at 1200°C, the C_5A_3 phase will be formed from the reactions between CA and

C_3A. However, at higher temperatures, the C_5A_3 phase is unstable and $C_{12}A_7$ will be formed instead.

5. The apparent activation energies for the formation of C_3A and CA have been determined to be 45.6 Kcal/mole and 89.8 Kcal/mole, respectively. These values are probably related to the diffusion processes in their respective phases.

6. The results of Na_2CO_3 leaching of the pure compounds and sinters show that the total extractable alumina is the sum of the extractable alumina from each aluminate phase. Under the leaching conditions employed in this research, the solubility of CA in 3% Na_2CO_3 solution is 91%, while that for $C_{12}A_7$ is 89.1% and that for C_3A is 55.5%. The silica can enter the filtrate through reactions between C_2S and Na_2CO_3 or sodium aluminate.

RECOMMENDATIONS

From the results of this exploratory work the following recommendations are offered for future research:

1. Other variables in this study should be investigated such as the amount of $CaCO_3$ added, the pressure used to make the sintering pellets, the starting state of alumina and silica, etc.
2. In order to make this system more similar to fly ash, the effects of Fe_2O_3 have to be taken into account. Calcium alumina ferrite will inevitably form during the sintering stage. The rate of formation and its subsequent effect on the leaching of alumina should be determined.
3. The lime-soda sinter process offers another attractive alternative to extract alumina from fly ash. Thus the addition of Na_2CO_3 to our system and its effect should be studied. The formation of sodium aluminate and dicalcium silicate in this system can be investigated and later related to the extraction ratio of alumina.
4. The effects of the addition of a small amount of mineralizers need to be determined. These materials should help with the reaction rates between CaO and Al_2O_3, promoting the formation of CA and $C_{12}A_7$ while prohibiting that of the C_3A phase.
5. The effect of atmospheres on the reactions between CaO and Al_2O_3, especially that of the water vapor, should be investigated.

6. Finally, this technique can be applied to other processes for extracting alumina from fly ashes, such as the chlorination (Ames HiChlor) process, to understand the true mechanisms of the reactions taking place.

REFERENCES

1. Ampian, S. G. Lime-soda sinter process. Correlation of reaction products with extractability of alumina from anorthite. U.S. Bureau of Mines, RI6933: 1-44. 1967.

2. Ampian, S. G. X-ray diffraction and optical microscopic data on several important phases in the binary systems $CaO-Al_2O_3$, $CaO-SiO_2$ and $Na_2O-Al_2O_3$. U.S. Bureau of Mines, RI6428: 1-53. 1964.

3. Annual Report of National Ash Association. National Ash Association, Washington, D.C. 30 April 1977.

4. Archibald, F. R., and Nicholson, C. M. Alumina from clay by the lime sinter method II. Transactions of AIMME 182: 14-38. 1949.

5. Arlyuk, B. I. Thermodynamic analysis of reactions between components of alumina sinters and solutions. Journal of Applied Chemistry of USSR 40(4): 729-733. 1967.

6. Babushkin, V. I., and Mehedlov-Petrosyan, O. P. Thermodynamic study of solid-phase reaction in the system of calcium oxide-alumina. Journal of Applied Chemistry of the USSR 32(1): 45-49. 1959.

7. Barclay, J. A., and Peters, F. A. New sources of alumina. Mining Congress Journal 62(6): 29-32. 1976.

8. Birchenall, C. E. The mechanisms of diffusion in solids. Proceedings of the Fourth International Symposium on Reactivity of Solids: 24-37. Edited by J. H. DeBoer. Elsevier Publishing Company, Amsterdam, The Netherlands. 1961.

9. Blanco, M. N., Thomas, H. J., and Pereira, E. Study of the alkaline oxides influence on dicalcium silicate polymorphism II: The thermal treatment in the stabilization of beta-Ca_2SiO_4 polymorph. Latin American Journal of Chemical Engineering and Applied Chemistry 6(1): 45-53. 1976.

10. Bonnickson, K. R. High temperature heat contents of aluminates of calcium and magnesium. Journal of American Chemical Society 59(3): 220-221. 1955.

11. Budnikov, P. P., and Ginstling, A. M. Principles of solid state chemistry: Reactions in solids. MaClaren and Sons Ltd., London, England. 1968.

12. Campbell, W. J. High-temperature diffractometer techniques. Chapter 13 in the "Handbook of X-rays." Edited by E. F. Kaelble. McGraw-Hill Book Company, New York, N.Y. 1967.

13. Capp, J. R., and Spencer, J. D. Fly ash utilization. A summary of applications and technology. U.S. Bureau of Mines, IC8483: 2-65. 1970.

14. Carter, R. E. Kinetic model for solid state reactions. The Journal of Chemical Physics 34(6): 2010-2015. 1961.

15. Chemekova, T. Yu, and Udalov, Yu P. Conditions for synthesis of $5CaO \cdot 3Al_2O_3$ and $12CaO \cdot 7Al_2O_3$. Izvestiya Akademii Nauk SSSR-Neorganicheskie Materialy 10(12): 2191-2193. 1974.

16. Chou, K. S., Klemm, W. A., Murtha, M. J., and Burnet, G. The lime sinter process for production of alumina from fly ash. Proceedings of the Fourth International Symposium on Ash Utilization: 433-449. ERDA, Morgantown Energy Research Center, Morgantown, W. Va. 1976.

17. Chung, F. H. Quantitative interpretation of x-ray diffraction patterns of mixtures. I. Matrix-flushing method for quantitative multicomponent analysis. Journal of Applied Crystallography 7(6): 519-525. 1974.

18. Coughlin, J. P. Heats of formation of crystalline CA, $C_{12}A_7$ and C_3A. Journal of American Chemical Society 78(5): 5479-5482. 1956.

19. Cullity, B. D. Elements of x-ray diffraction. Addison-Wesley Publishing Co., Reading, Massachusetts. 1978.

20. Dean, R. S. Production of alumina from low-grade domestic materials. Mining and Metallurgy: 356-359. August 1943.

21. DeKeyser, W. Lattice defects and reactivity of solids. Proceedings of the Fourth International Symposium on Reactivity of Solids: 376-391. Edited by J. H. DeBoer. Elsevier Publishing Company, Amsterdam, The Netherlands. 1961.

22. Edwards, J. D., Fray, F. C., and Jefferies, Z. Aluminum and its production. Vol. I. McGraw-Hill Book Co., Inc., New York, N.Y. 1930.

23. Eitel, W. The physical chemistry of silicates. The University of Chicago Press, Chicago, Illinois. 1954.

24. Eremin, N. I., Egereva, A. I., Dimitrieva, A. M., and Furfarova, I. B. Investigation of solid solutions of $2CaO \cdot 2SiO_2$ with oxides

of certain metals. Journal of Applied Chemistry of the USSR 43(1): 15-20. 1970.

25. Fierens, P., and Picquet, P. Kinetic studies of the thermal synthesis of calcium silicates above 1400°C: I. Dynamic thermal synthesis of Ca_2SiO_4. Journal of the American Ceramic Society 58(1-2): 50-51. 1975.

26. Fierens, P., and Picquet, P. Kinetic study of the thermal synthesis of calcium silicate above 1400°C: I. Quantitative kinetics of the formation of Ca_2SiO_4 in the presence of a liquid phase. Journal of the American Ceramic Society 58(1-2): 52-54. 1975.

27. Fine, M. E. Introduction to chemical and structural defects in crystalline solids. Chapter 5 in "Treatise on Solid State Chemistry, Vol. 1: The Chemical Structure of Solids." Edited by N. B. Hannay. Plenum Press, New York, N.Y. 1973.

28. Gallagher, K. J. The effect of particle size distribution on the kinetics of diffusion reactions in powders. Proceedings of the Fifth International Symposium on Reactivity of Solids: 192-203. Edited by G. M. Schwab. Elsevier Publishing Company, Amsterdam, The Netherlands. 1965.

29. Garn, P. D. Thermoanalytical methods of investigation. Academic Press, New York, N.Y. 1965.

30. Ginstling, A. M., and Brounshtein, B. I. Concerning the diffusion kinetics of reactions in spherical particles. Journal of Applied Chemistry of USSR 23(12): 1249-1259. 1950.

31. Gomes, W. P., and DeKeyser, W. Factors influencing the reactivity of solids. Chapter 2 in "Treatise on Solid State Chemistry, Vol. 4: Reactivity of Solids." Edited by N. B. Hannay. Plenum Press, New York, N.Y. 1976.

32. Gordeev, S. Ya, and Sychev, M. M. Kinetics of the reaction between solid substance in powder mixture. Journal of Applied Chemistry of the USSR 50(6) Part I: 1252-1256. 1977.

33. Grim, R. E., Machin, J. S., and Bradley, W. F. Amenability of various types of clay mineral to alumina extraction by the lime sinter and lime soda sinter processes. Illinois State Geological Survey, Bulletin No. 69: 9-75. 1945.

34. Harrison, L. G. The theory of solid state kinetics. Chapter 5 in "Comprehensive Chemical Kinetics, Vol. 2." Edited by C. H. Bamford and C. F. H. Tipper. Elsevier Publishing Company, Amsterdam, The Netherlands. 1969.

35. Hose, H. R. Bauxite mineralogy. AIMME International Symposium on the Extractive Metallurgy of Aluminum Proceedings: Alumina 1: 3-20. 1962.

36. Hulbert, S. F., Brosnan, D. A., and Smoak, R. H. Kinetics and mechanism of the reaction between MgO and Cr_2O_3. Proceedings of the Sixth International Symposium on Reactivity of Solids: 573-582. Edited by J. W. Mitchell, R. C. DeVries, R. W. Roberts, and P. Cannon. John Wiley and Sons, New York, N.Y. 1969.

37. Hulbert, S. F., and Kalawitter, J. J. Kinetics and mechanism of the reaction between zinc oxide and barium carbonate. Journal of the American Ceramic Society 50(9): 484-488. 1967.

38. Hulbert, S. F., and Popowich, M. J. Kinetics and mechanism of the reaction between TiO_2 and $SrCO_3$. Pages 422-445 in "Materials Science Research, Vol. 4: Kinetics of Reactions in Ionic System." Edited by T. J. Gray and V. D. Frechette. Plenum Press, New York, N.Y. 1969.

39. Imlach, J. A., Dent Glasser, L. S., and Glasser, F. P. Excess oxygen and the stability of $12CaO \cdot 7Al_2O_3$. Cement and Concrete Research 1: 57-61. 1971.

40. Ito, S., Kato, M., Suzuki, K., and Inagaki, M. Layer formation and apparent activation energies of formation of calcium aluminates. Zeitschrift für Physikalische Chemie Neue Folge 104(1-3): 147-154. 1977.

41. Ito, S., Shibata, S., Suzuki, K., and Inagaki, M. Kinetic study on the formation of calcium monoaluminate. Yogyo Kyokai Zasski 83(5): 239-243. 1975.

42. Kelley, K. K., and E. G. King. Contributions to the data on theoretical metallurgy. XIV. Entropies of the elements and inorganic compounds. U.S. Bureau of Mines, Bulletin 592. 1961.

43. Kingery, W. D. Introduction to ceramics. John Wiley and Sons, New York, N.Y. 1960.

44. Klug, H. P., and Alexander, L. E. X-ray diffraction procedures for polycrystalline and amorphous materials. 2nd edition. John Wiley and Sons, New York, N.Y. 1973.

45. Kohatsu, I., and Brindley, G. W. Solid state reactions between CaO and alpha-Al_2O_3. Zeitschrift für Physikalische Chemie Neue Folge 60(1-4): 79-89. 1968.

46. Komatsu, W. The effect of particle size and mixing ratio on the reaction rate in a mixed powder system. Proceedings of the Fifth International Symposium on Reactivity of Solids: 182-191. Edited

by G. M. Schwab. Elsevier Publishing Company, Amsterdam, The Netherlands. 1965.

47. Komatsu, W., and Uemura, T. Kinetic equations of solid state reactions for counterdiffusion systems. Zeitschrift für Physikalische Cheme Neue Folge 72(1-3): 59-75. 1970.

48. Kröger, F. A. Point defects in compounds and their role in diffusion. Pages 29-54 in "Sintering and Related Phenomena." Edited by G. C. Kuczynski, N. A. Hooton and C. F. Gibbon. Gordon and Breach Science Publishers, Inc., New York, N.Y. 1967.

49. Lea, F. M. The chemistry of cement and concrete. Edward Arnold and Company, London, England. 1970.

50. Lecis, P., and Guidi, P. A. Pyrogenic attack of bauxite. AIMME International Symposium on the Extractive Metallurgy of Aluminum Proceedings: Alumina 1: 231-249. 1962.

51. Lepkowski, W. Politics and the world's raw materials. Chemical and Engineering News 57(23): 14-19. 1979.

52. Levin, E. M., and McMurdie, H. F. Phase diagrams for ceramists. 1975 Supplement. American Ceramic Society, Columbus, Ohio. 1975.

53. Levin, E. M., Robbins, C. R., and McMurdie, H. F. Phase diagrams for ceramists. American Ceramic Society, Columbus, Ohio. 1964.

54. Lopez, J. M. P., Thomas, H. J., and Pereira, E. Kinetic study of the chemical step in the tricalcium silicate formation reaction. Latin American Journal of Chemical Engineering and Applied Chemistry 6(1): 33-43. 1976.

55. Luginina, I. G. The kinetics of dicalcium silicate formation. Journal of Applied Chemistry of the USSR 29(12): 1873-1874. 1956.

56. Lundquist, R. V., and Leitch, H. Aluminum extraction characteristics of three calcium aluminates in water, sodium hydroxide and sodium carbonate solutions. U.S. Bureau of Mines, RI6528: 1-16. 1964.

57. Lundquist, R. V., and Leitch, H. Solubility characteristics of monocalcium aluminate. U.S. Bureau of Mines, RI6294: 1-9. 1963.

58. Macias, J. Calcium aluminates in the production of alumina and cement by a thermal decomposition method. Cement-Wapno-Gips 9: 273-277. 1968.

59. MacKenzie, K. J. D., and Banerjee, R. K. Formation kinetics of Portland cement clinker phases. I. Tricalcium aluminate. Transactions and Journal of the British Ceramic Society 77(3): 88-92. 1978.

60. MacKenzie, K. J. D., and Hadipour, N. Formation kinetics of Portland cement clinker phases. III. Beta-dicalcium silicate and tricalcium silicate. Transactions and Journal of the British Ceramic Society 77(6): 168-171. 1978.

61. Manning, J. R. Diffusion kinetics for atoms in crystals. D. Van Nostrand Company, Inc., New York, N.Y. 1968.

62. Marinov, M. R., Panova, S. I., and Dimitriev, Y. B. Investigating the kinetics of mullite formation in mixtures of alumina and silica and in mixtures of kaolin and alumina. Doklady Bolgarskoi Akademii Nauk 27(5): 647-650. 1974.

63. Mchedlov-Petrosyan, O. P. Thermodynamik der Silikate. Veb Verlag für Bauwesen, Berlin, W. Germany. 1966.

64. Midgley, H. G. Quantitative determination of phases in high alumina cement clinkers by x-ray diffraction. Cement and Concrete Research 6(2): 217-224. 1976.

65. Minnick, L. J. Fundamental characteristics of pulverized coal fly ashes. ASTM Proceedings 59: 1155-1177. 1959.

66. Montierth, M. R., Gordon, R. S., and Culter, I. B. The initial stages of reaction between quartz and calcium carbonate. Pages 522-544 in "Material Science Research, Vol. 4. Kinetics of Reactions in Ionic Systems." Plenum Press, New York, N.Y. 1969.

67. Newbury, D. E., and Yakowitz, H. Specimen preparation, special techniques and applications of the scanning electron microscope. Chapter VI in "Practical Scanning Electron Microscopy." Edited by J. I. Goldstein and H. Yakowitz. Plenum Press, New York, N.Y. 1975.

68. Nowak, hab. inz. Zygfrad. Iron and alumina extraction from power plant fly ash in Poland. U.S. Bureau of Mines, IC8640: 224-230. 1974.

69. Nurse, R. W. The dicalcium silicate phase. Proceedings of the Third International Symposium on the Chemistry of Cement: 56-90. Cement and Concrete Association, London, England. 1952.

70. Nurse, R. W., Welch, J. H., and Majumdar, A. J. The $12CaO \cdot 7Al_2O_3$ phase in $CaO-Al_2O_3$ system. Transactions of British Ceramic Society 64(6): 323-332. 1965.

71. Peacey, J. G., and Davenport, W. G. Evaluation of alternative methods of aluminum production. Journal of Metals 26(7): 25-28. 1974.

72. Peters, F. A., Kirby, R. C., and Higbie, K. B. Methods for producing alumina from clay — An evaluation. Journal of Metals 19(10): 26-34. 1967.

73. Pope, M. I., and Judd, M. D. Differential thermal analysis. Heyden and Son, Ltd., London, England. 1977.

74. Pribil, R., and Vesley, V. Contributions to the basic problems of complexometry. IX. The determination and masking of alumina. Talanta 9: 23-26. 1962.

75. P'yachev, V. A., Chebukov, M. F., and Cherepanova, P. V. N. Formation kinetics of dicalcium silicate. Izvestiya Akademii Nauk SSSR, Neorganicheskie Materialy 10(7): 1303-1306. 1974.

76. Ramachandran, V. S. Applications of differential thermal analysis in cement chemistry. Chemical Publishing Company, Inc., New York, N.Y. 1969.

77. Rastogi, R. P. Solid-solid reactions: Classification, mechanism of interaction, diffusion and reaction kinetics. Journal of Scientific and Industrial Research 29(4): 177-189. 1970.

78. Ress, A. L. G. Elementary processes in solid state reactions. Proceedings of the First Australian Conference on Electrochemistry: 3-26. 1963.

79. Rhodin, T. N. Recent approaches to the interpretation of atom-surface interactions. Proceedings of the Seventh International Symposium on Reactivity of Solids: 651-680. Edited by J. S. Anderson, M. W. Roberts and F. S. Stone. Chapman and Hall Ltd., London, England. 1972.

80. Sasaki, H. Introduction of particle size distribution into kinetics of solid state reaction. Journal of American Ceramic Society 47(10): 512-516. 1964.

81. Schmalzried, H. Solid-solid reactions. Proceedings of the 25th International Meeting of the Societe de Chemie Physique: 558-577. Edited by P. Barret. Elsevier Scientific Publishing Company, Amsterdam, The Netherlands. 1975.

82. Schmalzried, H. Solid state reactions. Chapter 5 in "Treatise on Solid State Chemistry, Vol. 4." Edited by N. B. Hannay. Plenum Press, New York, N.Y. 1976.

83. Scott, T. R. The recovery of alumina from its ores by a sulfuric acid process. AIME International Symposium on the Extractive Metallurgy of Aluminum Proceedings, Alumina 1: 305-332. 1962.

84. Seimiya, S. Some properties of sodalite in red mud. AIMME International Symposium on the Extractive Metallurgy of Aluminum Proceedings, Alumina 1: 115-132. 1962.

85. Sharp, J. H., Brindley, G. W., and Achar, B. N. N. Numerical data for some commonly used solid state reaction equations. Journal of the American Ceramic Society 49(7): 379-382. 1966.

86. Standard method for chemical analysis of hydraulic cement. Pages 79-117 in 1977 Annual Book of ASTM Standards. ASTM, Philadelphia, Pennsylvania. 1977.

87. Standard methods of analysis of coal and coke ash. Pages 540-547 in 1977 Annual Book of ASTM Standards. ASTM, Philadelphia, Pennsylvania. 1977.

88. Stone, F. S. The kinetics and mechanism of reactions of solid. Proceedings of the Fourth International Symposium on the Reactivity of Solids: 7-23. Edited by J. H. DeBoer. Elsevier Publishing Company, Amsterdam, The Netherlands. 1965.

89. Stull, D. R., and Prophet, H. JANAF thermochemical tables, 2nd ed. U.S. Department of Commerce, National Bureau of Standards, Washington, D.C. 1971.

90. Tabikh, A. A., and Weht, R. J. An x-ray diffraction analysis of Portland cement. Cement and Concrete Research 1(3): 317-328. 1971.

91. Thomas, J. M., and Williams, J. O. Dislocations and the reactivity of organic solids. Progress in Solid State Chemistry 6: 119-154. Edited by H. Reiss and J. O. McCaldin. Pergamon Press, Oxford. 1971.

92. Tompkins, F. C. Influence of structure on solid state reaction. Proceedings of the Fifth International Symposium on the Reactivity of Solids: 3-8. Edited by G. M. Schwab. Elsevier Publishing Company, Amsterdam, The Netherlands. 1965.

93. Toporov, N. A., Barzakovskii, V. P., Lapin, V. V., and Kurtseva, N. N. Handbook of phase diagrams of silicate systems, Vol. 1: Binary systems. U.S. Department of Commerce, NBS and NSF, Washington, D.C. 1972.

94. Watt, J. D., and Thorne, D. J. Characteristics of fly ashes II. Journal of Applied Chemistry 15: 595-604. 1965.

95. Wells, O. C. Scanning electron microscopy. McGraw-Hill Book Company, New York, N.Y. 1974.

96. Wendlandt, W. W. Thermal methods of analysis. 2nd ed. John Wiley and Sons, New York, N.Y. 1974.

97. Williamson, J., and Glasser, F. P. Reactions in heated lime-alumina mixtures. Journal of Applied Chemistry 12(12): 535-538. 1962.

98. Yakowitz, H. Methods of quantitative x-ray analysis used in electron probe microanalysis and scanning electron microscopy. Chapter IX in "Practical Scanning Electron Microscopy." Edited by J. I. Goldstein and H. Yakowitz. Plenum Press, New York, N.Y. 1975.

99. Zerfoss, S., and Davis, H. M. Observations on solid-phase inversions of calcium orthosilicates, constituent of dolomite-silica brick. Journal of the American Ceramic Society 26(9): 302-307. 1943.

100. Zwell, L., and Danko, A. W. Applications of x-ray diffraction methods to quantitative chemical analysis. Applied Spectroscopy Reviews 9(2): 167-221. 1975.

ACKNOWLEDGMENTS

The author wishes to express his gratitude to Dr. George Burnet for his advice and helpful criticism during this research and the writing of this dissertation and to Ames Laboratory of the Department of Energy for the support throughout this investigation. A special thanks is due to the author's wife for her encouragement and patience.